TRANSPORT IN RIGID AND DEFORMABLE HYGROSCOPIC POROUS MEDIA DURING ELECTROMAGNETIC AND COMBINATION HEATING

A Dissertation

Presented to the Faculty of the Graduate School

of Cornell University

in Partial Fulfillment of the Requirements for the Degree of

Doctor of Philosophy

by

Vineet Rakesh

February 2010

TRANSPORT IN RIGID AND DEFORMABLE HYGROSCOPIC POROUS MEDIA DURING ELECTROMAGNETIC AND COMBINATION HEATING

Vineet Rakesh, Ph.D.

Cornell University 2010

Fundamental physics-based modeling integrated with relevant experimentation provides an effective framework to study a variety of transport processes in porous media. The work includes the development of a multiphase porous media model and magnetic resonance imaging (MRI) experiments to study and optimize two processes: microwave combination heating and microwave puffing. Microwave combination heating involves electromagnetic heating combined with other heating modes. The material heated during the process was modeled as a rigid porous medium with multiple phases and modes of transport. The model included three different phases: solid matrix, water and gas (water vapor and air), and considered pressure driven flow, binary diffusion and phase change. The 3D multiphase porous media model was coupled with electromagnetics and was solved using finite element method. Microwave puffing refers to significant structural changes in the material due to high pressure development caused by phase change during rapid heating. The two-way coupling of multiphase porous media transport and large deformation, which is critical to accurately simulate the microwave puffing process, was implemented. MRI and other experiments were designed to obtain spatial temperature and moisture distributions in the material during the heating process to validate the computational models. The results from computations and MRI experiments were analyzed to provide comprehensive and fundamental understanding and to thereby optimize the processes.

BIOGRAPHICAL SKETCH

Vineet Rakesh was born in the city of Ranchi in India. He went to elementary, middle and high school in this city and moved to Kharagpur for his undergraduate education in July of 1999. In 2003, he completed his Bachelor's degree in Agricultural and Food Engineering from the Indian Institute of Technology, Kharagpur. During his stay at IIT, Vineet pursued a number of courses related to transport phenomena, which got him interested in the field of biological transport with applications to biological systems and food processing. In August of 2003, he joined the Department of Biological and Environmental Engineering at Cornell University, Ithaca, to pursue graduate studies in this field. He obtained his Master of Science degree at Cornell University and continued for a PhD. In addition to the research presented in this dissertation, he also worked on modeling of biomedical processes that include turbulent flow modeling in the upper airway and modeling of antibody based drug delivery systems.

To my sisters, Smita and Namrata

ACKNOWLEDGEMENTS

First of all, I would sincerely like to thank my advisor, Professor Ashim K. Datta, for his persistent support and guidance throughout my stay at Cornell for the last six years. The successful completion of this work as well as other projects would not be possible without the numerous discussions with him, his encouragement and optimism about the projects. I am highly indebted to him for all the time he devoted for the discussions with me that has helped me develop academically as a researcher and will help me in my future career.

I would like to thank Professor Subrata Mukherjee for the numerous discussions related to solid mechanics modeling that helped me understand finer details of the topic and the need for large deformation modeling for the microwave puffing part of the dissertation and for being a part of my Special Committee. I would also like to acknowledge Professor Charles E. Seyler for his role on my Special Committee. I sincerely thank Professors Kathryn L. McCarthy and Michael J. McCarthy at the University of California, Davis for the magnetic resonance imaging measurements and for hosting me at their facility.

A special thanks to my colleagues in the research group, Amit Halder and Ashish Dhall for their technical support that helped me in the most difficult times as well as for their assistance and company. I am also thankful to Haolin Zhu for the invaluable discussions regarding solid mechanics modeling. I would also like to thank Youngseob Seo, graduate student at the University of California, Davis, for the MRI measurements for gel samples. Finally, I would like to thank my family and friends for their love and support throughout the work.

TABLE OF CONTENTS

LIST OF TABLES

LIST OF FIGURES

CHAPTER 1

INTRODUCTION

Heat, mass and momentum transport in porous media is a complicated process and finds application in a number of fields- biomedical applications, groundwater flow, reservoir flow, fuel cells, industrial drying of ceramics, wood and foodstuffs, food processing and pharmaceuticals, to name a few. In most of these materials, the flow comprises of multiple phases and modes of transport. In addition, many of these processes are accompanied with complex heating mechanisms such as microwave or electromagnetic heating. Intensive heating of porous materials containing water leads to phase change throughout the material and structural changes when the associated pressures become large. For intensive heating situations, the deformations may be large and it thereby introduces additional non-linearity in the problem. Hygroscopicity of the material further increases the complexity in such situations. To understand and optimize processes such as those discussed above, it is critical to develop fundamentals based models that can resolve the different physics involved. Grossly simplified description of such problems in absence of precise engineering understanding does not help towards the development and optimization of such processes since the models tend to be ad hoc and cannot readily be applied to different conditions.

This work aims to develop a generic framework for modeling multiphase transport in rigid and deformable porous media that is hygroscopic with proper resolution of the different phases, transport and heating mechanisms, and structural changes occurring in the material. The proposed models within the framework are fundamental physics based so that transport and deformations can be easily related to measurable physical processes. In this chapter, a general introduction to the different physics that were considered to develop the models is included.

1.1 Hygroscopic porous medium and multiple phases

A porous medium may be defined as a portion of space occupied by a heterogenous or multiphase matter with two parts: a solid matrix and the remaining pore space[1]. At least some part of the pore space should be interconnected. The pore space is generally filled with the transportable phases. A hygroscopic solid is a material that can attract moisture from the surroundings and therefore the vapor pressure of the surrounding air is a function of the moisture content and temperature of the solid[2]. Similarly, in a hygroscopic porous medium the vapor pressure of the air in the surrounding is a function of the moisture content and temperature of the medium. For the development of this particular framework for modeling porous media flow, two different phases, liquid and gas, were considered. The liquid phase constitutes of water and the gas phase consists of vapor and air as its two components.

1.2 Modes of transport

Transport of momentum, mass and energy occurs inside the porous medium. Since the velocities of the transportable phases are low, Darcy's law is valid for flow in the porous medium. Liquid water in the pore spaces moves due to capillarity and convective flow. The gas phase moves by convective flow. The components of the gas flow, *i.e.*, vapor and air, undergo binary diffusion as well as move by convection. The liquid and gas phases may exchange mass during phase change or evaporation/ condensation. Since heating processes are considered, heat transfer occurs inside the material. It is assumed that all the phases are at thermal equilibrium and they share the same temperature within a representative elementary volume (REV). Heat transfer occurs by convection of the transportable phases, conduction and the energy involved in phase change. In addition,

the different heating mechanisms heat the materials either volumetrically or at the surface.

1.3 Heating mechanism- Electromagnetic heating

In the context of this study, the primary heating mechanism that is considered is the volumetric electromagnetic heating due to microwaves. Therefore, in addition to formulation of the multiphase porous media model for transport, a model for solution of the electric field distribution has to be developed. The electric field distribution is governed by the Maxwell's law of electromagnetics. Solution of the Maxwell's equation gives the electric field distribution in the space, a cavity in this particular case. From the electric field distribution, the microwave power deposition can be calculated[3]. Consideration of electromagnetic heating introduces additional complexities. A full three dimensional model with the accurate details of the geometry needs to be incorporated to accurately determine the resonance patterns in the cavity and therefore the electric field distribution. Since the resulting heating pattern is non-uniform volumetrically, the multiphase porous media model also needs to be developed in a three-dimensional domain. Additionally, electromagnetics and transport need to be fully coupled. As temperature and moisture distribution in the material changes with heating time, the dielectric properties change which in turn changes the electric field distribution inside the domain. As a result the microwave power absorption changes and electromagnetic simulations have to be repeated to determine the updated microwave source term. This feedback mechanism needs to be included in the model. To date, no study has accounted for such a detailed coupling of these different physics.

1.4 Deformation

Intensive heating, such as due to microwaves, can lead to excessive evaporation in materials containing moisture due to pressure development. In certain cases of microwave heating, the porous material may undergo large deformations. The solid mechanics problem, as a result, becomes very complex as both geometric and material non-linearity have to be considered[4–6]. Most of the solid mechanics modeling work that have included detailed transport formulations have only implemented small deformation version of the problem. However, to model the representative processes accurately the two way coupling effects of transport and large deformation needs to be incorporated. The coupling is implemented by formulating the set of equations in a moving Arbitrary Lagrangian-Eulerian (ALE) grid setting[7]. Again, this problem has not been solved earlier.

1.5 Experimental methodology

To comprehensively understand the different phenomena, it is important to develop sophisticated experimental techniques to gain insight into the processes. Also critical is precise experimental validation of the computational modeling framework considering the complexity of the models. Detailed and accurate measurement of volumetric electromagnetic heating involves 3D mapping of variables such as temperature and moisture using a technique such as Magnetic Resonance Imaging (MRI). MRI for temperature and moisture mapping along with other temperature measurement tools such as surface temperature measurement using infrared thermography camera and point temperature measurement using fiber optic temperature probe were used. Measurements of input parameters for the models such as dielectric and thermal properties were also performed.

1.6 Objectives

The specific objectives of this work are outlined below.

- Formulate and solve a fundamental physics based mathematical model for multi-phase transport in porous media during electromagnetic and combination heating.
- Formulate and solve a model for transport in a deformable porous medium during electromagnetic heating.
- Use magnetic resonance imaging (MRI) and other experiments for fundamental understanding of the processes and to validate the computational models.
- Use the computational models to test *"what-if"* scenarios with the aim of design and optimization of the processes.

1.7 Organization of the dissertation

The dissertation is organized into five chapters. Overview of the different chapters are given below (also shown in Figure 1.1).

Chapter 1: Introduction This chapter provides an introduction to the work and the overall objectives.

Chapter 2: Coupled Electromagnetics- Heat Transfer Model In this chapter, the 3D electromagnetics model is developed. Transport is limited to heat transfer only. To justify this assumption, appropriate test material is chosen and the heating is limited to a short duration. It is also assumed that dielectric and thermal properties are constant

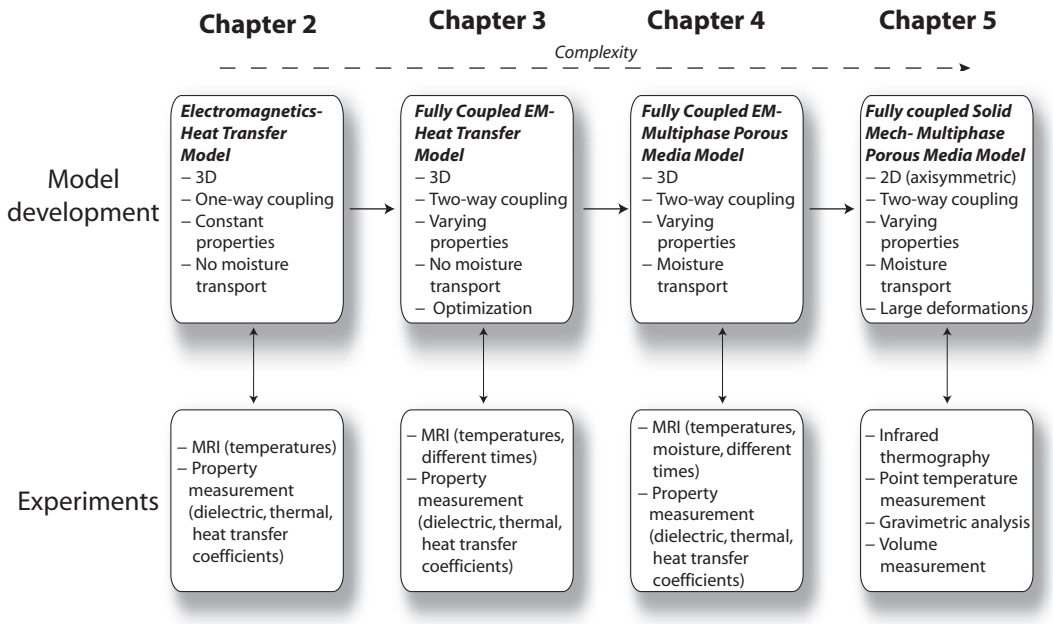

Figure 1.1: Organization of the dissertation.

during the period of heating due to the short duration. Therefore, a one-way coupling is considered and the Maxwell's equations are only solved initially. MRI is used to obtain temperature maps at the final time to verify the model qualitatively.

Chapter 3: Fully coupled Electromagnetics- Heat Transfer Model and Simple Optimization This chapter details the formulation of the fully coupled electromagnetics-heat transfer model. The heating times considered are longer and the dielectric and thermal properties vary with time. Therefore a full two-way coupling between electromagnetics and heat transfer is incorporated. Appropriate material is chosen so that there is minimum moisture loss and the transport is limited to heat transfer. Detailed MRI measurements are included. Spatial profiles of temperature were obtained at different times during the heating process and quantitative comparisons are done with the predicted results from the model for validation. Objective functions are defined and used with the model for design and optimization.

Chapter 4: Fully coupled Electromagnetics- Multiphase Porous Media Model The chapter includes the details about the formulation and implementation of the complete multiphase porous media model fully coupled with the electromagnetics model. This is the most generic model that includes heat, mass and momentum transfer inside the porous medium during the electromagnetic heating process. Validation of the model is done using MRI measurements that include spatial temperature and moisture mapping. Different materials and combinations are analyzed to arrive at generic guidelines for electromagnetic and combination heating processes.

Chapter 5: Fully coupled Solid Mechanics- Multiphase Porous Media Model In this chapter, the fully coupled solid mechanics and multiphase porous media transport model is developed and solved. Large deformations are considered for the solid mechanics model and the ALE formulation is used. Validation is done by comparisons of the model with measured surface temperatures distribution (determined using infrared thermography), point temperature history, moisture loss and volume change. Different processing conditions are analyzed to optimize the process.

BIBLIOGRAPHY

[1] Bear J. Dynamics of Fluids in Porous Media, Dover Publications Inc, New York, NY. 1972.

[2] Datta AK. Biological and Bioenvrionmental Heat and Mass Transfer, Marcel Dekker Inc, New York, NY. 2002.

[3] Cheng DK. Field and Wave Electromagnetics, Second Edition, Addison-Wesley Publishing Company Inc, Reading, MA. 1989.

[4] Coussy O. Poromechanics, John Wiley & Sons Ltd, West Sussex, England. 2004.

[5] Simo JC, Hughes TJR. Computational Inelasticity, Springer-Verlag Inc, New York, NY. 1998.

[6] Belytschko T, Liu WK, Moran B. Nonlinear Finite Elements for Continua and Structures, John Wiley & Sons Ltd, West Sussex, England. 2001.

[7] Donea J, Huerta A, Ponthot JP, Rodríguez-Ferran. Arbitrary Lagrangian-Eulerian Methods. In Encyclopedia of Computational Mechanics Volume 1, Eds. Stein E, Borst RD, Hughes TJR, John Wiley & Sons Ltd, West Sussex, England. 2004.

CHAPTER 2

COUPLED ELECTROMAGNETICS- HEAT TRANSFER MODEL

2.1 Abstract

Physics-based modeling complemented with magnetic resonance imaging (MRI) for validation can provide a novel means to understand and thereby optimize combination heating processes. The objectives of this study were to: compare heating patterns in a combination radiant, forced air and microwave oven measured by MRI with those predicted by coupled electromagnetics-heat transfer model, quantify speed and uniformity of heating for the different combination modes, determine the effect of food dielectric properties on heating patterns and delineate the nature of individual heating modes and their combinations. The modes of radiant heating through heating elements and forced convection by fan lead to more uniform heating compared to the faster (but less uniform) heating method provided by the microwaves. Combination methods were faster than radiant-forced air and microwave only heating. Although the speed of heating increases appreciably for combination modes, the non-uniformity of heating does not increase as much.

Practical Applications The results from the study can be used to develop design recommendations/ guidelines for combination heating for different thermal processes such as baking, broiling, roasting and reheating of different materials grouping them based on their properties. The research can benefit the consumers, food services and equipment manufacturers to understand the combination heating process in a better way and to, thereby, use it efficiently. Without a fundamental understanding of the effect of various

Reprinted with permission from "Rakesh V, Datta AK, Amin MHG, Hall LD. Journal of Food Process Engineering.2009; 32(3): 398-424".

combinations, optimization of heating can be intractable. The fundamental approach used in this study would, therefore, help consumers and food services in preparation of safe and high quality foods through combination heating. The work would also help equipment manufacturers in optimizing the designs of combination heating ovens.

Nomenclature

Symbol	Description and unit
$\mathbf{E}$	electric field intensity, V/m
$\mathbf{H}$	magnetic field intensity, A/m
T	temperature, °C
t	time, s
c_p	specific heat, J/kg K
k	thermal conductivity, W/m K
P	power density, W/m^3
h_c	surface heat transfer coefficient, W/m^2 K
T_a	oven temperature, °C
ϵ_0	permittivity of free space, 8.854×10^{-12} F/m
μ	permeability of free space, $4\pi \times 10^{-7}$ H/m
ϵ	complex relative permittivity, dimensionless
ϵ'	dielectric constant, dimensionless
ϵ''	dielectric loss, dimensionless
ω	angular frequency, rad/s
ρ	density, kg/m^3

2.2 Introduction and Objectives

Combination heating of foods refers to combining various modes of heating such as microwaves, infrared and hot air. These heating modes have their own characteristic heating patterns in space and time. Microwave heating is known to be faster and more convenient compared to conventional heating methods. However, there are numerous problems associated with microwave heating such as development of hot and cold spots, edge over-heating, sogginess and lack of browning[1–3]. As a result, microwaves have mostly been used for reheating of food rather than actual cooking. Microwave assistance to conventional cooking methods like baking and broiling could help in combining the advantages of microwaves with complementary characteristics of other modes of heating. For example, infrared or hot air heating can provide surface heating, which can reduce the problem of surface moisture accumulation during microwave heating. Combination of heating modes can potentially provide desired profiles of temperature needed for specific food processes. Physics-based computer modeling complemented with experimentation using magnetic resonance imaging (MRI) for validation can provide a novel means to understand and thereby optimize such combination heating processes.

2.2.1 Past work on combination heating

Most of the work on combination heating has been done in the context of combination microwave-convection drying[4–8] where spatial heating uniformity was not deemed to be the key parameter and therefore was not reported. Other combination heating systems like jet impingement with microwave have also been considered by researchers [9,10]. Others have also looked at jet impingement systems in detail[11,12] but have not considered the combination of jet impingement and microwave heating. Baking has been

studied experimentally for microwave-jet impingement[13] and microwave-infrared ovens [14] in relation to final product quality (such as specific volume, crust color, texture, etc) and reduction in cooking time compared to conventional ovens. Changes in physical properties during baking were measured for microwave-infrared and microwave-jet impingement heating recently[15]. Most of these studies have treated the food as lumped, ie., spatial information is not available. Also, the studies did not attempt to separate contributions due to each mode of heating and provide insight into the nature of combining the modes. A physics-based computational model that captures the spatial and temporal heating patterns combined with complementary experimentations using MRI can provide valuable insight into the nature of combination heating. However, no such study has been accomplished in the literature.

2.2.2 Mathematical Modeling of Microwave Heating

Mathematical modeling of microwave-only heating started with analytical models[16,17]. Researchers have also studied microwave heating computationally using a simplified form for the microwave heat generation term obtained by assuming exponential decay (Lambert's Law) of microwave intensity and thereby solving the heat and mass transfer equations only[18–20]. However, these methods do not accurately represent food heating situations in a multimode resonant oven cavity where the electric field varies in the three directions. For solving the set of Maxwell's equations that govern the electromagnetic field distribution inside the microwave oven cavity, finite difference time domain (FDTD) method[21,22] and finite element method (FEM)[23] are therefore used with the availability of extensive computing facilities. The majority of the work has, however, been on microwave-only heating. Combinations of microwave heating with other modes have also been studied using mathematical models although they are not nearly as fre-

quent. Jumah and Raghavan (2001)[5] studied heat and moisture transfer during combination microwave-convection drying. Datta and Ni (2002)[18] modeled combination microwave-infrared and microwave-hot air treating food as a multiphase porous medium and including the pressure driven flow. However, in both cases the Maxwell's equations were not solved and microwave heating was modeled by the Lambert's law assumption. Wappling-Raaholt *et al.* (2002)[3] solved Maxwell's equations using the FDTD method and coupled it with heat transfer to study microwave and forced air combination heating. Microwave-infrared combination was modeled by Haala and Wiesbeck (2002)[24] using the FDTD method and by Almeida (2005)[25] using FEM. Detailed analyses of speed and uniformity of heating for individual heating modes and their combinations were, however, not done in these studies. Recently, a microwave-jet impingement system has been studied using a computational model[26]. These computational models, however, have not shown detailed validation of spatial temperature information. Moreover, the present work aims at studying a novel radiant, forced air and microwave combination system that has not been studied earlier.

2.2.3 Experimental Validation of Microwave Heating

Researchers have explored various methods to measure temperatures during microwave and microwave combination heating for the validation of computational models[27]. Methods such as measurement of surface temperatures using infrared thermography camera[3,28] or thermosensitive paper[24] and point temperature measurement inside the food using fiber optic temperature probe[18] have been used for validation in the past. However, there are limitations associated with these techniques. Use of thermography camera is limited by the fact that it can measure temperature profiles only for the exposed surface. Microwaves heat the food load volumetrically and leads to formation

of hot and cold spots inside the food. Therefore, measurement of temperature distribution in the three dimensions becomes critical in the study of microwaves. In case of fiber optic probes as well, there is a limit to the number of probes that can be used for measuring temperature inside the food. Additionally, fiber optic probes cannot be used in combination ovens as they can be damaged due to contact from heated surfaces. Magnetic resonance imaging (MRI), therefore, provides an ideal method for mapping temperatures in three dimensions with high resolution[29]. MRI has been used for temperature mapping in microwave heating studies[30–32]. These studies have been purely experimental and/or for microwave only heating. The technique has not been used in conjunction with mathematical modeling and for microwave combination heating for detailed understanding of the combination heating processes.

2.2.4 Present Study

A physics-based mathematical model to obtain temperatures, coupled with temperature validation using MRI can provide the most comprehensive understanding of the microwave combination heating process. This would be novel and is critical for the design and development of combination heating processes and equipment. The present study, therefore, aims to mathematically model radiant, forced air and microwave combination heating and subsequently verify the model using MRI measurements. The specific objectives are:

1. To compare combination heating patterns as measured by MRI with those predicted by a coupled electromagnetics- heat transfer model.
2. Quantify the speed and uniformity of heating obtained from different heating modes and their combinations.

3. Study the effect of food dielectric properties on combination heating.
4. Delineate the nature of individual heating modes and their combinations, from 1, 2 and 3.

This chapter is organized as follows. A coupled electromagnetics and heat transfer model is developed and solved to obtain the temperature distribution inside food analogues of different compositions (representing different properties) heated in a combination oven using four different heating combinations. MRI is used to obtain the 3D temperature maps inside the food analogues. Results from the simulations and experiments (MRI) are compared with each other and the heating patterns, effect of composition and heating modes are discussed. Finally, quantitative analyses of speed and uniformity of heating for the different cases are done.

2.3 Mathematical Model

2.3.1 Oven geometry and heating modes

The oven used in this study was GE Profile oven (Model no. JT930BHBB, GE, Inc., Louisville, KY) (Figure 2.1). The oven heats the food placed inside using a combination of hot air and microwaves. The air is heated by the heating elements present at the top, bottom and the back walls of the oven and the air is circulated by a rotating fan at the back of the oven. Microwaves are introduced from the waveguide on the top of the oven. One or more of the features can be turned on using the settings provided in the oven to heat the food in a desired manner. Three different settings of the oven were selected to be used for heating the samples in this study. These settings are shown in Table 2.1.

Table 2.1: Different settings of the oven used in this study and the corresponding active heating modes (see Figure 2.1 for locations). Note that the settings are built into the oven and the modes of heating within a setting are not controllable individually. Also, Settings 2 and 3 are not simply microwaves added to Setting 1.

Setting	Heating Method	Oven Temperature (°C)
1	Upper element, Lower element, Fan	80
2	Back element, Fan, Microwave (Cycling: 54 s on, 6 s off)	80
3	Upper element, Fan, Microwave (Cycling: 20 s on, 10 s off)	110

Setting 1 does not use the microwaves to heat the food whereas settings 2 and 3 heat the food load using a combination of microwave and other methods. The oven does not provide the ability to heat the food with only microwaves.

2.3.2 Governing Equations and Boundary Conditions for Electromagnetics

The electromagnetic field distribution inside the microwave cavity including the load is governed by Maxwell's equations. The Maxwell's equations of electromagnetics were solved to obtain the electric field inside the oven cavity and gel sample and coupled with heat transfer to obtain the temperatures inside the sample. The Maxwell's equations for constant permittivity and permeability, with no sources can be written as:

$$\nabla \times \mathbf{E} = -j\omega\mu\mathbf{H} \tag{2.1}$$

$$\nabla \times \mathbf{H} = j\omega\epsilon_0\epsilon\mathbf{E} \tag{2.2}$$

$$\nabla \cdot \mathbf{E} = 0 \tag{2.3}$$

$$\nabla \cdot \mathbf{H} = 0 \tag{2.4}$$

(a)

(b)

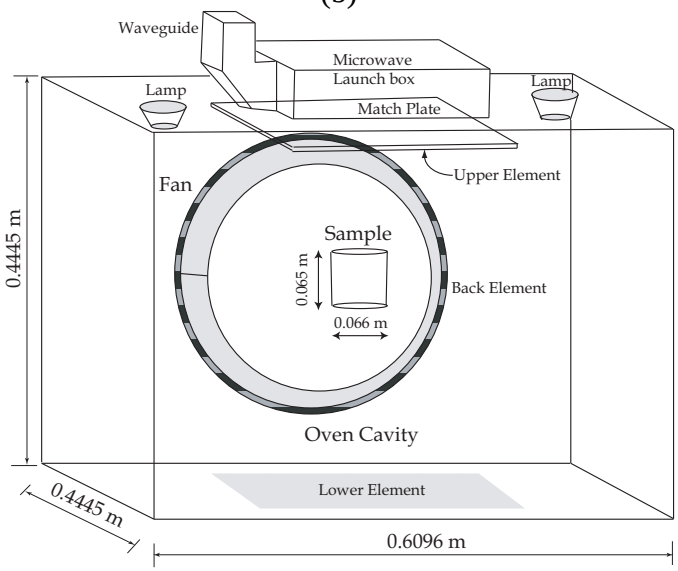

Figure 2.1: (a) GE Profile Single Wall Oven (Model JT930BHBB), used in this study; (b) Schematic of the oven used for the computations. Upper, lower and back elements provides heat and the fan circulates the hot air inside the oven. Microwaves are launched from the top.

Here, **E** is the electric field intensity and **H** is the magnetic field intensity, both defined as time harmonics:

$$\mathbf{E}(x, y, z, t) = \mathbf{E_0}(x, y, z)\, e^{j\omega t} \tag{2.5}$$

$$\mathbf{H}(x, y, z, t) = \mathbf{H_0}(x, y, z)\, e^{j\omega t} \tag{2.6}$$

where ω is the angular frequency. The complex relative permittivity, ϵ, is defined as:

$$\epsilon = \epsilon' - j\epsilon'' \tag{2.7}$$

Here, ϵ' is the dielectric constant and ϵ'' is the dielectric loss factor. ϵ_0 is the permittivity of free space.

Boundary Conditions

The walls of the oven were assumed to be perfect electric conductors and hence the tangential component of the electric field was set to zero.

$$E_{tangential} = 0 \tag{2.8}$$

Excitation

The excitation for the microwave oven is through a rectangular waveguide. The shape of the waveguide is designed to transmit maximum possible power from the magnetron to the cavity and the dominant mode of the transverse electric (TE) waves is the TE_{10} mode.

Power Loss Calculation

Power absorbed per unit volume at any location, P, by the food from the microwaves is given by:

$$P(x, y, z, t) = \frac{1}{2}\omega\epsilon_o\epsilon''|\mathbf{E}|^2 \tag{2.9}$$

where $|\mathbf{E}|$ is the magnitude of the electric field.

2.3.3 Governing Equations and Boundary Conditions for Heat Transfer

The transient diffusion equation with source term for the volumetric heating due to microwaves was solved to obtain temperatures inside the food:

$$\rho c_p \frac{\partial T}{\partial t} = k\nabla^2 T + P(x, y, z, t) \tag{2.10}$$

For oven setting 1 that did not use the microwaves, the source term, P, was set to zero.

Boundary Conditions

Heat transfer due to the three elements (top, bottom and back) and the fan was modeled using a surface heat transfer coefficient determined experimentally (discussed later).

$$-k\nabla T = h_c(T - T_a) \tag{2.11}$$

where h_c is the convection heat transfer coefficient over a surface and T_a is the temperature of air inside the oven. The oven was preheated to 80°C for settings 1 and 2 and to 110°C for setting 3 and these values were used for T_a. The initial temperature of the food was 22°C. These input values are also provided in Table 2.2.

Table 2.2: Input parameters used in the simulations

Parameter	Value
Oven dimensions (m)	$0.6096 \times 0.4445 \times 0.4445$
Food dimensions (m)	0.033 (r) $\times$ 0.065 (h)
Heating times (s)	30, 120
Microwave frequency (GHz)	2.45
Excitation amplitude (A/m)	20
Water $\epsilon' - j\epsilon''$(at 2.45 GHz)	78 - j 12.5
Air ϵ	1
TX151 gel without salt	
$\epsilon' - j\epsilon''$ (at 2.45 GHz)	69.3 - j 16
Thermal conductivity, k (W/m K)	0.55
Specific heat, c_p (J/kg K)	3655
Density, ρ (kg/m^3)	1000
TX151 gel with 4% salt	
$\epsilon' - j\epsilon''$ (at 2.45 GHz)	63.3 - j 51.7
Thermal conductivity, k (W/m K)	0.55
Specific heat, c_p (J/kg K)	3655
Density, ρ (kg/m^3)	1000
Heat transfer coefficient (W/m^2 K)	
Settings 1 and 2	22
Settings 3	35
Natural convection	10
Oven temperatures (°C)	
Settings 1 and 2	80
Settings 3	110

Numerical Solution

Equations 2.1 and 2.2 can be expressed solely in terms of electric field intensity, **E**, using Equations 2.3 and 2.4.

$$\nabla^2 \mathbf{E} + \omega^2 \mu \, \epsilon_0 \, \epsilon \, \mathbf{E} = 0 \tag{2.12}$$

Equation 2.12 for electromagnetics was solved using the FEM based commercial code ANSYS v.9 (Canonsburg, PA, U.S.A) with boundary condition given by Equation 2.8.

The geometry and mesh were created in ANSYS itself. Figure 2.2 shows the mesh of the oven cavity. Extremely fine mesh was used inside the sample (Figure 2.2) as

the wavelengths inside the sample are smaller (∼15 mm) compared to the surrounding air (∼122 mm). The finite element mesh consisted of tetrahedral volume elements. Mesh convergence study was performed to confirm that the results were independent of the mesh. Figure 2.3 shows the power absorbed in the dielectric load as a function of total number of elements in the mesh. Based on this convergence study, the total number of elements used were 1,270,484 for the electromagnetic analysis. The heat conduction equation was solved in another finite element solver, COMSOL (COMSOL Inc., Burlington, MA). The geometry that consisted of the gel sample only and the mesh with 12,900 prismatic elements were created in COMSOL. The power density (Equation 2.9) obtained from the electromagnetic analysis in ANSYS was input into COMSOL as source term, P, in the heat transfer equation (Equation 2.10).

2.4 Experimental Methodology

2.4.1 Test Material

TX151 (Oil Center Research International, Lafayette, LA), an organic hydrophilic polymer mixed with water was used as the food simulant for this study. TX151 based gels have been used extensively in previous microwave heating studies[29,33] using MRI as it resembles slow heating food, does not melt and preserves induced heating patterns for thermal image validation. In addition, water content is high which is required to achieve good signal-to-noise image during MRI.

TX151 powder (1 part) was mixed with water (10 parts by weight) and preconditioned to form the gel. To simulate foods with varying dielectric constant, another sample was prepared by adding 4% salt by weight. The gel samples were heated for 30 s at

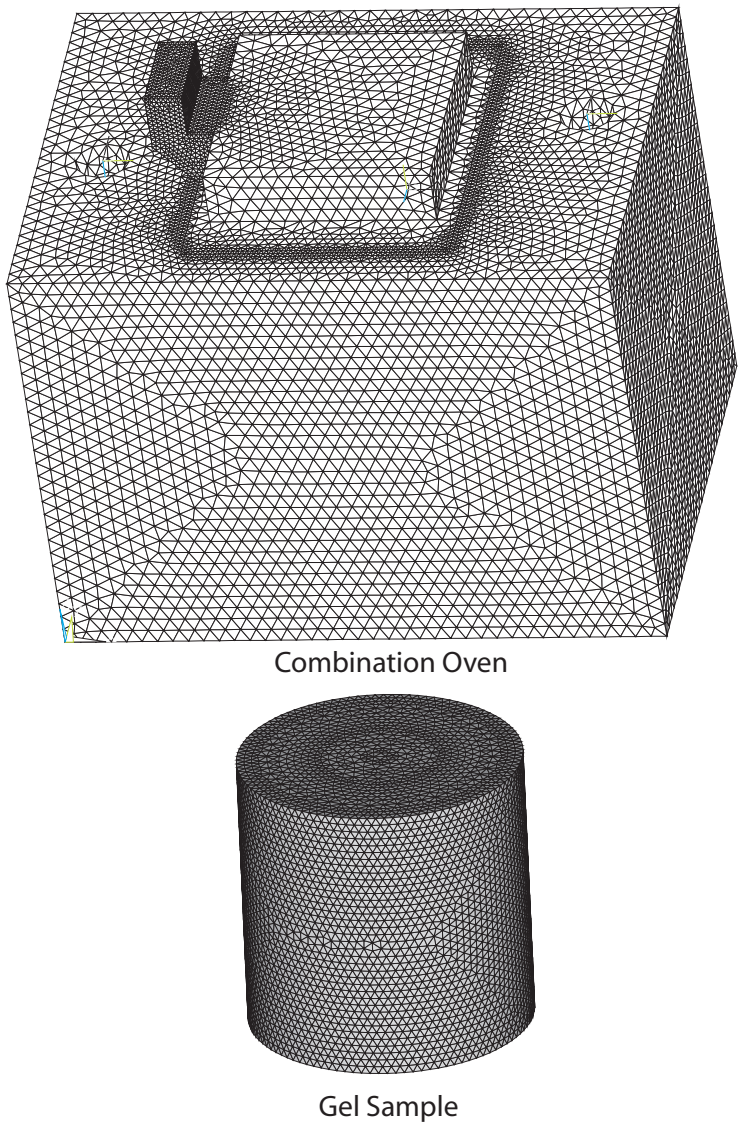

Figure 2.2: The volume mesh consisting of tetrahedral elements created in ANSYS used for the computations. The total number of elements in the mesh were 1,270,484 based on mesh convergence analysis (Figure 2.3).

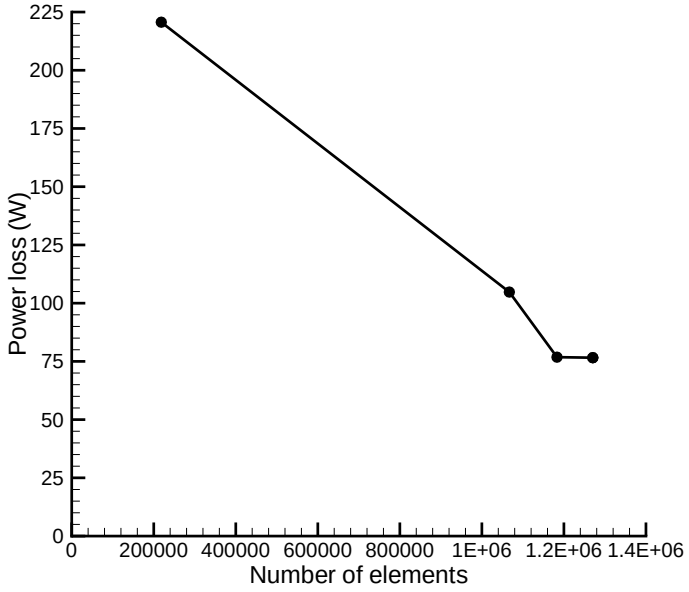

Figure 2.3: Power absorbed in the load as a function of total number of elements (tetrahedral) in the mesh consisting of the oven and load. The results reported in the study used 1,270,484 elements.

the center of the oven cavity using the 4 different settings discussed earlier (Table 2.1).

2.4.2 Microwave Combination Oven

The oven used for the study has been already described in Section 2.3.1. An identical oven was shipped to Cambridge, UK, and was used for the MRI experimentation. The oven was run using a generator to convert the voltage and frequency to the prescribed values (240 V, 60 Hz) same as those used at Cornell. The same method was used for the preparation of gel samples at both places. The MRI measurements were done off-line. The gel samples were heated in the oven for 30 s using the oven settings discussed in Section 2.3.1 and then taken out and placed in the sample holder which was then inserted inside the magnet for the measurement of temperatures.

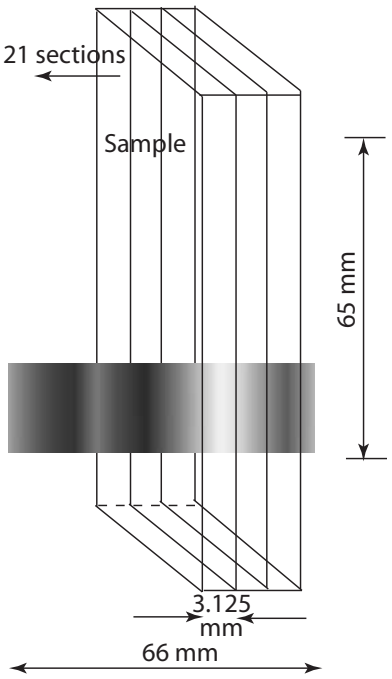

Figure 2.4: Vertical slices 3.125 mm wide along the food at which the temperature contours were mapped using MRI. The MRI spatial resolution was 3.125 × 0.78125 × 3.125 mm. Note that the slices will progressively increase in width from one side to the center and decrease as the other side is approached.

2.4.3 Magnetic Resonance Imaging (MRI)

All MRI measurements were done at the University of Cambridge, UK. MRI 3-D temperature maps were acquired using a 2 Tesla, 100 cm bore magnet. The phase difference between the heated and room temperature reference images was calibrated linearly against temperature to obtain the maps[29]. The scan time was 51.2 s for a 32 × 128 × 32 matrix. This corresponds to a spatial resolution of 3.125 × 0.78125 × 3.125 mm. These specifications resulted in 21 slices which were 3.125 mm wide and represented different vertical section in the gel (Figure 2.4). The reason for choosing vertical sections in favor of horizontal was that vertical sections present a better illustration of the penetration of microwaves inside the load.

2.4.4 Input Parameters

Input parameters required for the computational model such as gel properties (dielectric and thermal), heat transfer coefficients and input excitation were determined through experiments and are shown in Table 2.2. There was no appreciable change in the thermal and dielectric properties for the short duration of heating and hence, constant values of properties were used for the simulations.

Dielectric properties

The dielectric properties were measured using HP85070 open ended coaxial high temperature probe (Agilent Technologies, Inc., Palo Alto, CA) and a S parameter network analyzer (Agilent 8722ES, Agilent Technologies, Inc., Palo Alto, CA). Measurements were made at a frequency of 2.45 GHz and calibration was done by measurements on air, short and distilled water.

Thermal properties

Thermal conductivities of the samples were measured experimentally using a thermal properties meter (KD2, Decagon Devices, Inc., Pullman, WA). Specific heat capacities of the samples were measured using differential scanning calorimeter (Q1000 DSC, T. A. Instruments, New Castle, DE). Densities of the samples were measured separately.

Heat transfer coefficient

The surface heat transfer coefficients for different heating modes were obtained experimentally. Point temperature histories were measured by thermocouples and heat flux

was measured by heat flux sensors (HFS-3, Omega, Inc., Stamford, CT) connected to FLUKE data acquisition Bucket (Fluke Co., Everett, WA). Using the values of heat flux, q'', food surface temperature, $T_{surface}$ and ambient oven temperature, T_{oven}, heat transfer coefficient was calculated from:

$$h_c = q''/(T_{surface} - T_{oven}) \tag{2.13}$$

It was assumed that the heat transfer coefficient was constant for the period of heating. Since MRI measurements were done off-line, a natural convection heat transfer coefficient of 10 W/m^2 K was assumed for the time lag between the heating process and measurement (i.e., the time to transfer sample from oven to magnet).

Input Excitation

Microwave power was determined experimentally using water as the load in the oven and measuring the heating time for a fixed rise in temperature of water[34]. The waveguide characteristics were prescribed by specifying the width, height and amplitude of the longitudinal magnetic field component for the TE_{10} mode. To obtain the amplitude of the longitudinal component of magnetic field, microwave power absorbed in the dielectric (water load) corresponding to an arbitrary value of specified amplitude was calculated by modeling the water load inside the microwave oven and solving the Maxwell's equations. By subsequent trials, the exact value of amplitude was determined that resulted in the measured value of power obtained from the water heating experiment (Details can be seen in Zhang and Datta (2000)[23] for example). This value of the amplitude was used as the input excitation for all subsequent calculations.

2.5 Results and Discussions

2.5.1 Radiant and Forced Air Heating (Setting 1)

Setting 1 of the oven uses radiant heating from the upper and lower elements together with forced air from the fan located at the back. Figure 2.5 compares the simulation with MRI measurements for the temperature distribution in the gel samples without and with salt heated using Setting 1. There is insignificant heating in the sample without salt as can be observed from the temperature contours. Figure 2.9a shows that average temperature rises by only about 1°C at the end of 30 s. Likewise, for the sample with salt (Figure 2.5b), there is no appreciable rise in temperature, as expected, since the thermal properties of the two samples are the same (Table 2.2). The small increase in temperature in setting 1 is mostly at the surface due to convection and predominantly at the bottom since the sample was in contact with the metal rack of the oven.

2.5.2 Microwave-only heating (Simulation only)

The oven used for the study does not support microwave only heating. In order to assess the effect of microwave on conventional modes of heating, the hypothetical case of microwave-only heating was simulated. Figure 2.6 shows the simulated temperature contours for microwave-only heating for the two samples. It can be observed that due to the penetration of the microwaves, deeper locations of the sample are heated compared to radiant-forced air heating (setting 1) and there is preferential heating at the edges of the cylindrical gel samples. Higher temperatures at the edges and surface are observed in the sample with salt (Figure 2.6). The average temperatures in the sample with salt are, however, marginally lower compared to sample without salt (Figure 2.9a) showing

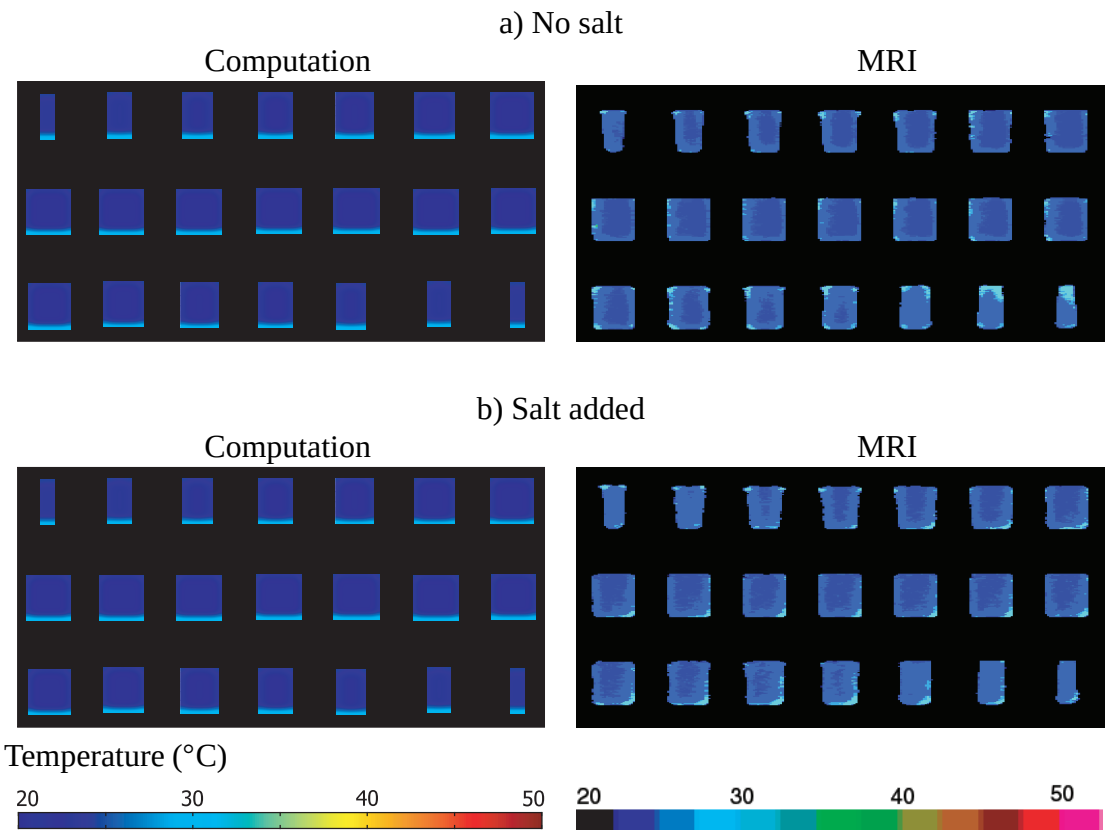

Figure 2.5: Temperature distribution in 21 vertical slices in the gel samples obtained from computations and MRI after 30 s of heating in the combination oven shown in Figure 2.1 for setting 1 (Table 2.1). Gel sample without salt is shown at the top (a) while the sample with salt is shown at the bottom (b). Initial temperature of the samples was 22°C (room temperature). Orientation of the slices are shown in Figure 2.4.

that the microwaves do not heat deeper locations in this case. This is due to reduced penetration of the microwaves as a result of significantly larger dielectric loss in the sample with salt (Table 2.2) indicating that microwave heating depends greatly on the dielectric properties of the food material. The average temperatures for the 30 s of heating for both samples, shown in Figure 2.9, were greater than setting 1 that do not use microwaves demonstrating the faster rate of heating of microwaves in this instance.

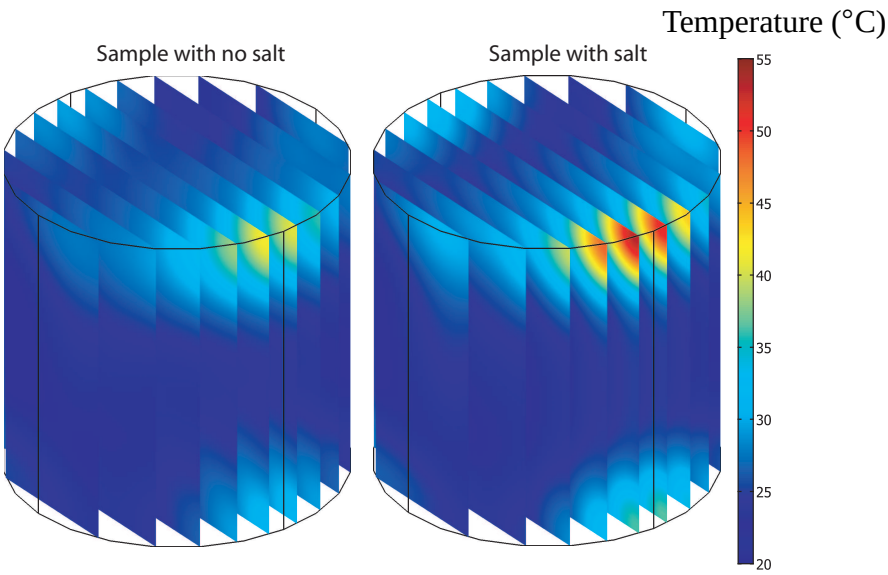

Figure 2.6: Computed temperatures inside the gel samples after 30 s of heating if only microwaves are used. Initial temperature of the samples was 22°C (room temperature). Here the slices are shown in a 3D configuration as opposed to those in Figures 2.5, 2.7 and 2.8.

2.5.3 Combination Radiant, Forced Air and Microwave Heating (Setting 2)

Setting 2 uses radiant heating from the back element, forced air from the fan and microwaves from the top of the oven. The sample was heated using setting 2 to investigate heating patterns obtained when a combination of the radiant-forced air and microwave heating modes discussed above are used. Figure 2.7 presents the temperature maps inside the gel for combination heating (Setting 2) of the oven.

Figure 2.7a shows that the corners of the slices (corresponding to the edges of the cylinder) are preferentially heated with the top left corner of the slices (corresponding to the top left region of the cylinder) being heated the most, consistent with microwave only heating shown in Figure 2.6. For the sample with salt (Figure 2.7b), similar patterns can be observed with higher temperature at the corner and edge of the corresponding slices

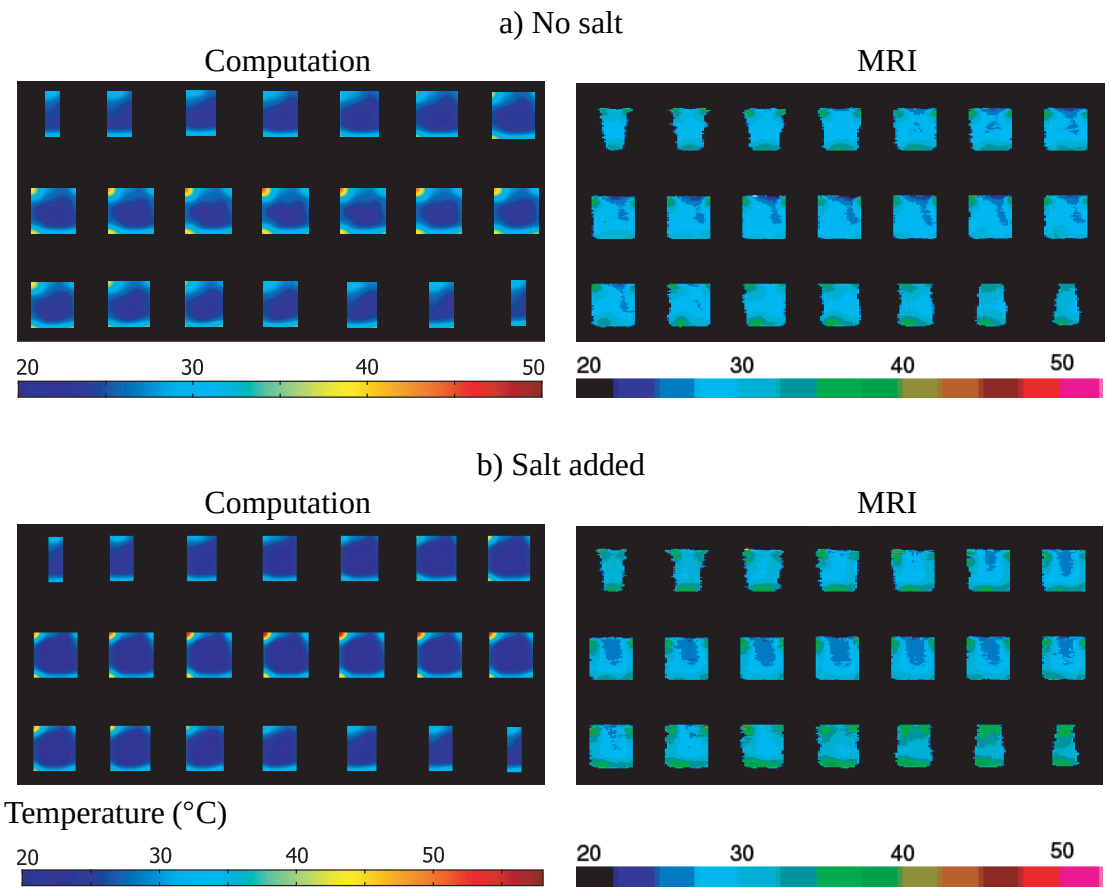

Figure 2.7: Temperature distribution in 21 vertical slices in the gel samples obtained from computations and MRI after 30 s of heating in the combination oven shown in Figure 2.1 for setting 2 (Table 2.1). Gel sample without salt is shown at the top (a) while the sample with salt is shown at the bottom (b). Initial temperature of the samples was 22°C (room temperature). Orientation of the slices are shown in Figure 2.4.

without salt due to smaller penetration of the microwaves. For both samples, without salt and with salt, the top and sides are heated primarily by the hot air and the bottom is heated primarily by contact with the metal grill on which the sample is placed. The temperature profile obtained for this case is, therefore, a combination of the heating patterns obtained from the radiant and forced air heating and microwave only heating along with contact heating. The average temperatures for the 30 s of heating are higher than both setting 1 and microwave only heating, as shown in Figure 2.9. Qualitatively, the heating profile looks more uniform compared to microwave only heating, since in

microwave only heating (Figure 2.6) the majority of the curved surface of the sample that was not heated is heated in this case by addition of radiant heat and forced air and the bottom that was not heated is now heated by contact. Detailed quantitative analyses of speed and uniformity of heating are done in a later section (Section 2.5.5)

2.5.4 Combination Radiant, Forced Air and Microwave Heating (Setting 3)

To investigate the effect of using a different combination of the heating modes (radiant, forced air and microwave), setting 3 of the oven was chosen. For setting 3, microwaves are on for 20 s (Table 2.1) and the heat transfer coefficient (Table 2.2) and oven temperature (110°C) are higher compared to setting 2. The temperature distribution inside the gel samples during combination heating (Setting 3) obtained from computation and MRI are shown in Figure 2.8.

Heating patterns in this case are similar to setting 2 with the corners of the slices preferentially heated by microwaves and the top left corner of the slices heated the most. However, the top and sides that are heated by hot air and the bottom that is heated by contact are at higher temperatures compared to setting 2 due to higher heat transfer coefficient and oven temperature. The final temperatures are similar (Figure 2.9) due to decreased heating by the microwaves which are on for 20 s as opposed to the entire 30 s of heating in setting 2. Similar to setting 2, higher surface temperatures are obtained for the sample with salt due to reduced penetration of the microwaves. However, this effect is less enhanced compared to setting 2 as the microwaves are on for a smaller time. Detailed quantitative analyses of speed and uniformity of heating for the different heating modes are done in the next section.

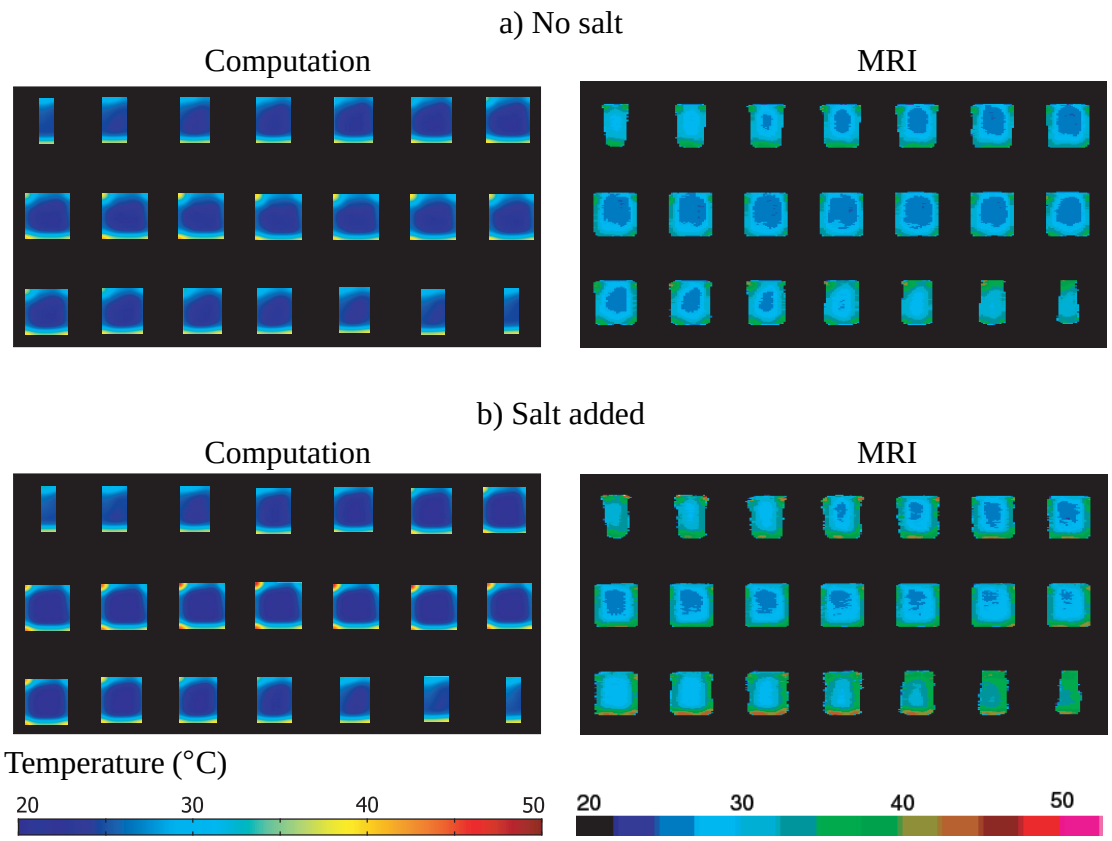

Figure 2.8: Temperature distribution in 21 vertical slices in the gel samples obtained from computations and MRI after 30 s of heating in the combination oven shown in Figure 2.1 for setting 3 (Table 2.1). Gel sample without salt is shown at the top (a) while the sample with salt is shown at the bottom (b). Initial temperature of the samples was 22°C (room temperature). Orientation of the slices are shown in Figure 2.4.

2.5.5 Speed of heating and uniformity

Measure of speed and uniformity of heating

For this study, speed of heating is quantified by the rate of increase of average temperature with time. As discussed in Section 2.2, non-uniformity of temperatures is a known problem during microwave heating of food and as a result, microwave ovens have been used mostly in reheating of foods rather than cooking. Combination heating may help in overcoming the problem of non-uniform heating when temperature profiles from each

individual mode of heating complement each other. It is therefore important to quantify the temperature uniformity to evaluate the different heating methods. Temperature non-uniformity will be quantified using coefficient of variation (COV), as was reported by Geedipalli et al. (2007). COV is defined as the ratio of the standard deviation to the mean of a data set. Higher COV values would signify more non-uniformity of heating.

Rate and uniformity of heating when considering contact heating from the grill

a) Sample without salt As will be shown, contact heating from the metal grill on which the food is placed contributes significantly to heating rate and uniformity. For this section, we consider this heating effect. Figure 2.9a shows the transient average temperatures for various oven settings (given in Table 2.1). The average temperature increases linearly with time for radiant hot-air (Setting 1) and for microwave only heating when the microwaves are on continuously. For combination heating (Settings 2 and 3), microwaves are cycled and therefore the temperatures show cycling. The power cycling is different for the two settings (54 s on and 6 s off for Setting 2; 20 s on and 10 s off for Setting 3), leading to different temperature histories. As expected, combination heating (Settings 2 and 3) is faster than radiant-forced air heating or microwave-only heating by itself. Although contributions by the individual heating modes are different, the heating rates of the two combination heating settings are comparable.

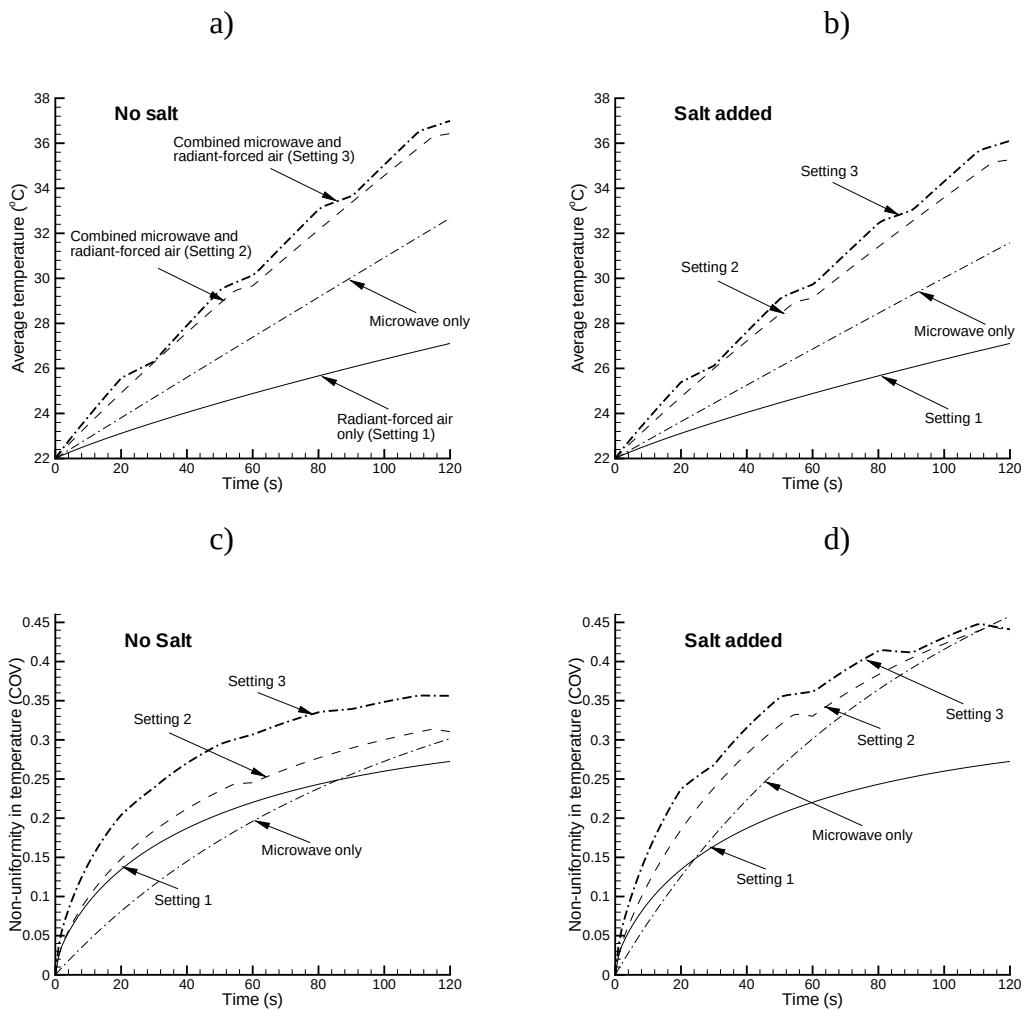

Figure 2.9: Computed average temperatures and non-uniformity in temperatures (with coefficient of variation or COV as the measure) of the gel samples as functions of heating time for four modes of heating: radiant-forced air only (setting 1), microwave only, and combination radiant-forced air and microwave heating modes (setting 2 and 3). Settings are described in more details in Table 2.1. Contact heating (Section 2.5.5) is considered here for Settings 1, 2, and 3.

Figure 2.9c shows that the COV, a measure of non-uniformity of heating, increases with time during this short duration of heating. However, for radiant-forced air heating (Setting 1), the value of COV tends to level off indicating that as time progresses the temperature uniformity inside the samples improves. This is because the heating process depends on conduction and as more heat from the surfaces diffuses inside, the

temperatures become more uniform. For microwave only heating, spatially non-uniform rates of energy absorption lead to spatially varying rates of heating, thereby increasing non-uniformity of temperature with time, as shown by the increase in COV. In case of combination heating (Settings 2 and 3), COV values depend on modes of heating used and the cycling of the microwaves. It can be seen that the speeds of the combination heating (Settings 2 and 3) are roughly the summation of the individual modes (radiant-forced air only and microwave only) (Figure 2.9a). However, the non-uniformities of heating in the combination settings are considerably less than the summation of those in the individual modes (Figure 2.9c). This indicates that although the speed of heating increases appreciably for combination modes, the non-uniformity of heating does not increase as much. Nevertheless, it is evident that radiant-forced air only and microwave only modes do not provide absolutely complementary heating patterns, since the combination of these individual modes (in Settings 2 and 3) does not lead to the decrease in the non-uniformity of heating.

COV values for microwave only heating for the sample without salt are less than the corresponding values for radiant-forced air and combination heating, suggesting that microwave only heating is more uniform in this case. However, contact heating is significant in case of radiant-forced air and combination heating, as discussed in the previous section. The greater non-uniformity in the sample during convection and combination heating may have been contributed by contact heating since the sample is heated preferentially at the bottom. To investigate the effect of radiant-forced air and combination heating only without contact at the bottom, the COV was calculated for the case of the sample bottom being heated by hot air and is discussed in Section 2.5.5.

b) Sample with salt The heating rates for the four settings in the sample with salt are similar to those in the sample without salt, as shown in Figures 2.9a and 2.9b. The spa-

tial temperature profiles were, however, found, to be different for microwave-only and combination heating modes and were discussed earlier (Sections 2.5.1-2.5.4). For Setting 1, the non-uniformity of temperatures for the sample with salt is same as that for the sample without salt (Figures 2.9c and 2.9d), as expected since the thermal properties of the two samples are the same. However, for microwave only heating, the non-uniformity of heating is considerably greater compared to the sample without salt. This is because the microwave heating depends on the dielectric loss of the material, as given by Equation 2.9 and therefore, for a material with higher dielectric loss (sample with salt), the spatial non-uniformity due to microwave heating increases. For combination heating (Settings 2 and 3), the effect of microwave cycling on the COV values is visible more in case of sample with salt compared to sample without salt, consistent with greater non-uniformity during heating of a more lossy material (sample with salt). In addition, as opposed to the sample without salt, non-uniformities during microwave only and combination heating are considerably higher compared to those for radiant-forced air heating, even while considering contact heating. These further indicate that the microwave contributes significantly to temperature non-uniformity for materials with high dielectric loss.

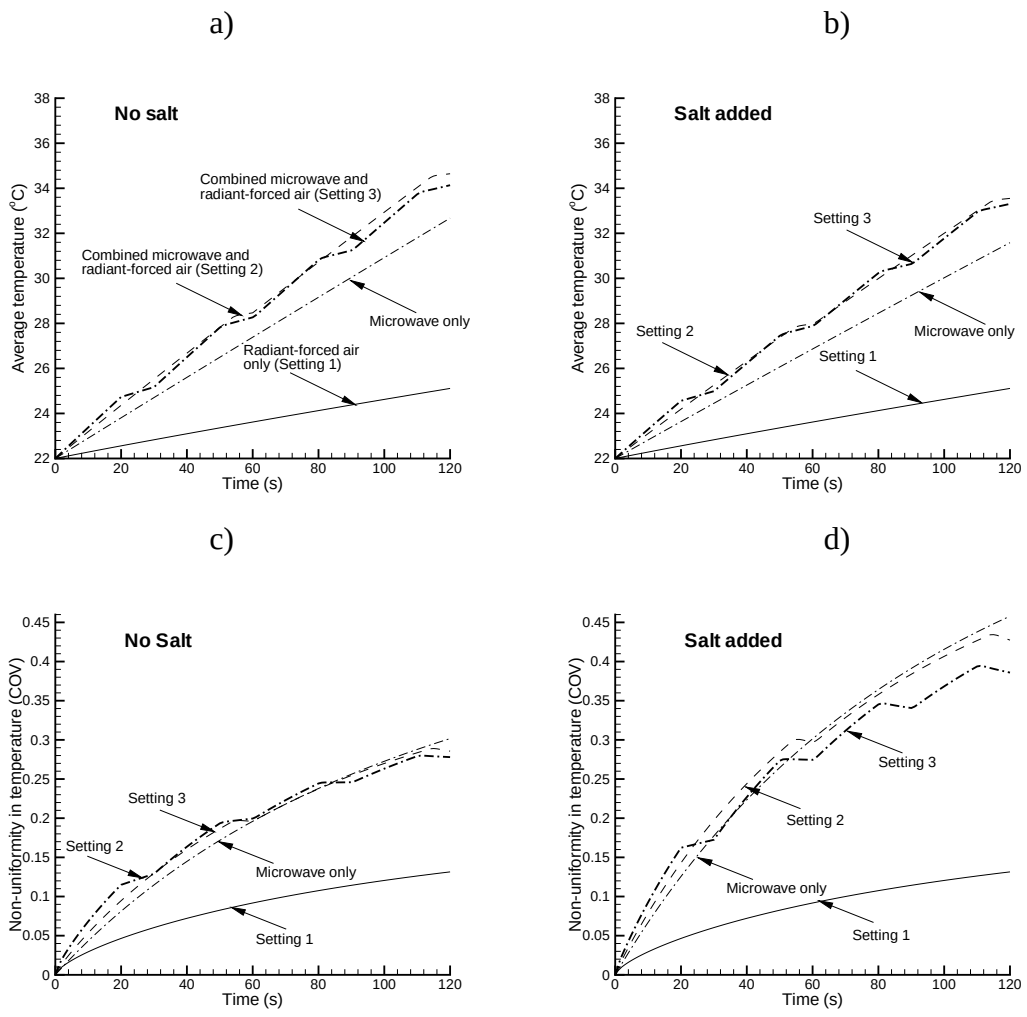

Figure 2.10: Computed average temperatures and non-uniformity in temperatures (with coefficient of variation or COV as the measure) of the gel samples as functions of heating time for four modes of heating: radiant-forced air only (setting 1), microwave only, and combination radiant-forced air and microwave heating modes (setting 2 and 3). Contact heating is not considered here for Settings 1, 2 and 3 (Section 2.5.5). Settings are described in more details in Table 2.1.

Rate and non-uniformity of heating without considering contact heating from the grill

Since contact heating from the grill seems to play a significant role, simulations were run with the samples heated by convection at the bottom but without contact heating

from the grill. Average temperatures histories for this case are shown in Figures 2.10a and 2.10b. Combination heating methods (Settings 2 and 3) although still faster compared to Setting 1 and microwave-only heating, temperatures for Settings 1,2 and 3 are several degrees lower due to the absence of the contact heating of the grill. With the contribution of the grill to non-uniformity removed, the combination heating (Settings 2 and 3) becomes comparable in non-uniformity to microwave heating (Figure 2.10c) even with higher average temperatures. Perhaps another way to interpret this is that microwaves are the primary contributor to non-uniformity in Settings 2 and 3. For the sample with salt, non-uniformity for combination heating Setting 3 is eventually lower than microwave heating while maintaining a higher rate of heating than microwaves alone (Figures 2.10b). This is because of lower microwave power (on for 80 s; off for 20 s) and more of radiant-forced air heating in Setting 3 than microwave only heating and Setting 2 (on for 108 s; off for 12 s).

2.6 Summary and Conclusions

A novel mix of physics-based computation and MRI experimentation was used for the detailed study of heating that combines infrared, forced air and microwaves. The effects of processing variables such as heat transfer coefficient, oven temperature and microwave cycling, and food factor such as dielectric properties on the uniformity of heating were evaluated. The modes of radiant heating through heating elements and forced convection by fan lead to more uniform heating compared to the faster (but less uniform) heating method provided by the microwaves. Heating uniformity of the samples heated using combination heating depends on the type of combination and the contribution of the different heating methods. These results lead to the fact that an optimum combination of heat transfer coefficient, oven temperature and microwave cycling, while

considering the food properties, can be developed that can speed up the process of heating while maintaining the heating uniformity at the same time. The results from the study can be used to develop design recommendations/ guidelines for combination heating for different heating processes such as baking, broiling, roasting and reheating for different materials grouping them based on their properties.

Although comparison of results obtained from the finite element based computational model and MRI experimentation was made, detailed quantitative analysis was not possible. The temperature maps obtained from MRI are averaged over a volume that depends on the spatial resolution used for obtaining the MR images whereas for the FEM model it depends on the mesh density used. The spatial resolution for MRI was $3.125 \times 0.78125 \times 3.125$ mm (corresponding to a pixel distribution of $32 \times 128 \times 32$) in this case. For a greater precision, the obvious solution would be to increase the spatial resolution. However, increasing the spatial resolution would also increase the scan time which in turn would not be a very accurate means of measuring the temperatures for the heating process. For example, the resolution used in this study resulted in a scan time of 51.2 s. If the resolution was increased to $0.390625 \times 0.78125 \times 0.78125$ mm (corresponding to a pixel distribution of $256 \times 128 \times 128$), the scan time would increase to 819.2 s or about 14 min. The unavailability of quantitative MRI data due to closure of the facility in Cambridge prevented making additional quantitative comparisons. As a result, similar color schemes and limits for the temperature color bars in the computed and MRI results could not be used that made these look visually different. However, as discussed throughout Section 4, several qualitative features compare well between the computed and MRI results.

2.7 Acknowledgements

This research was supported by grant number 2003-35503-13737 from the United States Department of Agriculture under the National Research Initiative Grant Program. This work was also partially supported by the National Center for Supercomputing Applications under CTS040034N and utilized the Copper system.

BIBLIOGRAPHY

[1] Datta AK, Ni H. Infrared and hot-air-assisted microwave heating of foods for control of surface moisture. *Journal of Food Engineering*. 2002;51(4):355-364.

[2] Watanabe M, Suzuki M, Ohkawa S. Analysis of Power-Density Distribution in Microwave Ovens. *Journal of Microwave Power and Electromagnetic Energy*. 1978;13(2):173-181.

[3] Wappling-Raaholt B, Scheerlinck N, Galt S, Banga JR, Alonso A, Balsa-Canto E, Van Impe J, Ohlsson T, Nicolai BM. A combined electromagnetic and heat transfer model for heating of foods in microwave combination ovens. *Journal of Microwave Power and Electromagnetic Energy*. 2002;37(2):97-111.

[4] McMinn WAM, McLoughlin CM, Magee TRA. Microwave-convective drying characteristics of pharmaceutical powders. *Powder Technology*. 2005;153(1):23-33.

[5] Jumah RY, Raghavan GSV. Analysis of heat and mass transfer during combined microwave-convective spouted-bed drying. *Drying Technology*. 2001;19(3-4):485-506.

[6] Ren G, Chen F. Drying of steamed Asian ginseng (Panax ginseng) roots by microwave-hot air combination. *Pharmazie*. 2000;55(2):124-128.

[7] Khraisheh MAM, Cooper TJR, Magee TRA. Microwave and air drying I. Fundamental considerations and assumptions for the simplified thermal calculations of volumetric power absorption. *Journal of Food Engineering*. 1997;33(1-2):207-219.

[8] Riva M, Schiraldi A, Dicesare LF. Drying of Agaricus-Bisporus Mushrooms by Microwave Hot Air Combination. *Food Science and Technology-Lebensmittel-Wissenschaft & Technologie*. 1991;24(6):479-483.

[9] Ovadia DZ, Walker CE. Impingement in food processing. *Food Technology*. 1998;52(4):46-50.

[10] Smith DP. Food-Finishing Microwave Tunnel Utilizes Jet Impingement and Infrared Sensing for Process-Control. *Food Technology*. 1986;40(6):113-116.

[11] Nitin N, Gadiraju RP, Karwe MV. Conjugate heat transfer associated with a turbulent hot air jet impinging on a cylindrical object. *Journal of Food Process Engineering*. 2006;29(4):386-399.

[12] Sarkar A, Singh RP. Spatial variation of convective heat transfer coefficient in air impingement applications. *Journal of Food Science*. 2003;68(3):910-916.

[13] Li A, Walker CE. Cake baking in conventional, impingement and hybrid ovens. *Journal of Food Science*. 1996;61(1):188-191.

[14] Sumnu G, Sahin S, Sevimli M. Microwave, infrared and infrared-microwave combination baking of cakes. *Journal of Food Engineering*. 2005;71(2):150-155.

[15] Sumnu G, Datta AK, Sahin S, Keskin SO, Rakesh V. Transport and related properties of breads baked using various heating modes. *Journal of Food Engineering*. 2007;78(4):1382-1387.

[16] Watanabe M, Suzuki M, Ohkawa S. Analysis of Power-Density Distribution in Microwave Ovens. *Journal of Microwave Power and Electromagnetic Energy*. 1978;13(2):173-181.

[17] Zhu SZ, Chen HK. Power Distribution Analysis in Rectangular Microwave-Heating Applicator with Stratified Load. *Journal of Microwave Power and Electromagnetic Energy*. 1988;23(3):139-143.

[18] Ni H, Datta AK, Torrance KE. Moisture transport in intensive microwave heating of biomaterials: a multiphase porous media model. *International Journal of Heat and Mass Transfer*. 1999;42(8):1501-1512.

[19] Zhou L, Puri VM, Anantheswaran RC, Yeh G. Finite-Element Modeling of Heat

and Mass-Transfer in Food Materials during Microwave-Heating - Model Development and Validation. *Journal of Food Engineering*. 1995;25(4):509-529.

[20] Campanone LA, Zaritzky NE. Mathematical analysis of microwave heating process. *Journal of Food Engineering*. 2005;69(3):359-368.

[21] Ma LH, Paul DL, Pothecary N, et al. Experimental Validation of a Combined Electromagnetic and Thermal FDTD Model of a Microwave-Heating Process. *Ieee Transactions on Microwave Theory and Techniques*. 1995;43(11):2565-2572.

[22] Dincov DD, Parrott KA, Pericleous KA. A new computational approach to microwave heating of two-phase porous materials. *International Journal of Numerical Methods for Heat & Fluid Flow*. 2004;14(5-6):783-802.

[23] Zhang H, Datta AK. Heating concentrations of microwaves in spherical and cylindrical foods part two: in a cavity. *Food and Bioproducts Processing*. 2005;83(C1):14-24.

[24] Haala J, Wiesbeck W. Modeling microwave and hybrid heating processes including heat radiation effects. *IEEE Transactions on Microwave Theory and Techniques*. 2002;50(5):1346-1354.

[25] Almeida MF. Modeling infrared and combination infrared-microwave heating of foods in an oven, Ph. D. Dissertation, Cornell University. 2005.

[26] Geedipalli SSR, Rakesh V, Datta AK. Modeling the heating uniformity contributed by a rotating turntable in microwave ovens. *Journal of Food Engineering*. 2007;82(3):359-368.

[27] Datta AK, Berek H, Little DA, Ramaswamy HS. Merement and Instrumentation, In *Handbook of microwave technology for food appplications,* A. K. Datta and R. C. Ananatheswaran, eds. Marcel Dekker Inc. , New York, NY. 2001. 279-298.

[28] Bengtsson NE, Lycke E. Experiments with a heat camera for recording temperature distribution in foods during microwave heating. *Journal of Microwave Power*. 1969;4(2):48-54.

[29] Nott KP, Hall LD, Bows JR, Hale M, Patrick ML. Three-dimensional MRI mapping of microwave induced heating patterns. *International Journal of Food Science and Technology*. 1999;34(4):305-315.

[30] Bows JR, Patrick ML, Nott KP, Hall LD. Three-dimensional MRI mapping of minimum temperatures achieved in microwave and conventional food processing. *International Journal of Food Science and Technology*. 2001;36(3):243-252.

[31] Nott KP, Hall LD. Validation and cross-comparison of MRI temperature mapping against fibre optic thermometry for microwave heating of foods. *International Journal of Food Science and Technology*. 2005;40(7):723-730.

[32] Knoerzer K, Regier M, Schubert H. Microwave heating: A new approach of simulation and validation. *Chemical Engineering & Technology*. 2006;29(7):796-801.

[33] Swain MVL, Russell SL, Clarke RN, Swain MJ. The development of food simulants for microwave oven testing. *International Journal of Food Science and Technology*. 2004;39(6):623-630.

[34] Buffler CR. Microwave Cooking and Processing: Engineering Fundamentals for the Food Scientist. Van Nostrand Reinhold, New York. 1993:4-31, 157-159

CHAPTER 3

FULLY COUPLED ELECTROMAGNETICS- HEAT TRANSFER MODEL AND SIMPLE OPTIMIZATION

3.1 Abstract

Combination of heating modes such as microwaves, convection and radiant heating can be used to realistically achieve the quality and safety needed for cooking processes and, at the same time, make the processes faster. Physics based computational modeling used in conjunction with MRI experimentation can be used to obtain critical understanding of combination heating. The objectives were to- 1) formulate a fully coupled electromagnetics- heat transfer model, 2) use magnetic resonance imaging (MRI) experiments to determine the 3D spatial and temporal variation of temperatures and validate the numerical model, 3) use the insight gained from the model and experiments to understand the combination heating process and to optimize it. The different factors that affect heating patterns during combination heating such as the type of heating modes used, placement of sample and microwave cycling were considered. Objective functions were defined and minimized for design and optimization. The use of such techniques can lead to greater control and automation of combination heating process benefitting the food process and product developers immensely.

Nomenclature

Symbol	Description, units
B_o	magnetic field strength, T
c_p	specific heat capacity, J/kg K
$\mathbf{E}$	electric field intensity, V/m
h	surface heat transfer coefficient, W/m^2 K
$\mathbf{H}$	magnetic field intensity, A/m
j	imaginary unit, $\sqrt{-1}$
J	objective function, m^{3}K
k	thermal conductivity, W/m K
n	normal direction
Q	power absorbed, W/m^3
t	time, s
T	temperature, °C
T_{air}	oven temperature, °C
T_p	processing temperature, °C
TE	echo time, s
$x,\ y,\ z$	directions, m
α	proportionality constant, ppm/°C
γ	magnetogyric ratio of hydrogen nucleus, rad/s T
ϵ	complex relative permittivity, dimensionless
ϵ'	dielectric constant, dimensionless
ϵ''	dielectric loss, dimensionless
ϵ_0	permittivity of free space, 8.854×10^{-12} F/m
μ_0	permeability of free space, $4\pi \times 10^{-7}$ H/m
ρ	density, kg/m^3
φ	phase shift, rad
ω	angular frequency, rad/s

3.2 Introduction and Objectives

Increased speed of food preparation along with improved quality and safety of the final product is critical to food processing for both domestic and industrial processes. A number of heating techniques are currently used to prepare foods. However, each heating method produces its own characteristic heating profile leading to different speed, quality and safety issues depending on the heating method used. Combining different heating modes on the other hand can potentially provide customized heating profiles suitable for a particular process. At the same time combination heating can help speed up the heating process. Using microwaves with convection and radiation, known as microwave combination heating, is one such novel combination heating technique that has been found to be effective. However, systematic development, design and optimization of microwave combination heating requires comprehensive knowledge of the engineering fundamentals that govern the relationship between combined modes of heating and the final quality and safety of the prepared food. Physics based computational modeling used in conjunction with novel experimentation can provide a level of understanding of the combination heating process that may be impossible to achieve either by modeling or experiments alone. A detailed study of combination heating using computations and experiments that is needed for critical understanding of the process is not present in the literature.

Development of combination heating requires a detailed study of processing variables and food factors. Processing variables are the factors related to the combination oven such as types of modes combined, and the power levels and cycling of the different modes. Although researchers have studied different combinations such as microwave-convection[1–3], microwave-jet impingement[4,5], and microwave-infrared[6–8] using experimental and/or numerical techniques, a comprehensive work that looks into the different

oven parameters mentioned above and does a comparative study of different combinations starting from fundamental physics is missing. Sample factors refer to the properties of the sample being heated and the transport processes occurring inside. Again a detailed study that looks at the spatial variation of heating profiles through simulation and elaborate experiments has not been accomplished. Majority of the combination heating studies[1,2,9] have not looked at spatial heating, being concerned more with the overall drying rate as the application area.

In this study, we use physics based computational models to investigate the different processing variables and food factors and how they affect the final quality of the prepared food. Two-way coupling of electromagnetic heating and heat transfer is needed for accurate description of the process as the properties of food (dielectric and thermal) change with temperature. Implementation of this two-way coupling in 3D presents inherent challenges and has been rarely implemented[10,11] and moreover these studies have not looked at microwave combination heating. Validation of the computational model is critical, more so since the combination heating technique involves volume heating due to microwaves that is spatially nonuniform. Elaborate measurement techniques such as Magnetic Resonance Imaging (MRI)[12–14], that presents a precise picture of the heating profiles in 3D, have not been used earlier for validation of computational models. We use novel experiments based on MRI to obtain 3D spatial variation of heating in the samples to validate the numerical model and complement understanding. The quality of the product obtained after a cooking process is defined by the temperature inside the sample and is a result of the processing variables and food factors. Although both heat and mass (water) transfer occur inside the food during the heating process, we have limited the analysis to heat transfer to focus more on the processing variables.

The specific objectives of the work are- 1) formulation and implementation of a fun-

damental physics based fully coupled electromagnetics- heat transfer model to study microwave combination heating, 2) use of magnetic resonance imaging (MRI) experiments to determine the 3D spatial and temporal variation of temperatures obtained during combination heating, 3) quantitative comparison of the computed results with the MRI data, 4) use the insight gained from the model and experiments to understand the process of combination heating comprehensively and to thereby optimize the process.

3.3 Methods

Mathematical description of the microwave combination heating process, MRI methodology used and experimental measurement of the input parameters are now discussed.

3.3.1 Mathematical Description

Solution of the microwave combination heating problem involves two different physics: electromagnetics and transport. The Maxwell's equations of electromagnetics need to be solved to determine the electric field inside the oven cavity and sample. Knowing the electric field distribution inside the sample, power absorbed at any location can be determined. As discussed earlier, transport is limited to heat transfer. The heat balance equation is then solved using the source term for microwave heating to determine the temperatures inside the sample. This process is repeated, i.e. solution of Maxwell's equations followed by heat transfer, to incorporate changes in the dielectric properties as the temperatures change. Thermal properties are also functions of temperature and this is incorporated while solving the energy equation.

Electromagnetics

The Maxwell's equations of electromagnetics are given by:

$$\nabla \times \mathbf{E} = -j\omega\mu_0\mathbf{H} \tag{3.1}$$

$$\nabla \times \mathbf{H} = j\omega\epsilon_0\epsilon\mathbf{E} \tag{3.2}$$

$$\nabla \cdot \epsilon\mathbf{E} = 0 \tag{3.3}$$

$$\nabla \cdot \mathbf{H} = 0 \tag{3.4}$$

where **E** is the electric field intensity and **H** is the magnetic field intensity.

The dielectric constant, ϵ', and the dielectric loss factor, ϵ'', are both functions of temperature. The complex relative permittivity, ϵ, is written as:

$$\epsilon = \epsilon'(T) + j\epsilon''(T) \tag{3.5}$$

Boundary Condition The oven walls are perfect electric conductors. Therefore:

$$E_{\text{tangential, oven wall}} = 0 \tag{3.6}$$

Microwave heating term Heat absorbed by the sample per unit time due to the microwaves is given by:

$$Q(x, y, z, t) = \frac{1}{2}\omega\epsilon_o\epsilon''|\mathbf{E}|^2 \tag{3.7}$$

Heat Transfer

The sample inside the oven is heated volumetrically by microwaves. Heat conduction occurs inside the sample.

$$\rho c_p \frac{\partial T}{\partial t} = \nabla \cdot (k\nabla T) + Q(x, y, z, t) \tag{3.8}$$

Boundary Conditions Convection and radiant heating act only on the surface and are, therefore, included as boundary conditions.

$$-k \left. \frac{\partial T}{\partial n} \right|_{\text{surface}} = h \left(T - T_{\text{air}} \right) \tag{3.9}$$

where n is the direction normal to a particular surface of the sample, h is the transfer coefficient due to convection and radiant heating at that surface (determined through experiments) and T_{air} is the oven air temperature.

Input parameters

Dielectric properties of the samples (ϵ', ϵ'') as functions of temperature were determined experimentally using the HP85070 open ended coaxial high temperature probe (Agilent Technologies, Inc., Palo Alto, CA). Thermal properties (k, c_p) were measured as functions of temperature using the KD2 Pro probe (KD2, Decagon Devices, Inc., Pullman, WA). Surface heat transfer coefficients for different heating combinations were obtained by measuring point temperature using thermocouples and heat flux using the heat flux sensors (HFS-3, Omega, Inc., Stamford, CT) connected to FLUKE data acquisition Bucket (Fluke Co., Everett, WA). All input parameters are shown in Table 3.1.

Solution of governing equations

The schematic of the computational domain along with the different physics solved for in the subdomains are shown in Figure 3.1. The governing equations for electromagnetics and heat transfer are fully coupled. As temperatures in the sample change due to heating, the dielectric properties change as given in Table 3.1. This in turn changes the electric field distribution inside the oven and sample and as a result, the microwave

Table 3.1: Input parameters for the computations

Parameter	**Value**
Oven dimensions (cm)	$60.96 \times 44.45 \times 44.45$
Sample (cylindrical) dimensions (cm)	3.80 (dia) $\times$ 3.60
Thermal conductivity, k (W/m K)	$0.5313 + 0.002T$
Specific heat, c_p (J/kg K)	$3724.4 + 2.0839T$
Density, ρ (kg/m^3)	1000
Microwave frequency (GHz)	2.45
Dielectric constant, ϵ'	$66.987 + 0.1553T - 0.0011T^2$
Dielectric loss, ϵ''	$13.247 + 0.0693T + 0.0003T^2$
Heat transfer coefficient, h (W/m^2 K)	
Top surface (Settings I and III)	22
Top surface (Settings II and IV)	35
Curved surface (Settings I, II, III and IV)	20
Air temperatures (°C)	
Combinations I and III	80
Combinations II and IV	110

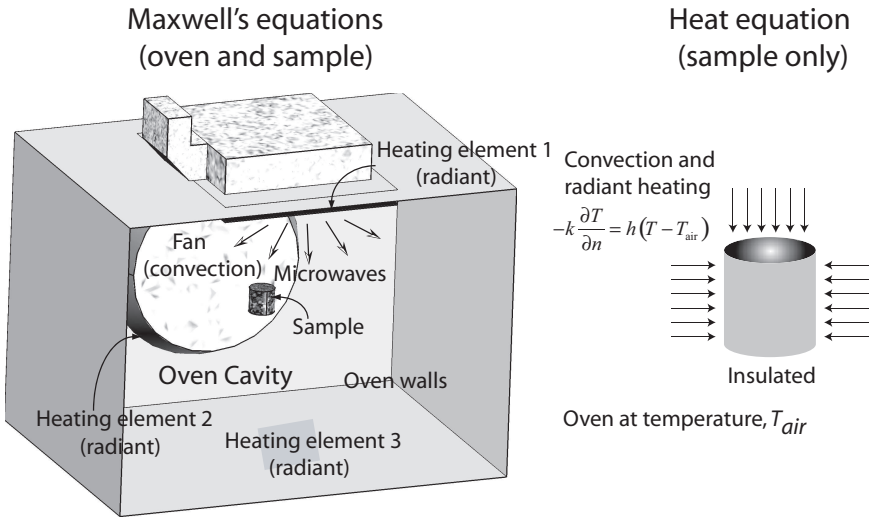

Figure 3.1: a) The computational domain for the electromagnetic simulation (for microwave heating) consists of both the oven and the sample. b) Heat transfer was solved only inside the food as shown. Also shown are the boundary conditions used on the surface of the food sample to simulate convection and radiant heating.

power absorbed (source term in the heat equation) by the sample changes and electromagnetic simulations need to be performed again to determine the updated microwave source term. The governing equations for the two physics were solved using the finite element method in the commercial solver, COMSOL Multiphysics (COMSOL Inc., Burlington, MA). To incorporate the coupling during the solution process, the electromagnetics and heat transfer problems were independently set up in the solver and a code was then written in COMSOL Script to implement the feedback mechanism. The electromagnetics problem was solved using the GMRES iterative solver with the Geometric Multigrid preconditioner. The mesh for the electromagnetic problem consisted of a total of 525873 quadratic tetrahedral elements (with 74005 elements in the sample) based on mesh convergence study as shown in Figure 3.2. It was ensured that the mesh consisted of more than 5 elements per wavelength both in the cavity and the sample. For solving the energy equation, the UMFPACK direct solver was used with the sample discretized into 10980 elements. The coupling parameters consisting of solver selection for the two physics, solution update interval and mapping of the electromagnetic solution to the heat transfer mesh and vice versa were programmed in the code. The simulations were run on a 3 GHz Windows workstation with 16 Gb memory.

3.3.2 Magnetic Resonance Imaging (MRI)

Combination heating modes

Convection and radiant heating modes were combined with microwaves for the study. Different combinations of these heating modes corresponding to different processing conditions were considered. The different processing conditions included combination of different oven temperatures, heat transfer rates and microwave power cycling. These

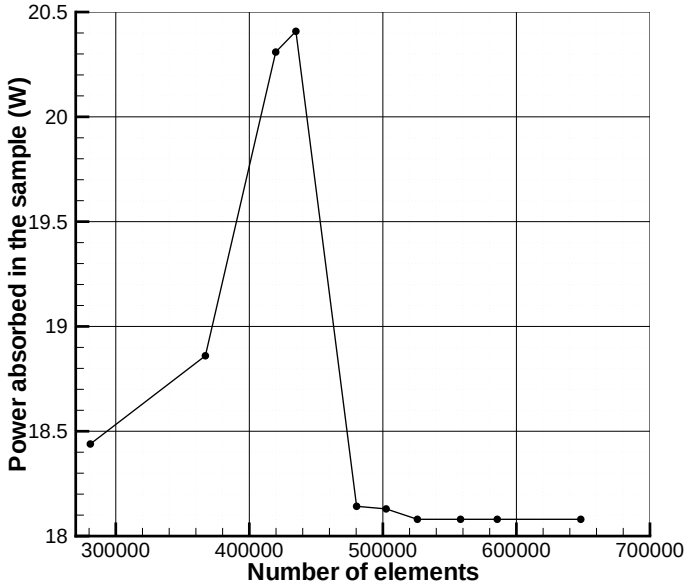

Figure 3.2: Mesh convergence analysis for the electromagnetic modeling. The total number of elements chosen for the final solution was 525873.

are listed in Table 3.2. The combinations were programmed in a GE Profile Trivection oven (Model no. JT930BHBB, General Electric Company, Louisville, KY).

Table 3.2: The different combinations of heating modes and MRI measurements times

Heating combination	**Heating modes used**	**Convection temperature,** °C	**MRI measurement times,** min
I	Convection, Radiant	80	2, 4, 6, 8, 10, 12
II	Convection, Radiant	110	0.5, 1, 1.5, 2
III	Convection, Radiant, Microwave (Cycling: 10 s on, 40 s off)	80	2, 4, 6, 8, 10, 12
IV	Convection, Radiant, Microwave (Cycling: 20 s on, 10 s off)	110	0.5, 1, 1.5, 2

Sample preparation

The food analogue used for the study was prepared by mixing TX151 powder (Oil Center Research International, Lafayette, LA) with water (1:10 parts by weight). When mixed with water the polymer forms a gel that maintains its integrity during heating. The solution was poured into 50 mL beakers and heated to 70°C in a water bath for 55 min to initiate gelation. Samples were cooled to room temperature and allowed to equilibrate at least 24 hours prior to heating.

MRI methodology

The magnetic resonance imaging experiments were performed using a ∼7T superconducting magnet and Biospec console (Bruker Biospin MRI Inc., Billerica, MA) with 300 MHz for ^{1}H-resonance frequency. Gradient echo sequence (Fast Low Angle Shot, FLASH) magnetic resonance imaging protocol was used to generate the temperature maps. The detailed MRI parameters are given in Table 3.3. MRI data was acquired for each sample at room temperature and then after heat treatment. The samples were positioned identically in the magnet for the imaging procedure before and after heat treatment. The MRI data acquisition time was 9 s. Temperature maps for different durations of heating using different combinations were obtained using MRI. The temperature maps represented 10 horizontal slices from the bottom to top of the cylindrical sample. Temperatures at the different locations are calculated using the following expression:

$$\Delta T = \frac{\varphi - \varphi_{ref}}{\alpha \gamma \, (TE) \, B_o} \tag{3.10}$$

where φ is the phase shift, B_o is the magnetic field strength, α is the proportionality constant, TE is the echo time and γ is the magnetogyric ratio of hydrogen nucleus.

MRI measurements were done for four different combinations of heating modes. The different heating modes along with the times at which the MRI measurements were performed are shown in Table 3.2. The heating times were chosen so that there was negligible moisture transport for the heating duration as discussed in the next section. As shown in Table 3.2, heating times for heating combinations I and III were up to 12 min. For heating combinations II and IV heating times were restricted to 2 min as these combination provided higher heating rates and there was rapid temperature rise in the samples.

Table 3.3: MRI parameters for the experiments

Parameter	**Value**
Echo Time (TE)	3.264 ms
Repetition Time (TR)	89.6 ms
Flip angle	20°
Matrix size	128×128
Field of view (FoV)	55 x 55 mm^2
Number of slices	10 (Coronal slice)
Slice thickness	3 mm

Moisture loss measurement

Moisture loss due to the heating process was determined using gravimetric measurement. Each sample was weighed prior to heating at room temperature and immediately following the combination heating process. It was confirmed that moisture transport was negligible.

3.4 Results and Discussions

The mathematical model is validated using experimental data and the results are discussed. Different oven parameters are considered and techniques to optimize and design different food processes using combination heating are discussed.

3.4.1 Validation of mathematical model using MRI results

The temperatures predicted from the mathematical model were compared with those measured using MRI for experimental validation. In order to provide a comprehensive and quantitative validation, average temperatures and spatial temperature distributions were compared. Comparison of average temperatures, although a good method for quantitative validation of the computational model, does not provide insight into the spatial temperature distribution. For heating combinations involving microwaves that heat the sample non-uniformly, comparison of spatial temperature distribution is critical for accurate validation of the numerical model.

Comparison of average temperature rise

Comparison of average temperatures in the sample obtained from computations and MRI for the different heating combinations are shown in Figure 3.3. A good match between computed and experimental temperature histories can be seen for all heating combinations. As expected, for combinations involving additional modes of heating (Combinations III and IV as compared to Combinations I and II, respectively), average temperature rise is greater.

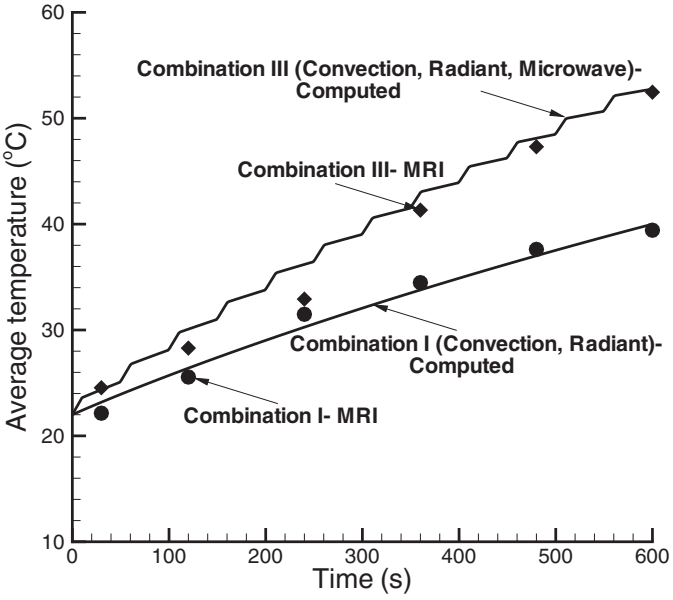

(a)

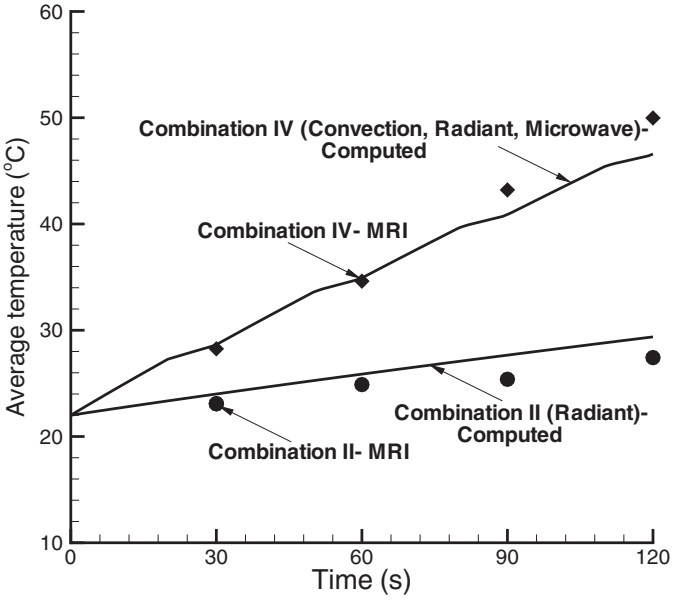

(b)

Figure 3.3: Comparison of average temperatures in the sample obtained from computations and MRI for the various heating combinations shown in Table 3.2 after different time intervals: a) with oven temperature at 80°C, and b) with oven temperature at 110°C. The computations were done at Cornell University and MRI measurements at UC, Davis.

Comparison of spatial temperature distribution

Spatial temperature maps obtained from the model were compared to those measured by MRI at different times for various heating combinations as shown in Figure 3.4. The temperatures were compared at 6 horizontal slices (perpendicular to axis) across the cylindrical sample. As mentioned earlier, 10 slices were obtained from MRI. The six comparison slices were chosen from the center of the gel sample. Slices at the top and bottom of the sample were not used for comparison since these have partial volume effects and slightly non-ideal surfaces. Any changes in sample geometry related to heating will also primarily impact these areas and hence they have been omitted from the detailed spatial comparison.

Figures 3.4-3.7 demonstrate a good match between the simulated and experimental spatial temperature profiles obtained by heating the samples using Combinations I-IV. Samples were manually positioned inside the oven and into a specially constructed sample shuttle for the MRI spectrometer. Sample positioning inside the over is accurate to less than 1×10^{-4} m in the vertical direction and less than 5×10^{-3} m in the horizontal directions. Sample positioning in the MRI spectrometer is accurate to within 1×10^{-4} m in all directions. Positional differences in the oven lead directly to differences in heating related to the spatial variation of the electromagnetic radiation. Positional differences in the MRI spectrometer would result in minor impacts on the temperature calculations. Hence, dissimilarities in the computed and experimental profiles are primarily related to variations in sample placement combined with variations in sample physical properties. Variations in sample physical properties would result from the inclusion of air bubbles and non-uniform solid distributions. The effect of changes in sample position inside the oven cavity on heating is presented in detail in Section 3.4.3.

Two distinct features of heating are observed: surface heating due to convection

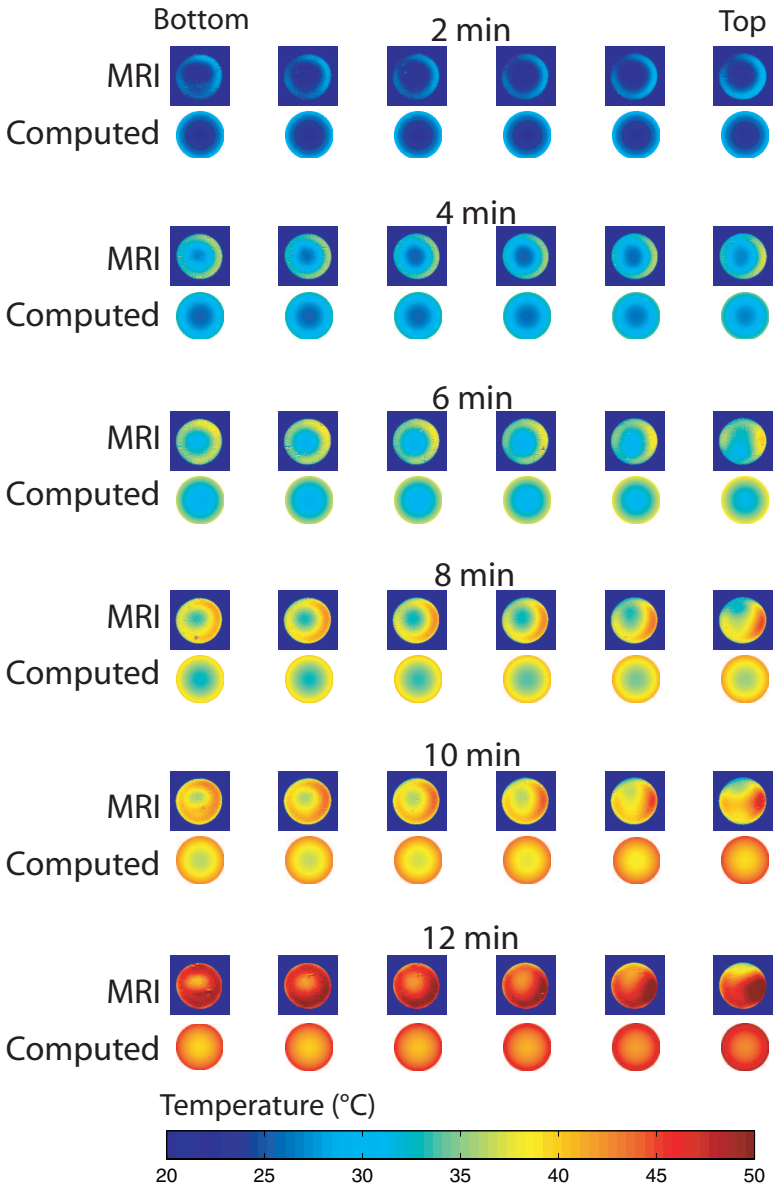

Figure 3.4: Spatial temperature maps obtained from the mathematical model compared to those measured by MRI at six different times for the sample heated by Combination I. The temperatures are compared at 6 different slices across the cylindrical sample starting from the bottom slice on the left to the top slice on the right. The initial temperature of the samples was 22°C.

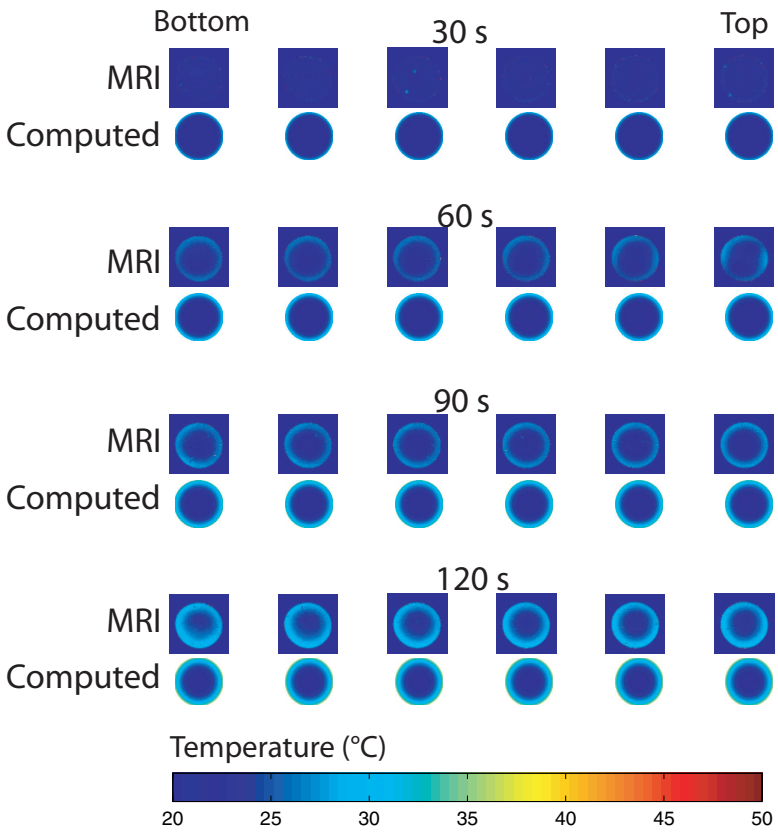

Figure 3.5: Spatial temperature maps obtained from the mathematical model compared to those measured by MRI at four different times for the sample heated by Combination II.

and radiation as can be seen in Figures 3.4 and 3.5 (which do not involve microwave heating) and heating at the interior locations in addition to surface heating as seen in Figures 3.6 and 3.7. These two features of heating nicely complement each other so that for heating combinations that include all the different modes of heating (Combinations II and IV), the entire sample heats more uniformly (Figures 3.6 and 3.7).

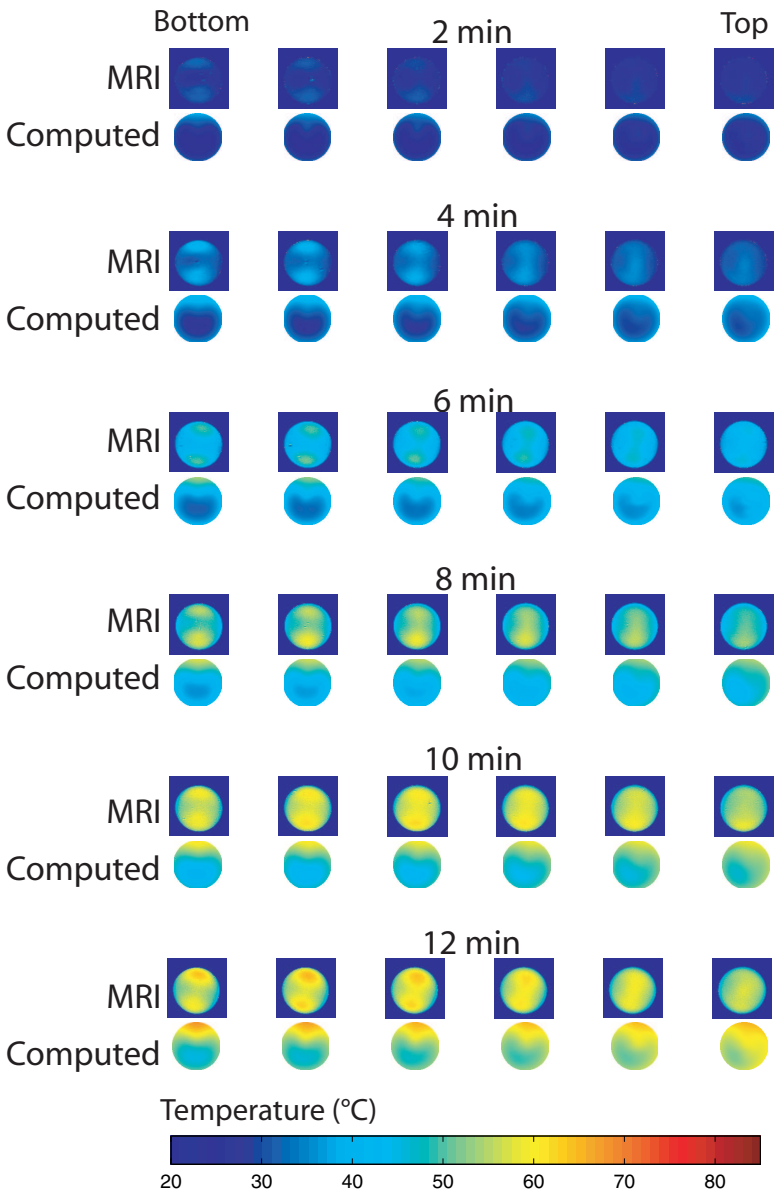

Figure 3.6: Spatial temperature maps obtained from the mathematical model compared to those measured by MRI at six different times for the sample heated by Combination III.

The similarities of the heating patterns between measured and computed are striking for all combinations. Combination I in Figure 3.4 demonstrates symmetric heating with only slightly non-symmetric heating in the gel sample. For combination II heating in Figure 3.5 the MRI and computed spatial temperature maps are nearly identical, detail-

ing the power of the computational model. In combinations III and IV (Figures 3.6 and 3.7) the comparison is best at shorter times and the non-uniform heating induced by the electromagnetic radiation is evident in both the model and experimental data. At the longer heating times (12 minutes and 120 s) for both combination III and IV respectively, preferential heating on one side of the sample is observed in the computation and seen in the experimental measurements. The experimental measurements also demonstrate some spatial differences from the computational model at longer times, however these are primarily related to the difficultly in matching identically the computation to the actual sample placement in the oven. Most importantly the model correctly reflects spatial variations seen in the experimental data as a result of non-uniform microwave fields.

3.4.2 Convection and radiant heating and combination with electromagnetic heating

As discussed in the last section, different heating combinations result in different heating patterns inside the sample. By combining volumetric and surface heating appropriately, one can obtain desired temperature profiles inside the sample and at the same time speed up the heating process. Convection and radiation heating modes heat mostly near surface as shown in Figure 3.8. Change in the oven temperature and movement of the fan (velocity, direction of rotation) changes the heating profiles due to these two modes of heating. Figure 3.8 (top figures) shows the temperature profile along the horizontal centerline of the sample for convective and radiant heating at two different oven temperatures (80°C and 110°C). For an oven temperature of 110°C, the heating is faster as expected. The temperature profiles are symmetric about the center and maximum

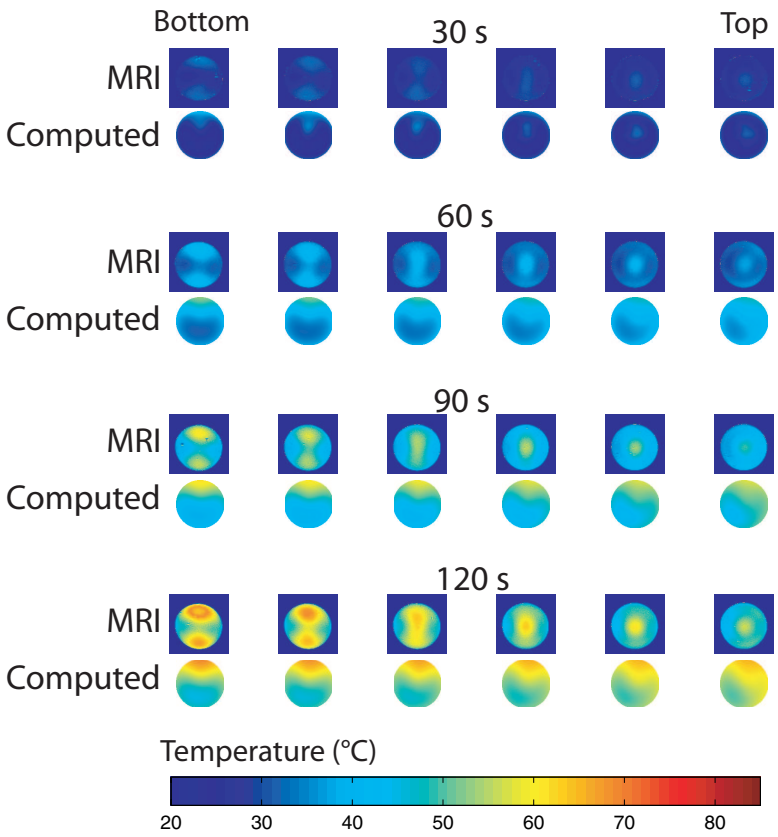

Figure 3.7: Spatial temperature maps obtained from the mathematical model compared to those measured by MRI at four different times for the sample heated by Combination IV.

heating is near the surface. On addition of microwaves (bottom figures), heating in the corresponding combinations are faster and the temperature profiles are no longer symmetric with the right side of the sample heating faster demonstrating the volumetric electromagnetic heating, also seen in Figures 3.6 and 3.7. By estimating the relative temperature rise due to each heating mode, guidelines for combining different modes of heating can be formulated based on the processing needs. Such combinations can be particularly important in speeding up cooking processes where high temperatures are desired at the surfaces of the food so that browning and crust formation occurs and at the same time the interior needs to be heated adequately.

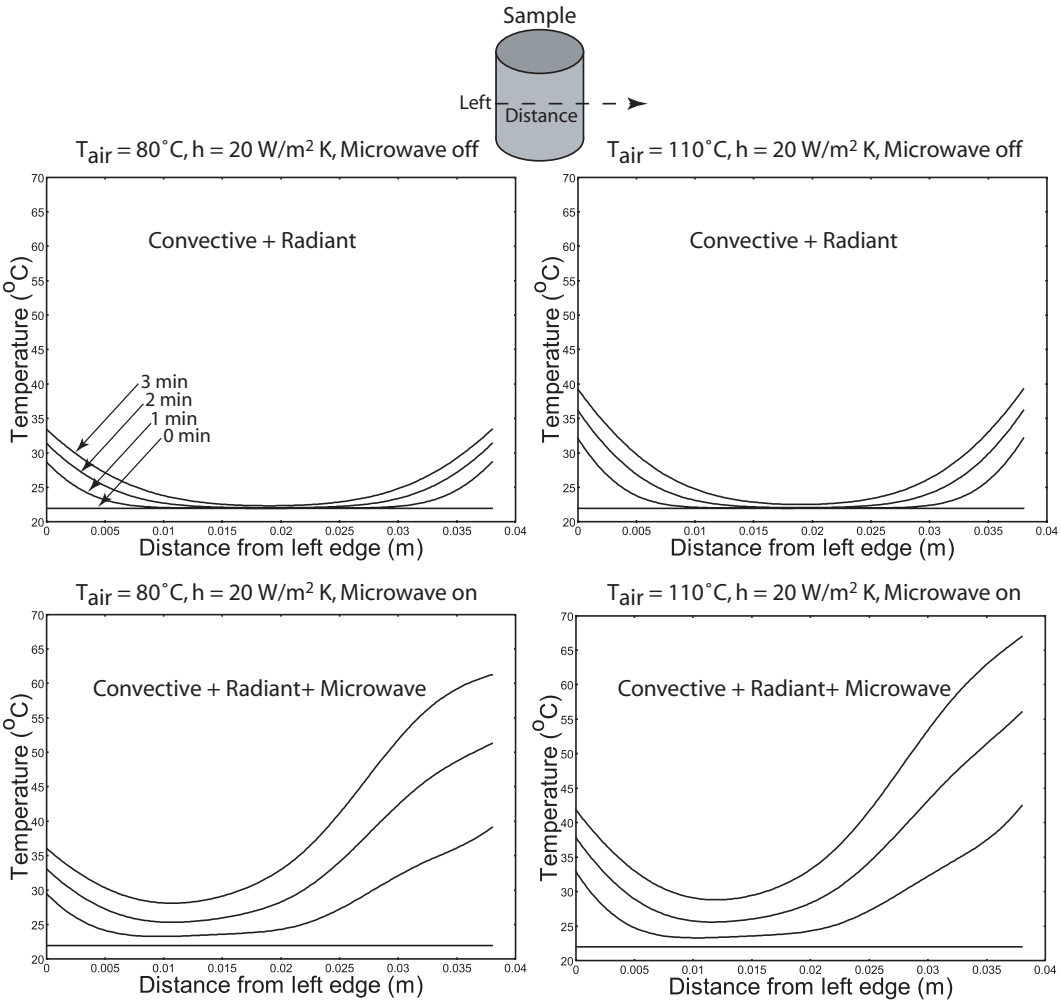

Figure 3.8: Heating profiles along a horizontal line at the center of the sample (as shown in the figure) for different combinations. For each combination, curves are shown for times of 0, 1, 2 and 3 min.

3.4.3 Electromagnetic heating patterns- Effect of positioning of sample inside the oven cavity

The heating profiles due to combination heating are the consequences of volumetric electromagnetic heating and surface heating due to convection and radiation. The electromagnetic heating patterns inside an oven cavity is a function of the electric field, given by Equation 3.7. Figure 3.9a presents the electric field distribution in the oven cavity

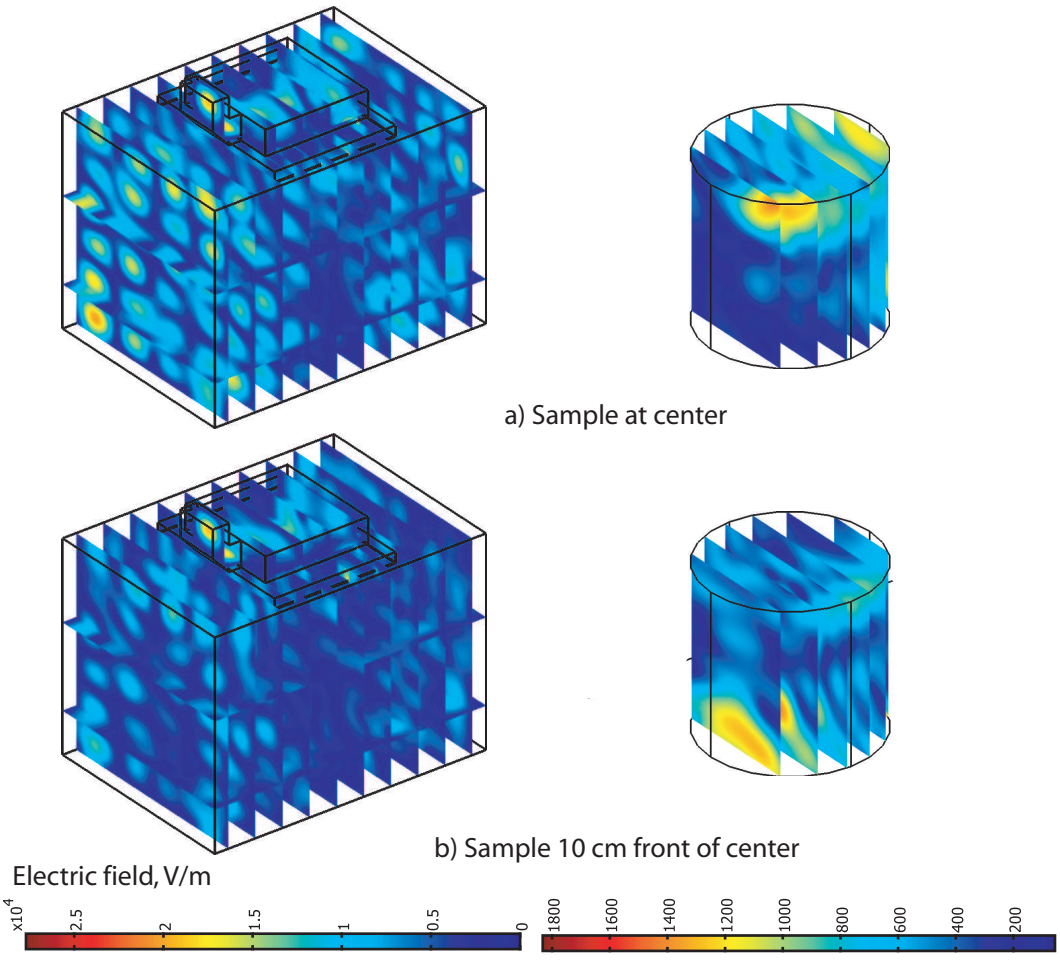

Figure 3.9: Electric field distribution in the oven cavity and sample for different positions of the sample inside the cavity: a) sample placed at the center; b) sample displaced 10 cm horizontally from the center toward the front of the oven. Contour colors from red to blue correspond to regions of high to low electric fields respectively.

with the sample placed at the center. It can be observed that regions of high and low electric fields are obtained inside the oven alternately. This type of electric field patterns in turn leads to hot and cold spots in the sample, also shown in Figure 3.9a. Consequently if the sample is placed in a region of high electric field intensity, the heating rate would be higher. Change in location of the sample changes the pattern of the electric field distribution inside the oven cavity significantly due to change in resonance pattern of the electromagnetic waves. This effect is shown in Figure 3.9b for the sample displaced

horizontally inside the oven by 10 cm toward the front of the center. To demonstrate this effect quantitatively, power absorbed by the sample, placed at seven different locations inside the oven, due to microwave heating are plotted in Figure 3.10. It can be observed that there is significant variation in the power levels for different positioning of the sample inside the oven. It should be noted here that there can be numerous such locations inside the oven cavity and the ideal way to analyze the effect of positioning of the sample in the oven is to perform Monte Carlo simulations, choosing the sample location randomly, and analyzing the change in power absorbed by the sample (using a measure such as coefficient of variation as done in[15] for an unrelated application). However in case of microwave heating, performing Monte Carlo simulations is not feasible since each electromagnetic simulation takes about three hours to complete and therefore the full Monte Carlo analysis would require simulation times that are unrealistic. Analysis shown here with predetermined locations is a feasible approach that provides a reasonable overview of the relative change in power absorbed for the different locations of the sample inside the oven cavity.

3.4.4 Effect of microwave cycling

As discussed earlier, heating patterns in a sample due to electromagnetic heating are fixed for a particular location of the sample inside the oven. Heating rates inside the sample can, however, be controlled by allowing the microwave excitation to cycle. The microwaves can be made to turn off for specific intervals to allow for conductive equilibration of heat to regions that are not heated by electromagnetic heating, thereby leading to a more uniform heating of the sample. However, if a particular temperature rise and uniform heating are desired in the sample, the required cycling is not known a priori. Here the computational model can be set as an optimization problem with an objective

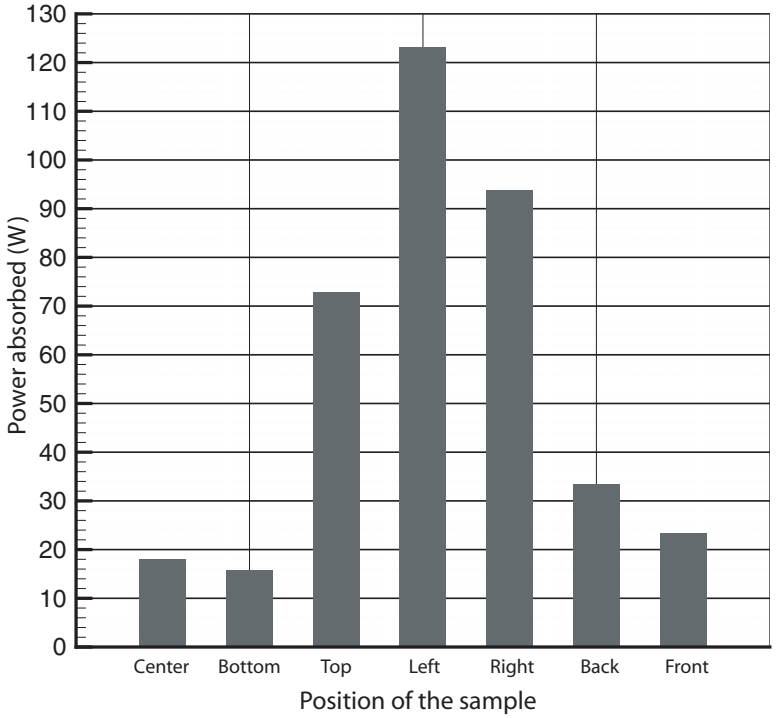

Figure 3.10: Total power absorbed in the food sample as a function of location inside the oven. The sample was placed at the center and displaced by 10 cm in the three different directions as shown.

function to be minimized and be used to test a number of scenarios that include different periods of cycling. We choose this objective function as follows: For a particular temperature, T_p, desired for a particular process, the objective function, J, is:

$$J = \int_V F(T)dv$$
$$F(T) = \begin{cases} T - T_p & T > T_p \\ 0 & T = T_p \\ T_p - T & T < T_p \end{cases} \tag{3.11}$$

By definition, the value of objective function increases as the temperatures are either lower or higher than the processing temperature, T_p. Therefore, by minimizing this objective function, the best method of microwave cycling can be obtained.

A number of microwave cycling cases were considered with the same setting of convection and radiant heating and the average temperature rise in the sample and objective function were calculated and plotted as a function of time for 5 min of heating (Figure 3.11). The processing temperature of 40°C is reached for the five cycles with microwaves on for 20, 30, 40, 50 and 60 s out of a total cycle time of 60 s (Figure 3.11a). Although the average temperature rise provides an estimate of the microwave cycles that can be used, it does not provide any insight if the sample is heated uniformly to the processing temperature, T_p. Figure 3.11b shows that for all cycles, the objective function decreases with time as the sample starts to heat from the initial room temperature (22°C), reaches a minimum or optimum value and then starts increasing as difference in temperatures between the hot and cold locations increases. For the cycle with microwaves on for the entire duration (represented as 60/60), although the average temperature rise to 40°C is faster, the minima in the objective function curve is much higher than the cycle with microwaves on for 20 s out of a 60 s cycle. It can therefore be concluded that the cycle represented as 20/60 is most effective for this process as it not only leads to the final processing temperature but also provides more uniform heating. Similarly, other microwave cycles can be evaluated for different processes using such an optimization technique.

In general, it is not intuitive which combination of heating modes is most efficient considering the time and quality of the final product. The microwave and surface heating patterns change with the different parameters (cycling, location, heat transfer coefficient, etc.). Use of physics based modeling along with optimization techniques is, therefore, very important. This type of analysis can be used to design and optimize combination heating processes and can help reduce the amount of experimentation needed for product or process development.

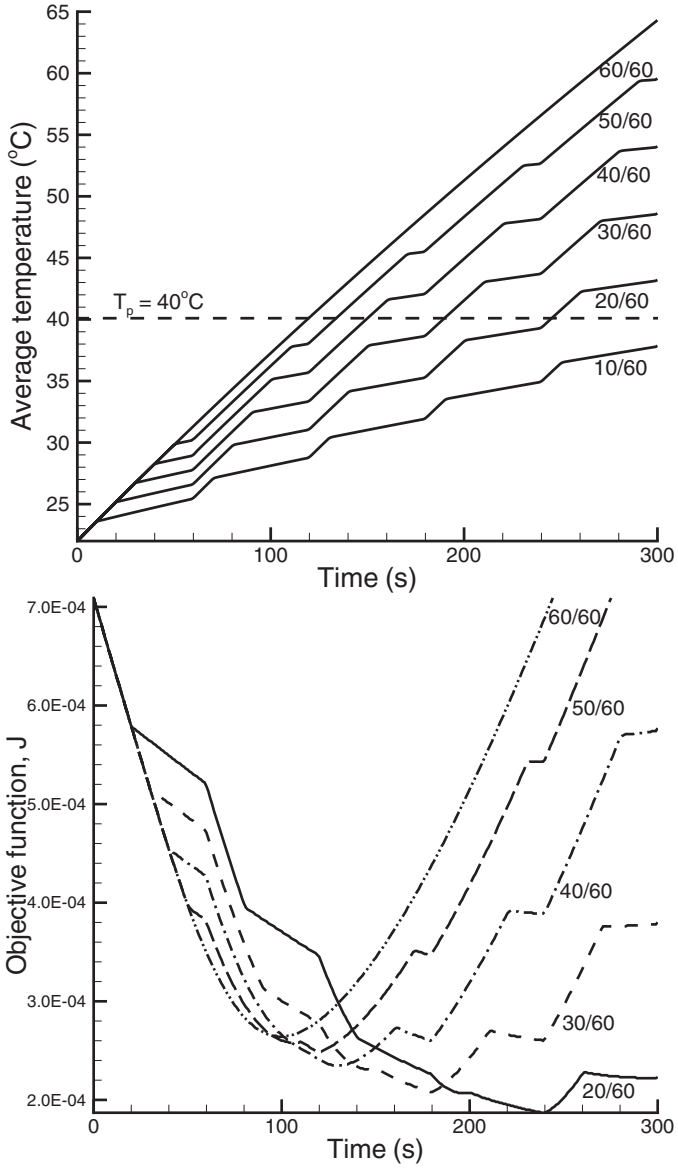

Figure 3.11: Average temperature rise in the sample heated using different cycles of microwave. Also plotted is the objective function (defined in Equation 3.11) as a function of time for the cycles that reach the processing temperature of 40°C. The notation $10/60$ denotes that the microwaves were on for 10 s out of a 60 s cycle.

3.5 Conclusions

A fully coupled electromagnetics- heat transfer model was used in close synergy with novel MRI experimentation for comprehensive validation of the model in space and time and to in turn study the process of combination heating accurately and comprehensively. Coupling of the different physics (electromagnetics, heat transfer) presented inherent computational challenges and was accomplished by manual scripting in the computational software. Some of these difficulties include the use of different finite element meshes for the electromagnetics and heat transfer problems that required mapping of solution back and forth between the different meshes, use of different solvers for the two physics, update of material properties and specification of coupling parameters. 3D validation of the model provided by MRI experiments with proper resolution was critical since the heating modes included volumetric electromagnetic heating.

The different factors that contribute to the heating patterns during combination heating such as heating modes used, placement of sample inside the oven and microwave cycling were considered. The use of objective functions to design and optimize combination heating processes as described in this work can lead to greater control and automation of combination heating processes benefitting the food processors and product developers immensely. Specific guidelines for processing conditions can be developed using the tools discussed in this paper not only for cooking processes but also biomedical applications, wood drying and processing of ceramics that can be optimized using microwave combination heating. As the framework consisting of the model and experimental measurement has been developed, possibilities for working with it are broad and exciting, and it can be used to provide insights into many aspects of combination heating that would not be possible otherwise.

3.6 Acknowledgements

This research was supported by grant number 2003-35503-13737 from the United States Department of Agriculture under the National Research Initiative Grant Program.

BIBLIOGRAPHY

[1] Jumah RY, Raghavan GSV. Analysis of heat and mass transfer during combined microwave-convective spouted-bed drying. *Drying Technology*. 2001;19(3-4):485-506.

[2] McMinn WAM, McLoughlin CM, Magee TRA. Microwave-convective drying characteristics of phannaceutical powders. *Powder Technology*. 2005;153(1):23-33.

[3] Wappling-Raaholt B, Scheerlinck N, Galt S, Banga JR, Alonso A, Balsa-Canto E, Van Impe J, Ohlsson T, Nicolai BM. A combined electromagnetic and heat transfer model for heating of foods in microwave combination ovens. *Journal of Microwave Power and Electromagnetic Energy*. 2002;37(2):97-111.

[4] Ovadia DZ, Walker CE. Impingement in food processing. *Food Technology*. 1998;52(4):46-50.

[5] Geedipalli S, Datta AK, Rakesh V. Heat transfer in a combination microwave-jet impingement oven. *Food and Bioproducts Processing*. 2008;86(C1):53-63.

[6] Datta AK, Ni H. Infrared and hot-air-assisted microwave heating of foods for control of surface moisture. *Journal of Food Engineering*. 2002;51(4):355-364.

[7] Haala J, Wiesbeck W. Modeling microwave and hybrid heating processes including heat radiation effects. *IEEE Transactions on Microwave Theory and Techniques*. 2002;50(5):1346-1354.

[8] Almeida MF. Modeling infrared and combination infrared-microwave heating of foods in an oven, Ph. D. Dissertation, Cornell University. 2005.

[9] Ren G, Chen F. Drying of steamed Asian ginseng (Panax ginseng) roots by microwave-hot air combination. *Pharmazie*. 2000;55(2):124-128.

[10] Ma LH, Paul DL, Pothecary N, Railton C, Bows J, Barratt L, Mullin J, Simons D. Experimental Validation of a Combined Electromagnetic and Thermal FDTD Model

of a Microwave-Heating Process. *IEEE Transactions on Microwave Theory and Techniques*. 1995;43(11):2565-2572.

[11] Zhang H, Datta AK. Coupled electromagnetic and termal modeling of microwave oven heating of foods. *Journal of Microwave Power and Electromagnetic Energy*. 2000;35(2):71-85.

[12] McCarthy MJ. Magnetic Resonance Imaging in Foods. Chapman and Hall, Inc., New York, NY. 1994.

[13] Bows JR, Patrick ML, Nott KP, Hall LD. Three-dimensional MRI mapping of minimum temperatures achieved in microwave and conventional food processing. *International Journal of Food Science and Technology*. 2001;36(3):243-252.

[14] Nott KP, Hall LD. Validation and cross-comparison of MRI temperature mapping against fibre optic thermometry for microwave heating of foods. *International Journal of Food Science and Technology*. 2005;40(7):723-730.

[15] Halder A, Datta AK, Geedipalli SSR. Uncertainty in thermal process calculations due to variability in first-order and weibull kinetic parameters. *Journal of Food Science*. 2007;72(4):E155-E167.

CHAPTER 4

FULLY COUPLED ELECTROMAGNETICS- MULTIPHASE POROUS MEDIA MODEL

4.1 Abstract

The work includes the development of a multiphase porous media model and magnetic resonance imaging (MRI) experiments to study microwave combination heating. Combination of electromagnetic, convective and radiant heating was considered. The material being heated was modeled as a hygroscopic porous medium with different phases: solid matrix, water and gas (water vapor and air), and considered pressure driven flow, binary diffusion and phase change. The 3D transport model was fully coupled with electromagnetics to include the effect of variable properties. MRI was used to obtain spatial temperature and moisture distributions to validate the model. Different combinations and materials were considered to obtain general guidelines for combining heating modes. High and low moisture materials behave differently under combination heating. Low moisture materials can be heated effectively for desired temperature and moisture distribution using higher microwave power which is not possible in high moisture material. Cycling of microwave was found to be useful in distribution of excessive volumetric heat by microwaves and can increase the effectiveness of the combination heating process.

4.2 Introduction and Objectives

Combining microwaves with other heating modes such as convection and radiant heating provides an excellent method to speed up heating processes such as cooking[1],

wood drying[2] and processing of ceramics[3] and pharmaceutical powders[4], to name a few. Combination heating can potentially provide automated custom-heating ability by implementing precise mix of power sources, their levels and time histories to obtain temperature and moisture profiles needed for specific processes. For example, in the cooking process, the quality of the final product such as texture (e.g., sogginess) or flavor (e.g., browning) is a multifaceted attribute that depends on the temperature and moisture distribution and their time-histories. Through improved understanding of the combination heating process, overheating, underheating, overdrying and sogginess of food can be minimized while enhancing its quality. Quality would be more predictable, which would in turn allow increased automation and reduce the drudgery and frustration of food product and process development. This work proposes to study combination heating using a fundamental physics-based computational model of the cooking process integrated with complementary magnetic resonance imaging (MRI) experiments to obtain optimum process guidelines for practical use that would provide the desired product quality in the quickest time, paving way for automation.

4.2.1 Previous mathematical models for studying heat and mass transport during electromagnetic heating

The process of microwave combination heating involves a number of physics and their complex coupling: volumetric electromagnetic heating due to microwaves (solution of Maxwell's equations of electromagnetics), surface heating due to convection and radiant heating, and transport of heat, mass (liquid water, water vapor, air) and momentum inside the sample. Additional complexity arises from the fact that these physics need to be implemented in 3D so that volumetric electromagnetic heating is accurately modeled.

Computational models to study microwave combination heating to date have not considered all these physics, most of those included heat transfer in the sample only and solved for electromagnetics empirically[5] or using Maxwell's equations[6–8]. Some other studies are for 1D or 2D cases valid for heating inside a waveguide[8–11] only; however for the cavity heating problem considered here, the geometry cannot be reduced to 2D. Studies that have considered moisture transport have mostly been empirical models[4] using the effective diffusivity formulation[12,13]. However in case of intensive microwave heating, evaporation and pressure driven flow are significant which these models do not take into account. Only a few studies exist that have considered detailed transport phenomena inside the sample, for example for deep fat frying[14–16] and wood drying[17], and even these are an order of magnitude less complex compared to the present study since they did not involve electromagnetic heating. On the other hand, empirical models have been used for electromagnetic heating when present[18,19]. In this study, we develop a fundamental physics based model that can be applied to generic processes that include electromagnetic heating and heat and mass transfer inside the sample. The model includes the solution of Maxwell's equations of electromagnetics in 3D to obtain the electric field inside the oven cavity and the sample. A 3D multiphase porous media model based on conservation laws is formulated to describe the heat, mass and momentum transfer inside the sample. The electromagnetics and multiphase porous media models are then fully coupled to model the combination heating process. Note that it can also be thought of as a combination drying process and its applicability extends to many heating processes such as drying, baking and thawing used in the food industry and elsewhere.

4.2.2 Modeling of materials with variable properties

Many industrial materials such as metal oxide ceramics and polymers exhibit a phenomena known as thermal runway[20,21] where dielectric properties change rapidly with temperature thereby affecting the heating patterns due to microwave considerably in the sample. In foods, dielectric properties are functions of temperature and moisture. Therefore, the computational model, in addition to accounting for all the different physics, should be fully coupled so that it can go back and forth between different physics (electromagnetics and transport) and update time dependent property values as needed. This is yet another modeling challenge that has not been addressed previously. Prior models that included dielectric property change are for simpler cases which considered heat transfer only[22] or did not solve the Maxwell's equations[23]. In this work, we develop a fully coupled model that includes a property updating scheme so that the model can work effectively for a wide variety of materials including thermal runway materials.

4.2.3 Experimental measurement and validation techniques used previously

It is critical not only to formulate a systematic modeling approach that accounts for all the physics occurring in the sample but to also have a sophisticated experimental technique to validate the computational model. Detailed and accurate measurement of volumetric electromagnetic heating can be obtained from 3D mapping of heating profiles using a technique such as Magnetic Resonance Imaging (MRI)[24]. Although a few studies have looked at detailed measurement and validation techniques using MRI[6,25], most of these have reported temperature distributions only. Others have used techniques such as measurement of surface temperatures using infrared camera[7] or thermosensitive

paper[26] and point temperature measurement using fiber optic temperature probe[27] that do not give a complete picture of the 3D heating process involving volumetric electromagnetic heating. Moisture movement and distribution is critical to the quality of the final product as discussed above; however, quantitative distribution of moisture in 3D has not been reported earlier[28–30]. In this study, we not only include the mapping of temperatures but moisture as well using MRI that again presents inherent challenges. The computational model is comprehensively validated by comparison with the experimental temperature and moisture profiles.

4.2.4 Objectives

The main objectives of this study are to: 1) Formulate and solve a fundamental physics based mathematical model for combination heating processes; 2) Use magnetic resonance imaging (MRI) measurements for fundamental understanding of the process and to validate the computational model; 3) Use the computational model to test *"what-if"* scenarios during combination heating with the aim of design and optimization of the process.

This chapter is organized as follows. First, the mathematical formulation consisting of electromagnetics and multiphase porous media models is presented and the solution strategy is discussed. Subsequently, the experimental methodology that includes the combination oven, test material and MRI details is discussed. The model is then validated using the MRI results and its predictions are used to understand different combination heating processes.

4.3 Mathematical Model

Mathematical description of the combination heating process broadly requires the solution of two different physics- electromagnetics in the oven cavity and sample, and heat, mass and momentum transport in the sample. The Maxwell's equations of electromagnetics are solved to obtain the electric field inside the oven cavity and sample and coupled with a multiphase porous media model to obtain temperature and moisture distribution in 3D inside the samples. These different physics are discussed in details separately in the following sections.

4.3.1 Electromagnetics- Solution of Maxwell's equations in the oven cavity and sample

The Maxwell's equations of electromagnetics for variable dielectric properties are given by:

$$\nabla \times \mathbf{E} = -j\omega\mu_0\mathbf{H} \tag{4.1}$$

$$\nabla \times \mathbf{H} = j\omega\epsilon_0\epsilon\mathbf{E} \tag{4.2}$$

$$\nabla \cdot \epsilon\mathbf{E} = 0 \tag{4.3}$$

$$\nabla \cdot \mathbf{H} = 0 \tag{4.4}$$

where **E** is the electric field intensity and **H** is the magnetic field intensity, both defined as time harmonics:

$$\mathbf{E}(x, y, z, t) = \mathbf{E_0}(x, y, z)\, e^{i\omega t} \tag{4.5}$$

$$\mathbf{H}(x, y, z, t) = \mathbf{H_0}(x, y, z)\, e^{i\omega t} \tag{4.6}$$

The complex relative permittivity, ϵ, of the dielectric material (model food product) is given by:

$$\epsilon = \epsilon' + i\epsilon'' \tag{4.7}$$

where ϵ' is the dielectric constant and ϵ'' is the dielectric loss factor.

Boundary Condition The combination oven walls were perfect electric conductors. Therefore:

$$E_{\text{tangential, oven wall}} = 0 \tag{4.8}$$

Microwave heating term The heat absorbed by the sample per unit time due to the microwaves is given by:

$$Q(x, y, z, t) = \frac{1}{2}\omega\epsilon_o\epsilon''|\mathbf{E}|^2 \tag{4.9}$$

4.3.2 Multiphase porous media model- Transport of momentum, mass and energy in the sample

To describe the heat, mass and momentum transfer in the sample during the combination heating process, a 3D multiphase porous media model was formulated. The sample was considered as a porous material[31] with three phases: solid, liquid water and gas. The gas phase had two components: water vapor and air. The schematic of a representative elementary volume (REV) of the material is shown in Figure 4.1. The volume fraction of pores in a representative elementary volume of the material, ΔV, is denoted by porosity, ϕ:

$$\phi = \frac{\Delta V_p}{\Delta V} = \frac{\Delta V_w + \Delta V_g}{\Delta V} \tag{4.10}$$

where ΔV_w and ΔV_g are the volume occupied by liquid water and gas phases in the REV respectively. The structure of the sample does not change during the combination heating process and hence the porosity remains constant.

The mass conservation equation for the transportable phases includes the effects of bulk flow (convection), diffusion and capillary flow. The porous media model also incorporates the change of phase between liquid water and vapor (evaporation/ condensation) throughout the domain. The energy conservation equation is solved for the mixture and the effect of microwave heating is included as a source term obtained from the electromagnetics model.

Momentum Conservation

Darcy's law is valid for flow in the porous media where velocities are low. The superficial velocity for each moving phase (liquid water and gas) due to the gas pressure gradient in the medium is therefore given by:

$$\mathbf{v_{sup,i}} = -\frac{k_i k_{r,i}}{\mu_i} \nabla P \tag{4.11}$$

where $i = w$ denotes the liquid water phase and $i = g$ the gas phase. The total gas pressure is the sum of the partial pressures of vapor and air based on the ideal gas law, $P = p_a + p_v$. The actual velocity due to the gas pressure for each phase based on the volume occupied by that particular phase is therefore given by:

$$\mathbf{v_i} = -\frac{1}{S_i \phi} \frac{k_i k_{r,i}}{\mu_i} \nabla P \tag{4.12}$$

where S_w and S_g are the liquid water saturation and gas saturation respectively. The saturations, S_i, denote the volume fraction of the liquid or gas phase with respect to

pore volume:

$$S_i = \frac{\Delta V_i}{\Delta V_p} = \frac{\Delta V_i}{\phi \Delta V} \tag{4.13}$$

Liquid water in the pores experience the capillary pressure, p_c, in addition to the gas pressure. Therefore,

$$p_w = P - p_c \tag{4.14}$$

The effective velocity of the liquid phase is therefore given by

$$\begin{aligned} \mathbf{v_{eff,w}} &= -\frac{1}{S_w \phi} \frac{k_w k_{r,w}}{\mu_w} \nabla p_w \\ &= -\frac{1}{S_w \phi} \frac{k_w k_{r,w}}{\mu_w} \nabla P + \frac{1}{S_w \phi} \frac{k_w k_{r,w}}{\mu_w} \nabla p_c \\ &= \mathbf{v_w} + \frac{1}{S_w \phi} \frac{k_w k_{r,w}}{\mu_w} \frac{\partial p_c}{\partial S_w} \nabla S_w \end{aligned} \tag{4.15}$$

Equation 4.15 can be written in terms of capillary diffusivity[32], $D_c = -\frac{k_w k_{r,w}}{\phi \mu_w} \frac{\partial p_c}{\partial S_w}$, and water concentration, $c_w = \rho_w \phi S_w$, in a compact form:

$$\mathbf{v_{eff,w}} = \mathbf{v_w} - \frac{D_c}{c_w} \nabla c_w \tag{4.16}$$

Mass Conservation

The mass conservation equation for the liquid water phase includes the bulk flow and phase change:

$$\begin{aligned} \frac{\partial c_w}{\partial t} + \nabla \cdot (\mathbf{v_{eff,w}} c_w) &= -\dot{I} \\ \frac{\partial c_w}{\partial t} + \nabla \cdot (\mathbf{v_w} c_w) &= \nabla \cdot (D_c \nabla c_w) - \dot{I} \end{aligned} \tag{4.17}$$

The continuity equation for the gas phase is given by:

$$\frac{\partial c_g}{\partial t} + \nabla \cdot \left(\mathbf{v_g} c_g\right) = \dot{I} \tag{4.18}$$

The mass conservation equation for the vapor component of the gas phase includes bulk flow, binary diffusion and phase change:

$$\frac{\partial c_v}{\partial t} + \nabla \cdot \left(\mathbf{v_g} c_v\right) = \nabla \cdot \left(S_g \phi \frac{C^2}{\rho_g} M_a M_v D_{eff,g} \nabla x_v \right) + \dot{I} \tag{4.19}$$

Here vapor concentration is related to the gas concentration by its mass fraction, $c_v = \omega_v c_g$. Similarly, concentration of air, c_a, is $\omega_a c_g$. Knowing the mass fraction of vapor from Equation 4.19, mass fraction of air can be calculated from the expression:

$$\omega_a = 1 - \omega_v \tag{4.20}$$

Energy Conservation

Energy conservation includes convection due to moving phases, conduction, phase change and microwave heat source term calculated from Equation 4.9:

$$\begin{aligned} \left[\sum_{i=s,w,v,a} \left(c_i c_{p,i}\right) \right] \frac{\partial T}{\partial t} \quad &+ \quad c_i \mathbf{v_i} \cdot \nabla \left[\sum_{i=w,v,a} \left(c_{p,i} T\right) \right] - D_c \nabla c_w \cdot \nabla \left(c_{p,w} T\right) \\ &= \quad \nabla \cdot \left(k_{eff} \nabla T\right) - \lambda \dot{I} + Q\left(x, y, z, t\right) \end{aligned} \tag{4.21}$$

Here the effective thermal conductivity is given by the volume weighted average of the different phases and components:

$$k_{eff} = \left(1 - \phi\right) k_s^{th} + \phi \left\{ S_w k_w^{th} + S_g \left(\omega_v k_v^{th} + \omega_a k_a^{th} \right) \right\} \tag{4.22}$$

Phase change (Evaporation/ Condensation)

The formulation for phase change is obtained from the literature[14]:

$$\dot{I} = K \frac{M_v}{RT} \left(p_{v,eq} - p_v\right) \tag{4.23}$$

where $p_{v,eq}$ is the equilibrium vapor pressure which is a function of both temperature and moisture content of the material.

Boundary and Initial Conditions

The boundary conditions needed to solve the set of governing equations are now listed (also shown in Figure 4.1). Pressure was set to ambient at all surfaces of the cylindrical sample:

$$P|_s = P_{amb} \tag{4.24}$$

Water from the interior can move out of the boundary as vapor after evaporation. When the liquid water saturation becomes high ($S_w = 1$), water can also move out of the open surfaces directly by drip flow. Therefore,

$$j_{n,w}|_s = h_m \phi S_w \left(\rho_v - \rho_{v,\,oven}\right) + \underbrace{c_w v_{n,w}}_{\text{when } S_w = 1} \tag{4.25}$$

where $j_{n,w}$ is the total normal flux of water at a particular surface. Vapor can be convected away from the open surfaces. Therefore,

$$j_{n,v}|_s = h_m \phi S_g \left(\rho_v - \rho_{v,\,oven}\right) \tag{4.26}$$

Convection and radiant heating act only on the surface and are, therefore, included as boundary conditions while solving the energy conservation equation. The loss of heat due to evaporation of water, removal of liquid water (during drip flow) and vapor is also included in the boundary condition for heat transfer:

$$\begin{aligned} q_n|_s &= h(T - T_{oven}) - h_m \phi S_w \left(\rho_v - \rho_{v,\,oven}\right) \lambda \\ &- h_m \phi \left(S_w + S_g\right) \left(\rho_v - \rho_{v,\,oven}\right) c_{p,v} T - \underbrace{c_w v_{n,w} c_{p,w} T}_{\text{when } S_w = 1} \end{aligned} \tag{4.27}$$

where q_n is normal heat flux.

Initial Conditions The initial conditions for the different variables are listed in the input parameters table (Table 4.1).

4.3.3 Input Parameters

All input parameters used for the simulations are listed in Table 4.1. The heating modes considered are detailed in Table 4.2.

4.3.4 Numerical Solution

The schematic of the computational domain along with the different physics solved for in the subdomains are shown in Figure 4.1. The governing equations for electromagnetics and porous media model need to be fully coupled. As temperature and moisture distribution in the material changes with heating time, the dielectric properties change as given in Table 4.1. This in turn changes the electric field distribution inside the oven and sample and as a result, the microwave power absorbed (source term in the heat equation) by the sample changes and electromagnetic simulations have to be repeated to determine the updated microwave source term. Additionally, different finite element meshes for the electromagnetics and heat transfer problems are needed that requires mapping of solution back and forth between the different meshes, different solvers for the two physics and specification of coupling parameters also needs to be included. To incorporate this coupling, the electromagnetics and porous media problems were independently setup in COMSOL Multiphysics (COMSOL Inc., Burlington, MA) graphical user interface (GUI). A code was then written in scripting version of the software, COMSOL Script, to implement the feedback mechanism. The electromagnetics problem was solved us-

Table 4.1: Input parameters for the simulations

Parameter	Value	Source
Oven dimensions (m)	$0.61 \times 0.44 \times 0.44$	
Sample (cylindrical) dimensions (m)	0.018 (rad) $\times$ 0.035	
Electromagnetics		
Microwave frequency (GHz)	2.45	
Dielectric constant, ϵ'	$27.403 + 9.5387M - 0.6018M^2$	
Dielectric loss, ϵ''	$23.756 - 4.8009M + 0.3613M^2$	
Transport		
Porosity, ϕ	0.88	[15]
Viscosity		
Water, μ_w (Pa s)	0.988×10^{-3}	
Vapor and air, μ_g (Pa s)	1.8×10^{-5}	
Intrinsic permeability		
Water, k_w (m^2)	5×10^{-14}	[15]
Vapor and air, k_g (m^2)	10×10^{-14}	[15]
Relative permeability		
Water, $k_{r,w}$	$[(S_w - 0.09)/0.91]^3, \quad S_w > 0.09$ $0, \quad S_w < 0.09$	[31]
Vapor and air, $k_{r,g}$	$1 - 1.1S_w, \quad S_w < 1/1.1$ $0, \quad S_w > 1/1.1$	[31]
Capillary diffusivity (water), D_c (m^2/s)	$10^{-8} \exp(-2.8 + 2\mathrm{M})$	[15]
Binary diffusivity, $D_{eff,g}$ (m^2/s)	2.6×10^{-6}	
Specific heat capacity		
Solid, c_{ps} (J/kg K)	1650	[34]
Water, c_{pw} (J/kg K)	4178	[34]
Vapor, c_{pv} (J/kg K)	2062	[34]
Air, c_{pa} (J/kg K)	1006	[34]
Thermal conductivity		
Solid, k_s^{th} (W/m K)	0.21	[34]
Water, k_w^{th} (W/m K)	0.57	[34]
Vapor, k_v^{th} (W/m K)	0.026	[34]
Air, k_a^{th} (W/m K)	0.026	[34]
Density		
Solid, ρ_s (kg/m^3)	1430	
Water, ρ_w (kg/m^3)	998	
Vapor, ρ_v (kg/m^3)	Ideal gas law	
Air, ρ_a (kg/m^3)	Ideal gas law	
Latent heat of vaporization, λ (J/kg)	2.26×10^6	
Evaporation rate constant, K (/s)	1×10^{-3}	[35]
Equilibrium vapor pressure, $p_{v,eq}$ (Pa)	$p_{sat}(T) \exp(-0.0267M^{-1.656}$ $+0.0107e^{-1.287M} M^{1.513} \ln[p_{sat}(T)])$	
Ambient pressure, P_{amb} (Pa)	101325	
Mass transfer coefficient, h_m (m/s)	6×10^{-3}	
Heat transfer coefficient, h (W/m^2 K)		
Top	80	
Side	20	
Oven temperature, T_{oven} (°C)	80	
Initial Conditions		
Pressure, P_0 (Pa)	101325	
Water concentration, $c_{w,0}$ (kg/m^3)	789.4	
Vapor mass fraction, $\omega_{v,0}$	0.01	
Temperature, T_0 (°C)	22	

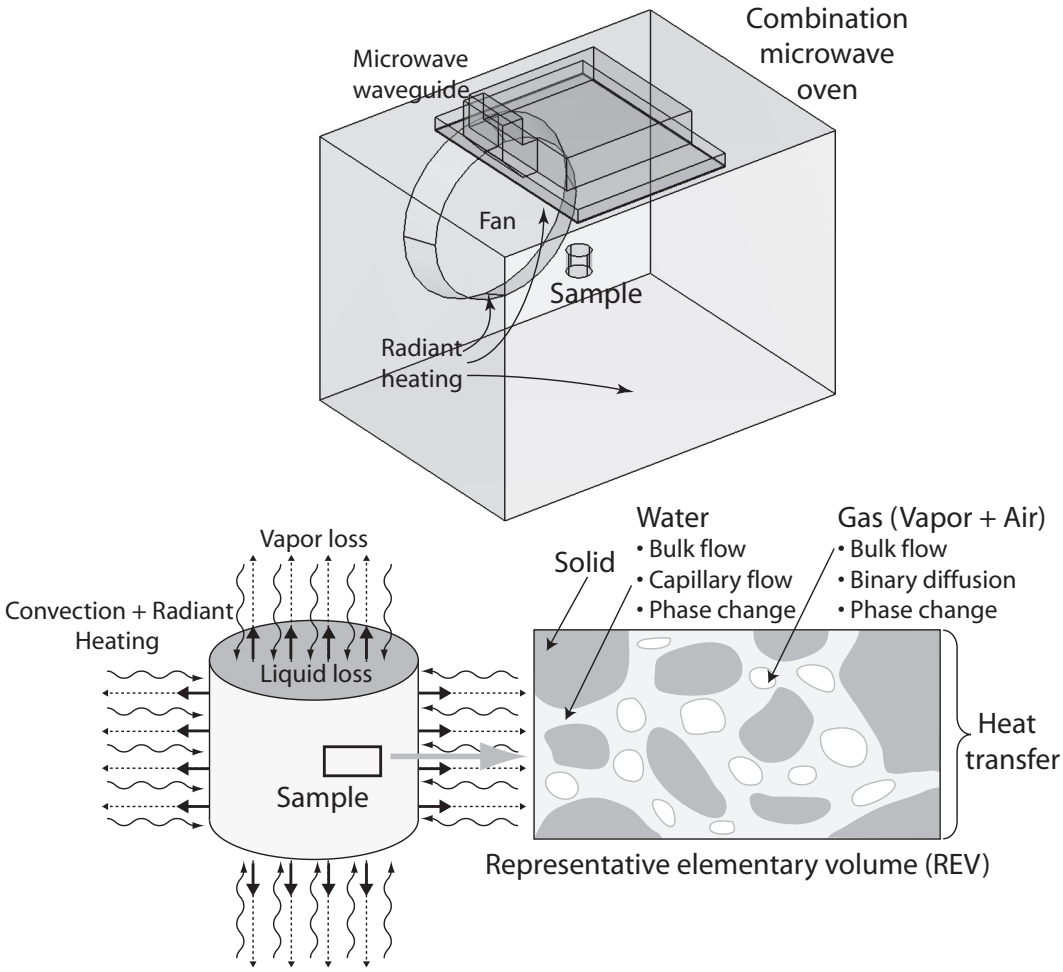

Figure 4.1: a) The computational domain for the electromagnetic simulation (for microwave heating) consists of both the oven and the sample. b) Porous media model was solved only inside the sample as shown. Also shown are the boundary conditions on the surface of the sample.

ing the GMRES iterative solver with the Geometric Multigrid preconditioner. The mesh consisted of a total of 367082 tetrahedral elements based on mesh convergence study. For solving the energy equation, the UMFPACK direct solver was used with the sample discretized into 44865 elements. The solver selection for the two physics, solution updating interval and mapping of the electromagnetic solution to the heat transfer mesh and vice versa were programmed in the code. The simulations were run on a 3 GHz Windows workstation with 16 Gb memory.

Table 4.2: Different combination of heating modes considered.

Heating modes	**Air temperature,** °C	**MRI measurement,** min
Convection, Radiant	80	10, 15, 20, 30
Cycled Microwaves (Cycling: 10 s ON, 40 s OFF), Convection, Radiant	80	10, 15, 20, 30
Full Microwaves, Convection, Radiant	80	—

4.4 Experimental Methodology

Heating was performed in a GE Combination Oven (Model No. JT930BHBB, General Electric Company, Louisville, Kentucky) located at the UC Davis NMR Facility. It was equipped for convection-radiant and combined convection-radiant and microwave heating modes. Two different settings of the oven representing different heating combinations were selected for the experiments, one without microwaves and the other with microwaves. The oven temperature for the convection-radiant heating combination was set at 80°C. For the microwave assisted heating combination, the oven temperature was also set at 80°C and microwave heating was on for 10 s for a 50 s cycle. For each of the two heating combinations, samples were heated for 10, 15, 20, and 30 min. Two replicates were performed for each heating combination. Samples were heated one at a time at the center of the oven by placing them on a 5 cm diameter polysulfone disc in a petri dish to minimize direct heating from the oven rack. After combination heating of the sample, it was transferred to a 50 mL pyrex beaker that fit into the sample holder for the imaging spectrometer.

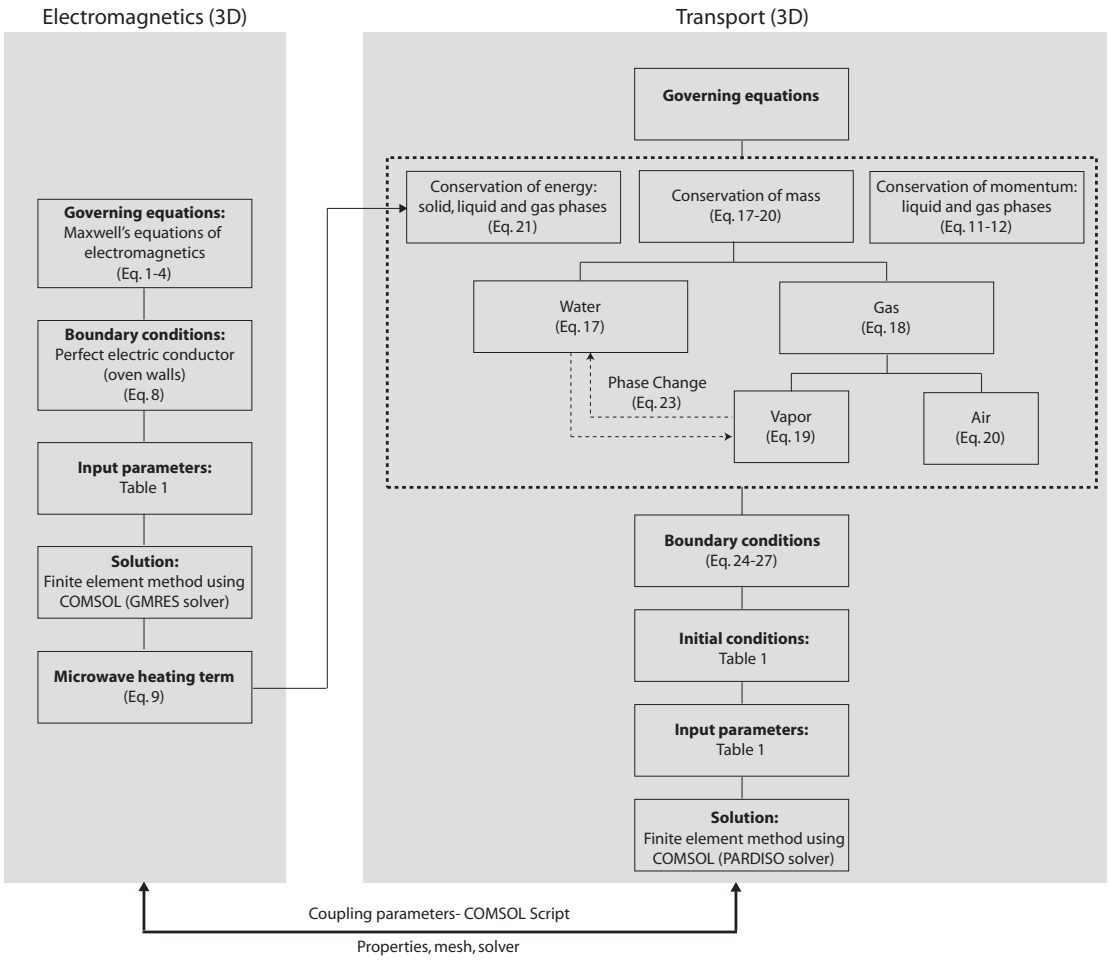

Figure 4.2: Flow chart showing the sequence of steps followed to develop the computational model.

4.4.1 Test Material

The model product was rehydrated Wegmans Instant Mashed Potatoes (Wegmans Food Markets, Inc., Rochester, New York). For each batch, 125 g of potato flakes (moisture content of 0.068 wb) was mixed with 550 g hot (95-100°C) distilled water. The potato flakes and water were mixed thoroughly and the mixture was allowed to equilibrate for 14 h in a 20°C incubator in order to obtain a uniform consistency for MRI imaging. Samples were prepared by placing the mixture in mesh cylinder container with 3.66 cm internal diameter and 3.5 cm height. The mesh cylinders material was

PTFE (polytetrafluoroethylene) (ET8500, Industrial Netting, Minneapolis, Minnesota) that was suitable for high temperature applications and minimum interference with the microwaves. Sample heating and magnetic resonance imaging commenced within an hour of sample preparation.

4.4.2 Magnetic Resonance Imaging (MRI) Measurements

MR imaging experiments were performed using a 7T super-conducting magnet and Biospec console (Bruker Biospin MRI Inc., Billerica, MA) with 300 MHz for 1H-resonance frequency. Three NMR protocols were used: gradient echo sequence (Fast Low Angle Shot, FLASH), Multi-slice multi-echo sequence (MSME), and Carr Purcell Meiboom Gill sequence (CPMG). The NMR parameters are given in Table 4.3. The FLASH sequence was used to generate temperature maps; the MSME was used to generate spin-lattice relaxation time (T2) maps and M0 maps. CPMG verified the mono-exponential decay of the relaxation time (T2).

For each sample the sequence of NMR data acquisition was FLASH, MSME, CPMG for the sample at room temperature sample and then FLASH, MSME, CPMG for the same sample after heat treatment. Data was acquired over a time frame of 4.5 min for the sequence (FLASH, MSME, CPMG). The samples were positioned identically in the magnet for the imaging procedure before and after heat treatment. Temperatures at different locations were calculated by measuring the phase shift using MRI and then using the following expression:

$$\Delta T = \frac{\varphi - \varphi_{ref}}{\alpha \gamma \left(TE\right) B_o} \tag{4.28}$$

where φ is the phase value after heating, φ_{ref} is the phase value before heating, B_o is the magnetic field strength, α is the proportionality constant, TE is the echo time and

Table 4.3: MRI parameters for the experiments

MRI Parameters	**MSME**	**FLASH**
TE	8.527 ms	3.264 ms
# of TEs	16	NA
Flip angle	NA	20 deg
TR	10000 ms	89.6 ms
Matrix size	128×128	128×128
FOV	64×64 mm^2	64×64 mm^2
No. of slices	12 (Coronal orientation)	12 (Coronal orientation)
Slice thickness	3.5 mm	3.5 mm

γ is the magnetogyric ratio of hydrogen nucleus. The M0 values obtained from MRI were correlated to moisture content measured using gravimetric analysis (described in the next section). The temperature and moisture maps represented 12 horizontal slices from the bottom to top of the cylindrical sample.

4.4.3 Gravimetric measurement of moisture loss

Moisture loss due to the heating process was determined using gravimetric measurement. Each sample was weighed prior to heating at room temperature and immediately following the combination heating process.

4.4.4 Input Parameter Measurements

Dielectric properties and heat transfer coefficients for modeling the convection-radiant heating were measured experimentally. Other input parameters for the sample were obtained from literature and are shown in Table 4.1.

Dielectric properties. The dielectric properties (dielectric constant and loss) of the samples were measured as a function of moisture content at the microwave frequency of 2.45 GHz using HP85070 open ended coaxial high temperature probe (Agilent Technologies, Inc.) and a network analyzer (Agilent 8722ES).

Heat transfer coefficients. Point temperature and heat flux histories were measured by thermocouples and heat flux sensors (HFS-3, Omega, Inc.) connected to FLUKE data acquisition Bucket (Fluke Co.). The heat transfer coefficients for different heating modes were calculated using the values of heat flux, surface temperature, and ambient oven temperature.

4.5 Results and Discussions

Experimental validation of the mathematical model is presented for two different combinations of heating, followed by descriptions of temperature, moisture and pressure distributions in the sample for various heating combinations and initial moisture content of the sample. To comprehensively understand the process of combining the different modes of heating for different materials, the variables that affect the final product such as temperature, moisture content and pressure in the domain obtained from computations are analyzed in detail for different conditions. Three different heating combinations were considered, as listed in Table 4.2: convection + radiant heating; cycled microwave + convection + radiant heating; and full microwave + convection + radiant heating. Samples at two different initial moisture contents of 82.1% wb (4.6 db) and 69.7 % wb (2.3 db) were heated using these different combinations and the comparisons are presented.

4.5.1 Experimental validation of temperature and moisture

Experimental validation is critical considering the complexity of the computational model. Validation was done by comparing the temperature and moisture content predicted by the model with the corresponding experimental values obtained from MRI measurements for the different heating combinations, as shown in Figures 4.3-4.6. These comparisons were done for two heating scenarios- the first included convection and radiant heating only and the other heating combination comprised of microwave (cycled), convection and radiant heating. Details of heating combinations are shown in Table 4.2.

Convection + radiant heating The top subplot (i.e., Figure 4.3a in Figure 4.3) compares the computed and measured average temperature or moisture history for the full sample during the combination heating process. The other four subplots (Figures 4.3b–4.3e) present average temperature and moisture histories at four different section. All computed values were obtained using volume averaging. For convection and radiant heating (Figure 4.3), both experiments and computations show that greater heating is from the top of the sample which is exposed to the hot air. Moisture, on the other hand, is lost uniformly from the sample, as shown in Figure 4.4. This is attributed to very high initial moisture content ($\sim$82% w.b.) and therefore, moisture loss depends entirely on the external resistance (as determined by the mass transfer coefficient). However, this is true only for this particular case where the initial moisture content is high and not in the low moisture case discussed later in the paper in detail.

Cycled microwave + convection + radiant heating In case of microwave combination heating (Figure 4.5) experimental measurement as well as numerical prediction

shows that there is more uniform heating of the sample with even the bottom slices being heated by the penetrating microwaves and the temperatures at the corresponding slices compared to convection and radiant heating (Figures 4.3b–4.3e) are higher as expected. The cycling of the microwaves can also be observed from the wavy nature of the computed temperature history plots. Moisture histories (Figures 4.6b–4.6e) are similar for different slices, like for convection + radiant heating (Figures 4.4b–4.4e). However, the amount of moisture loss is more compared to convection + radiant heating, due to greater heating.

For a visualization of spatial variation of temperature in the samples, temperature maps at different slices obtained from computations and MRI after 10 min of heating are plotted in Figure 4.7. The computational model predicts the spatial temperature variations for the two different combinations as obtained experimentally from MRI accurately. Moisture maps are not shown as there is insignificant variation in the spatial distribution at any particular time as was discussed for Figures 4.4 and 4.6.

4.5.2 Temperature distributions for different heating combinations

Average temperature history for high vs. low initial moisture contents for different combination heating scenarios are shown in Figure 4.8. As expected, for a particular moisture content, heating rate increases as amount of microwave heating is increased. The temperatures are generally higher in the low initial moisture material for all heating combinations. Since the temperatures are higher for even the heating combination that does not include microwaves, higher temperature values observed in the initially drier product can be attributed to its lower specific heat capacity, 3410 J/kg K compared to 3726 J/kg K initially. The microwave deposition is comparable in magnitude, 4.21

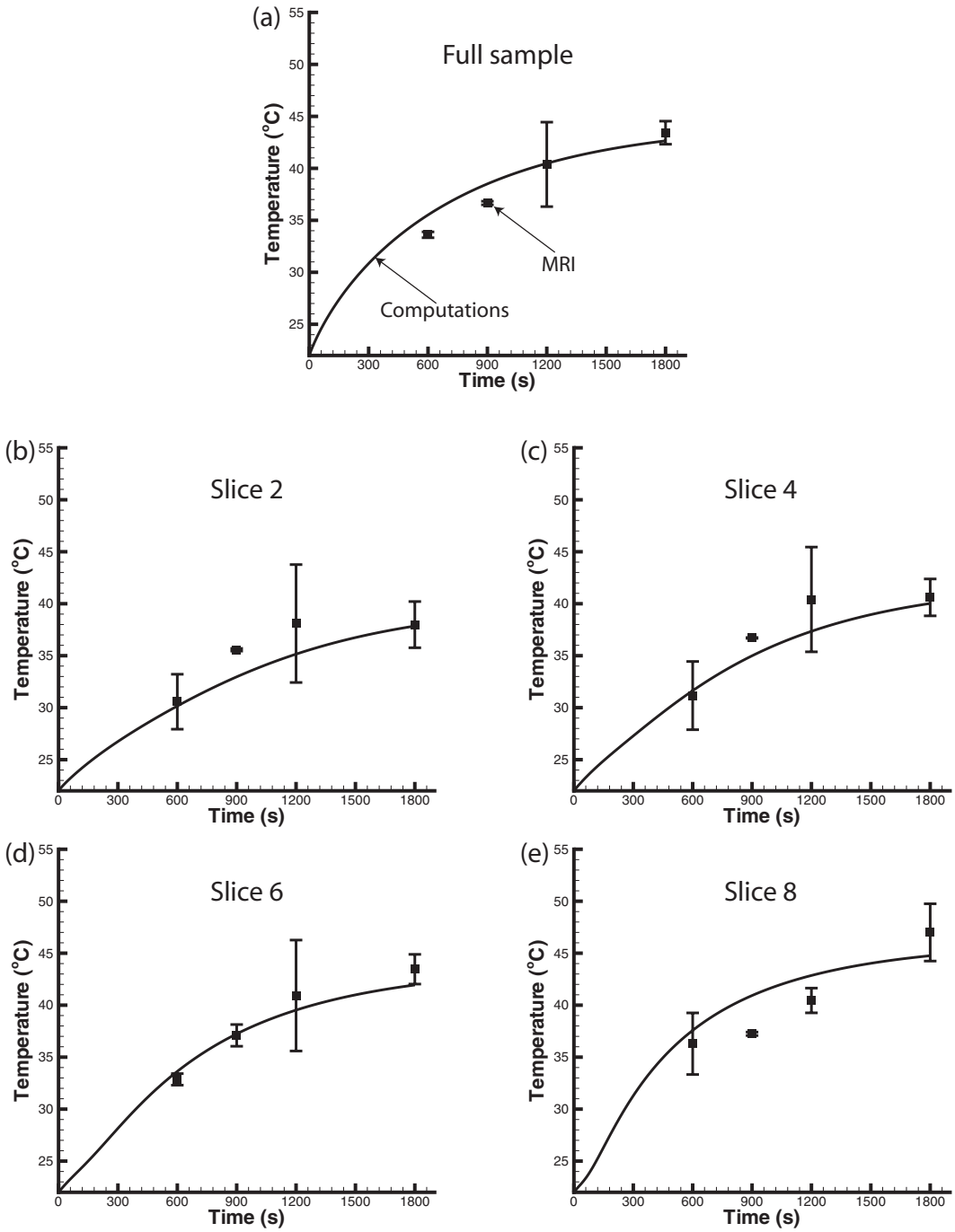

Figure 4.3: Comparison of average temperatures at different times obtained from computations and MRI experiments for the heating combination that involved convection and radiant heating only (no microwaves). The topmost plot shows the average temperature comparison for the full sample and the other plots show the comparison at 4 different slices from the bottom to the top of the cylindrical sample.

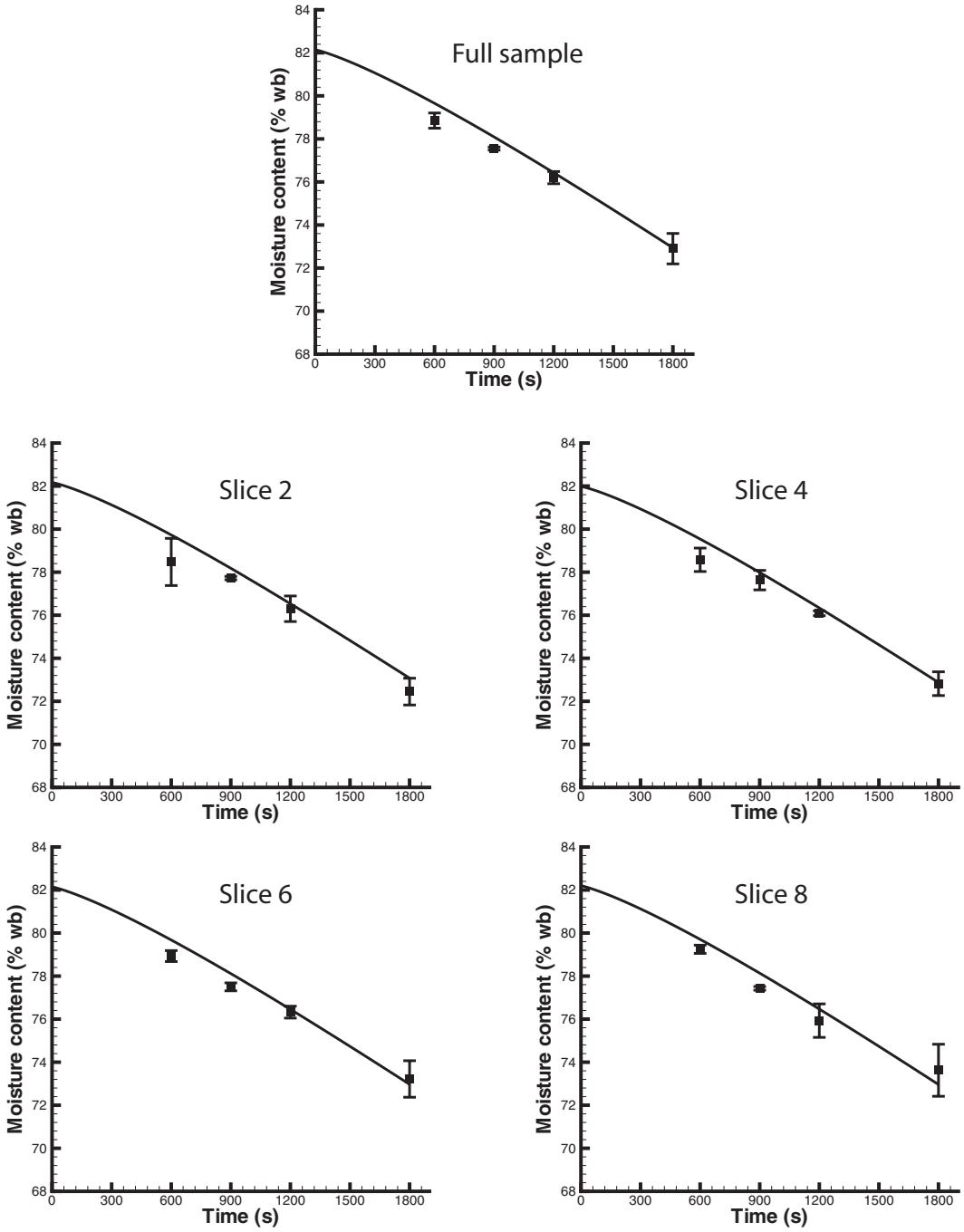

Figure 4.4: Comparison of average moisture content at different times obtained from computations and MRI experiments for the heating combination that involved convection and radiant heating only (no microwaves). The topmost plot shows the average moisture content comparison for the full sample and the other plots show the comparison at 4 different slices from the bottom to the top of the cylindrical sample.

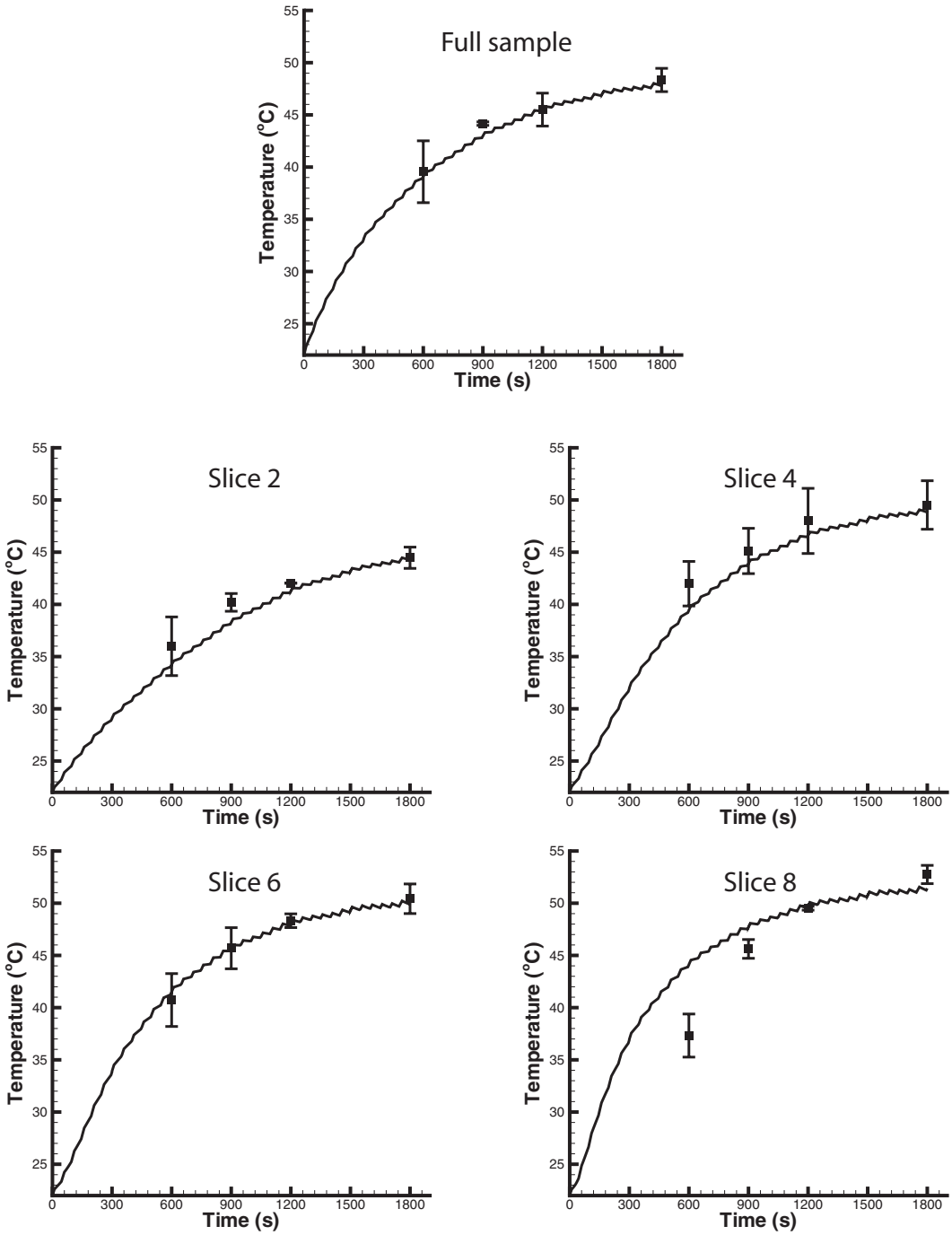

Figure 4.5: Comparison of average temperatures at different times obtained from computations and MRI experiments for the heating combination that involved convection, radiant heating and microwaves. The topmost plot shows the average temperature comparison for the full sample and the other plots show the comparison at 4 different slices from the bottom to the top of the cylindrical sample.

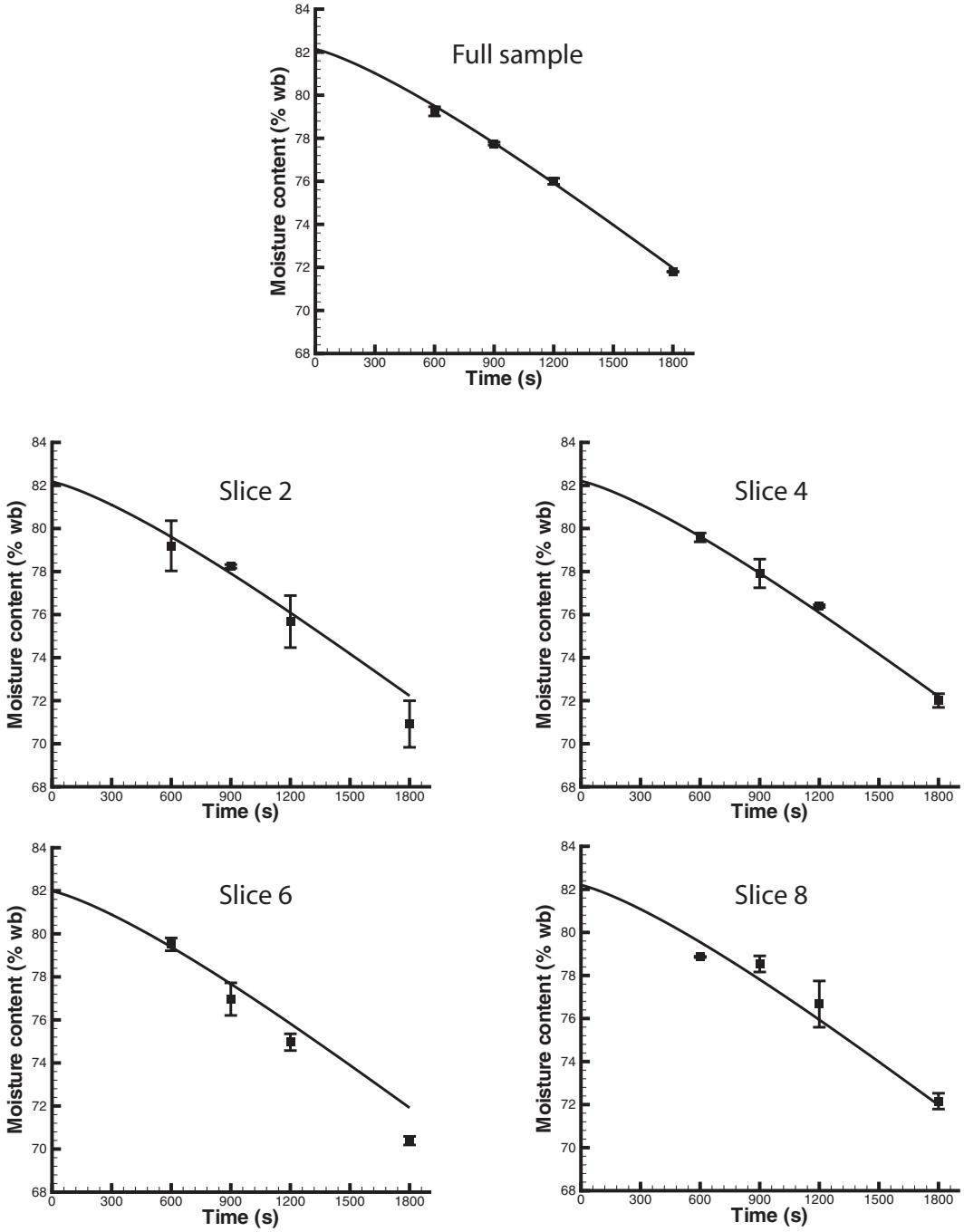

Figure 4.6: Comparison of average moisture content at different times obtained from computations and MRI experiments for the heating combination that involved convection, radiant heating and microwaves. The topmost plot shows the average moisture content comparison for the full sample and the other plots show the comparison at 4 different slices from the bottom to the top of the cylindrical sample.

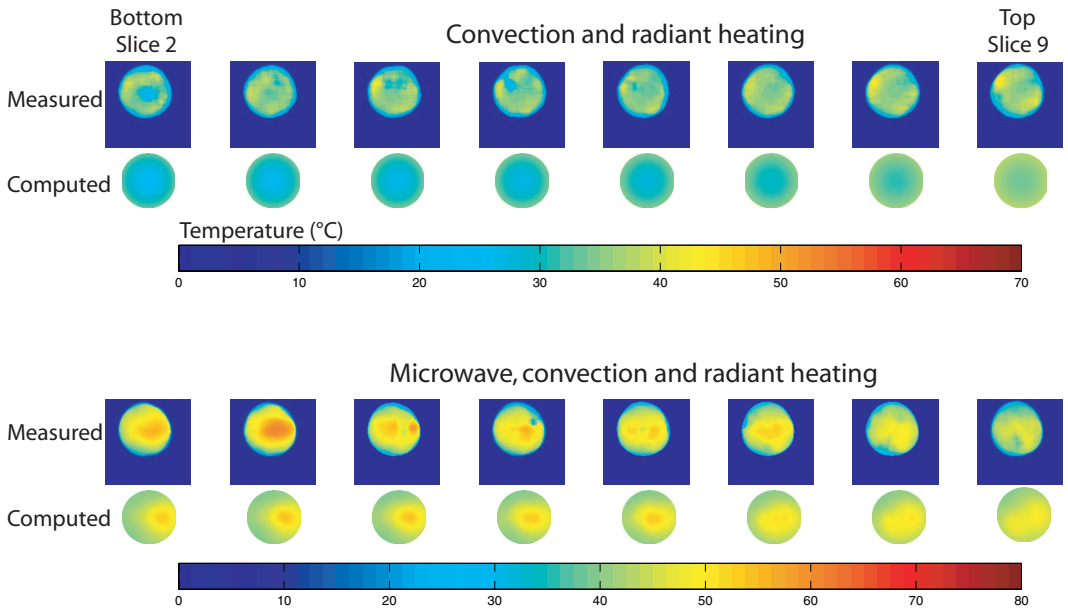

Figure 4.7: Temperature maps comparing the measured (using MRI) and computed values at different slices in the samples after 10 min of heating.

W compared to 4.68 W at t = 20 min, since the electric field patterns do not change significantly as the dielectric properties change.

High initial moisture content The comparison between the spatial temperature values obtained in the material heated using different combinations for a high initial moisture material is shown in Figure 4.9. For convection and radiant heating, temperatures are high at the top surface since it is open. The sample also heats up from the sides but at a much lower rate (thermal resistance due to the mesh cylinder walls). When the microwaves are on for the full time, there is considerable rise in temperatures in the interior locations due to the focusing effect of the microwaves and the heating due to convection and radiation on the surface cannot catch up. On the other hand when cycled microwaves are added, although heating also takes place at the interior locations, the time available for conduction of heat when the microwaves are off leads to more uniform distribution of temperatures. As a result, there is no uncontrollable rise in temperatures

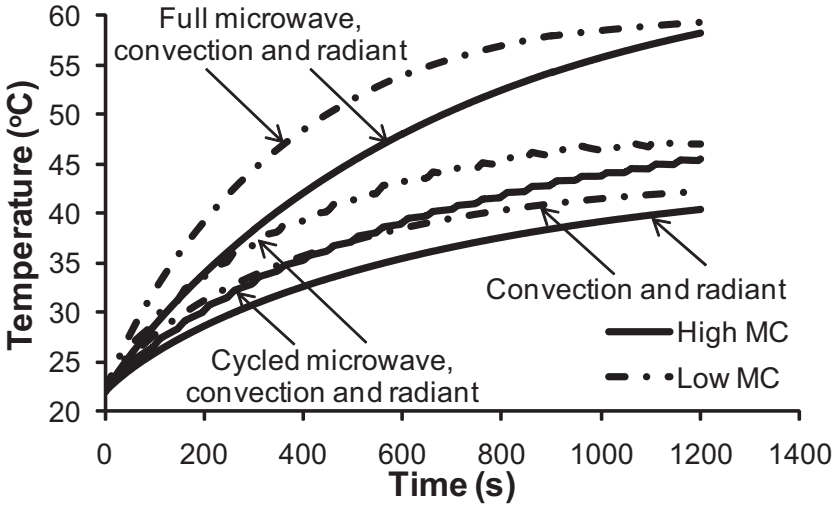

Figure 4.8: Computed average temperature history for material with different initial moisture contents heated using three different combinations.

in the interior and the sample is more uniformly heated. Thus cycling of microwaves can be used very effectively to complement convection and radiant heating in order to provide uniform heating to products during combination heating and at the same time for speeding up the heating process. The ratio of convection and radiant heating power to the microwave power absorbed by the sample is 5.8:1 for cycled and 1.2:1 for full microwaves. The convection and radiant heating power is calculated by integrating the surface heat flux over the sample surface. The microwave power absorbed is calculated using Equation 4.9.

Low initial moisture content Figure 4.10 shows temperature distributions for the low initial moisture sample. Again in this case, microwaves become the dominant mode of heating when on for the full time and the surface does not get heated up as much. Cycled microwaves complements convection and radiant heating well for more uniform heating. The ratio of convection and radiant heating power to the microwave power absorbed by the sample is 4.6:1 for cycled and 0.7:1 for full microwaves.

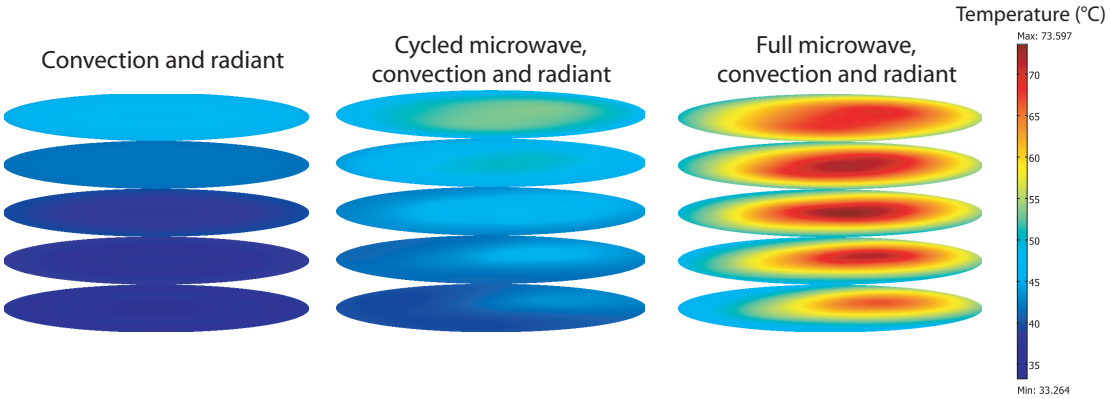

Figure 4.9: Computed spatial temperature maps for material with high initial moisture content heated using different combinations after 20 min of heating.

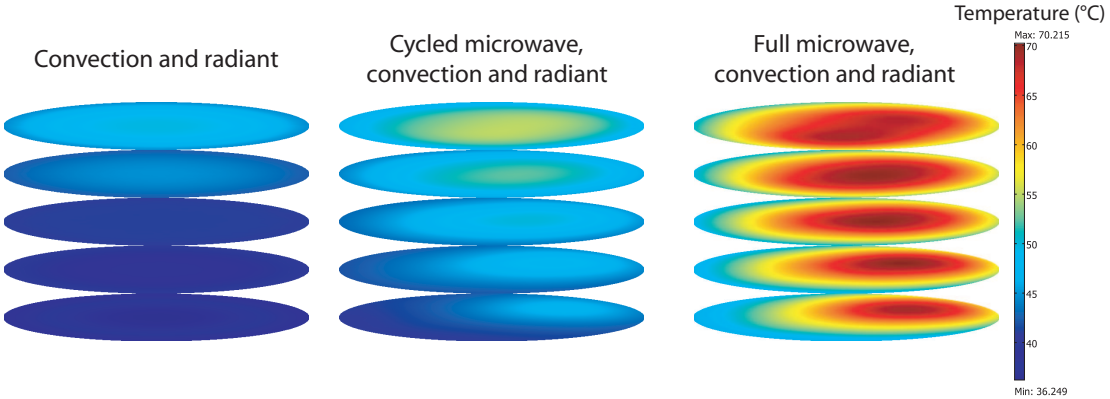

Figure 4.10: Computed spatial temperature maps for material with low initial moisture content heated using different combinations after 20 min of heating.

4.5.3 Moisture distributions for different heating combinations

4.5.4 Moisture distributions for different heating combinations

Many safety (microbiological/chemical) and quality attributes of the final food product are related to the total moisture and moisture distribution after the heating/cooking process, making them critical information. The overall moisture losses from the samples heated by different combinations are shown in Figure 4.11. More moisture is lost from

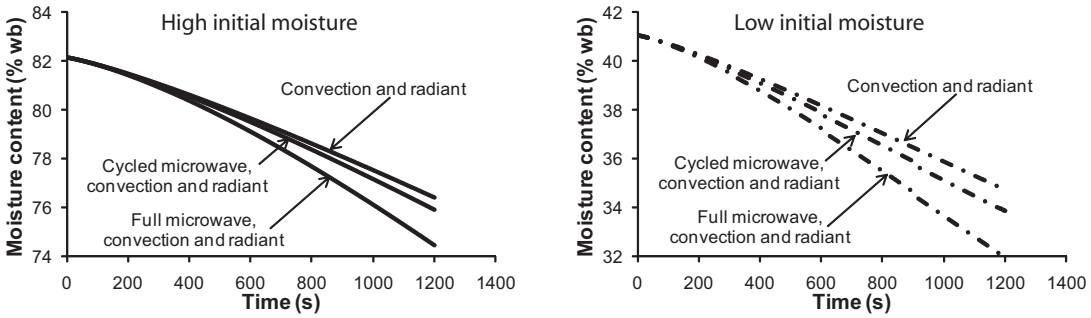

Figure 4.11: Computed average moisture content history for material with different initial moisture contents heated using three different combinations.

samples that are heated to higher temperatures since heating leads to increased evaporation and transport of water as water vapor in the porous medium. The moisture loss in 20 min from the high initial moisture samples are 7, 7.6 and 9.4% for convection and radiant, cycled microwave, convection and radiant, and full microwave, convection and radiant heating respectively. For the low initial moisture samples these are 15.4, 17.5 and 22.1% respectively, showing is a marked increase (more than two-fold) in the loss of moisture from the corresponding low initial moisture samples.

To determine the reason for the difference in moisture loss above, the total amount of water lost as liquid water and water vapor from the surface were calculated for the high and low moisture samples. At t = 20 min, for the high moisture sample heated using microwaves for the full time, the rate of loss of water as liquid and vapor was 3.02×10^{-6} and 1.84×10^{-7} kg/s, respectively. For the low moisture material, they were 1.36×10^{-6} and 1.28×10^{-6} kg/s, respectively. It can be observed that although the rate of water lost as liquid water reduces by half at low moisture content as the capillary diffusivity decreases (see Table 4.1), there is a ten-fold increase in moisture loss as vapor. This is attributed to the increase in temperatures as discussed for Figure 4.8 which leads to increased evaporation in the overall domain and the binary diffusion and pressure driven flow of vapor from the interior to surface.

High initial moisture content Figure 4.12 presents the moisture distribution in the high initial moisture samples after 20 min of heating. For convection and radiant heating, the moisture loss is mostly from the top surface with interior locations remaining at high moisture content even after 20 min of heating. The dominant mode of transport is capillarity which moves the liquid water to the surface and there is practically no pressure driven flow or binary diffusion of the vapor since the interior locations are not heated. The interior remains wet and the complete drying of the sample using only convective and radiant heating is therefore expected to take a very long time. In case of cycled microwave heating, there is additional mass transfer due to formation of vapor in the interior locations by evaporation and movement to the surface by binary diffusion and pressure driven flow. In case when the microwaves are on for the full time, very high heating rates are involved and there is increased evaporation leading to comparable moisture loss in the interior locations as well. In certain locations though, the moisture loss from the surface is not able to keep up with additional moisture coming from interior and therefore the locations close to the surface have higher moisture content. This is generally not desired during food preparation since it leads to soggy surface and is one of the known drawbacks of microwave heating. Interestingly, this is not observed when cycled microwaves are added and hence, careful addition of heating modes by matching the relative rates of heating may help in development of custom products by keeping the surface moisture low (crisp).

Low initial moisture content For the low initial moisture material, there is more variation in the moisture distribution even for convection and radiant heating (Figure 4.13). This is attributed to higher evaporation in the low moisture material discussed earlier. An interesting result observed here is that even when the microwaves are on for the full time, there is no accumulation of moisture in the surface unlike the high moisture ma-

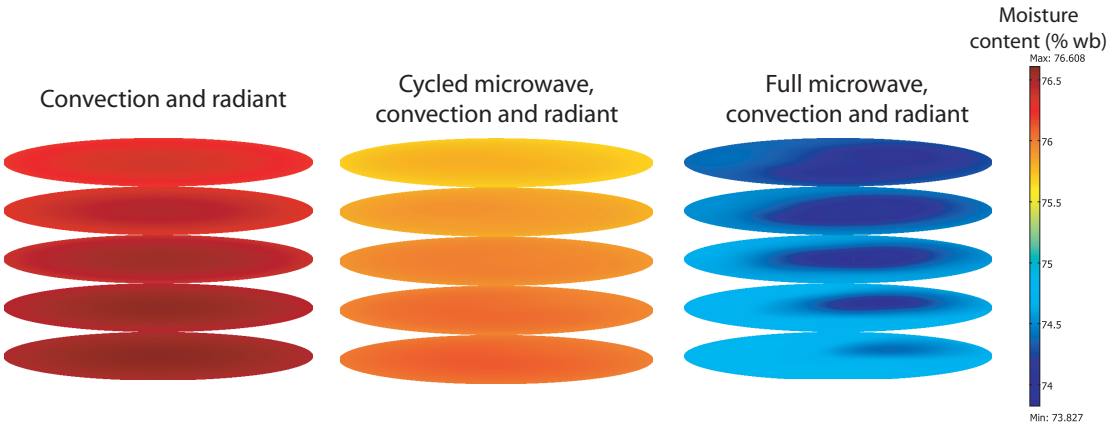

Figure 4.12: Computed moisture content maps for material with high initial moisture content heated using different combinations after 20 min of heating.

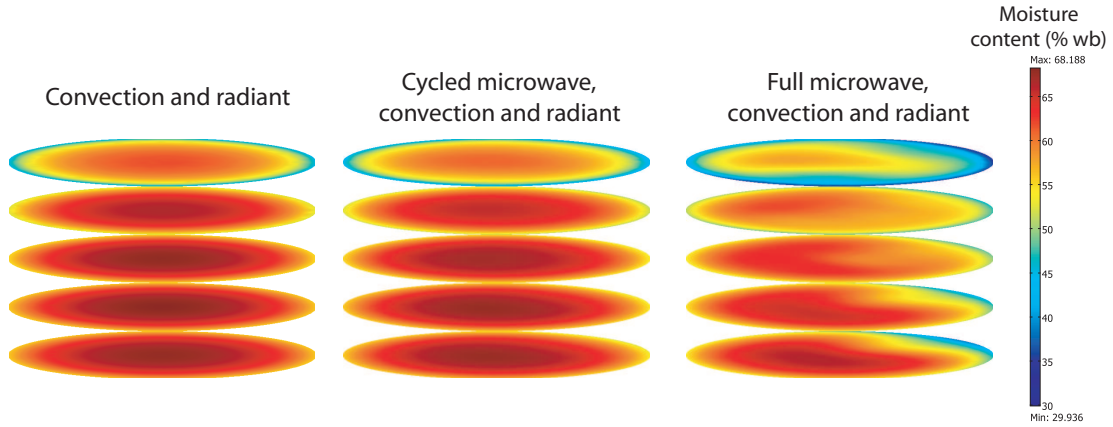

Figure 4.13: Computed moisture content maps for material with low initial moisture content heated using different combinations after 20 min of heating.

terial. The rate of evaporation of moisture due to convection and radiant heating near the surface becomes higher than that due to microwave heating which in turn facilitates moisture removal from the surface. This is also discussed in the next section.

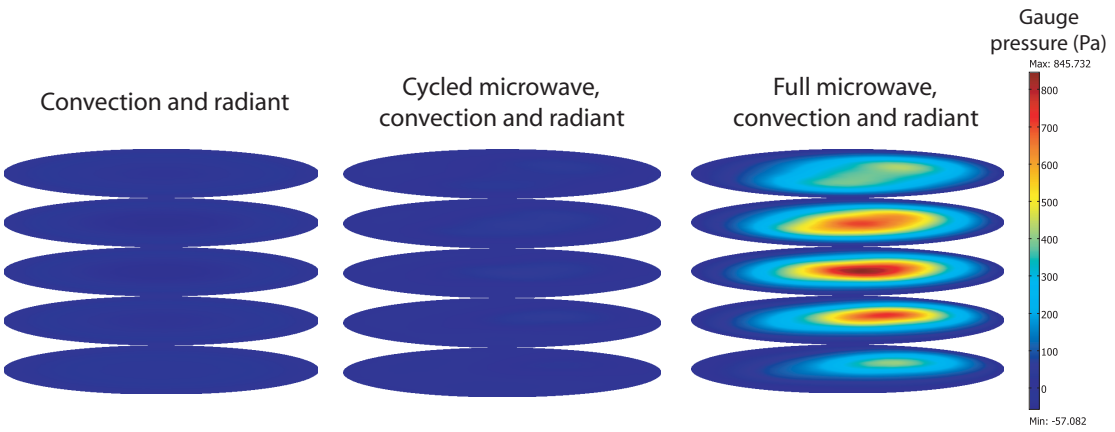

Figure 4.14: Computed pressure distributions for material with high initial moisture content heated using different combinations after 20 min of heating.

4.5.5 Pressure distributions for different heating combinations

High initial moisture content Pressure distributions (Figure 4.12) show that in convection and radiant heating negative pressures (minimum value of -57 Pa) are developed in the interior locations due to condensation of vapor. Very small positive pressures (maximum value of 0.375 Pa) are observed close to the surface due to evaporation. In case of cycled microwaves, pressures are mostly positive in the domain (maximum value of 50.8 Pa); however there are a few spots which have negative pressure (minimum value of -6.51 Pa) indicating condensation. Very high pressures are observed in the interior locations (maximum value of 845.7 Pa) and the pressures are positive throughout the domain when the microwaves are on for the full time as a result of the high microwave heating rate. A general trend is therefore seen here that convection and radiant heating leads to negative pressure development in the core of the domain whereas during microwave heating the pressures are generally positive.

Low initial moisture content In case of low moisture material (Figure 4.13), although there is negative pressure development in the core region (minimum value of -29.9 Pa),

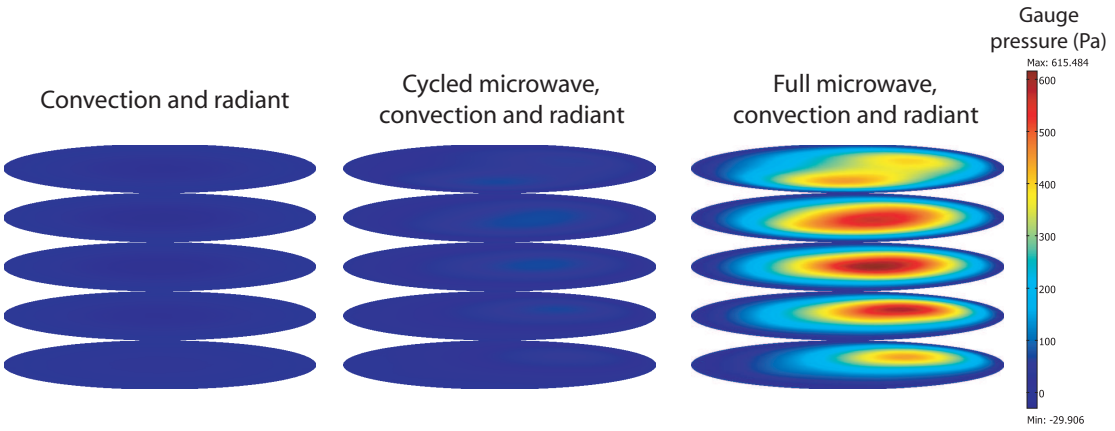

Figure 4.15: Computed pressure distributions for material with low initial moisture content heated using different combinations after 20 min of heating.

the positive pressures near the surface (maximum value of 4 Pa) are higher which supports the fact that there is greater evaporation near the surface in low moisture material as discussed earlier. For cycled microwave heating and with microwaves on for the full time, pressures are positive throughout the domain with maximum values of 72.3 Pa and 615.5 Pa respectively. Thus, the trend mentioned in the previous paragraph regarding the effect of heating modes on pressure development is also true here.

4.6 Summary and Conclusions

In this work, combination heating was studied the most comprehensive way, using a novel synergy of physics-based computation and MRI experimentation. This is also the first study that uses complex coupling of Maxwell's equations of electromagnetics in 3D with a multiphase porous media model to study combination heating. The coupling of different physics and MRI measurements both present unmatched computational and experimental challenges. The use of such a technique is, however, required in the study of combination heating processes, otherwise predictions of critical parameters such as

microwave energy deposition, temperature, moisture content and pressure in space and time are not possible. Knowledge of these factors can, in turn, lead to a quantum improvement in speed, quality and safety of food preparation, increased ability of automation and customization, retention of food nutrition and organoleptic qualities, reduction of food wastage, and increase of energy efficiency.

The key conclusions from the work are summarized as follows. (1) For a combination heating process that includes microwaves, distribution of parameters such as temperature and moisture content in 3D were obtained, that are critical to comprehensively understand and optimize the process. (2) More specifically, microwaves complement the convection and radiant heating regimes well. Also different mass transfer mechanisms were found to be dominant for different heating combinations; capillary flow for convective and radiant heating and pressure driven and binary diffusion for microwave heating. However, matching of relative power from convection and radiant heating, and microwaves is extremely critical to obtain a balanced heating rate in the material and to avoid formation of extreme regions of high temperature or excessive moisture. Generally the combination heating process provides uniform heating when the relative microwave power is substantially lower than the power due to convective and radiant heating. (3) High and low moisture materials behave differently under microwave combination heating. Higher temperatures and moisture loss was observed for low moisture material. It was found that low moisture materials can be heated uniformly using higher microwave power which is not possible in high moisture material. Therefore, these factors must be taken into consideration before designing a combination heating process. (4) Cycling of microwave is useful in distribution of excessive volumetric heat by microwaves and can increase the effectiveness of the combination heating process.

4.7 Acknowledgements

This project was supported by National Research Initiative Grant no. 2003-35503-13737 from the USDA Cooperative State Research, Education, and Extension Service Competitive Grants program. The authors also acknowledge Amit Halder (Dept. of Biological and Environmental Engineering, Cornell University, Ithaca) for providing the initial simulation files and Youngseob Seo (Dept. of Biomedical Engineering, University of California, Davis) for work in the initial part of the MRI measurement.

Nomenclature

Symbol	Description and unit
B_o	magnetic field strength, T
c	concentration, kg m^{-3}
c_p	specific heat capacity, J $kg^{-1}K^{-1}$
C	molar density, kmol m^{-3}
$D_{eff,g}$	effective gas diffusivity, m^2s^{-1}
D	capillary diffusivity, m^2s^{-1}
$\mathbf{E}$	electric field intensity, V m^{-1}
h	heat transfer coefficient, W $m^{-2}K^{-1}$
h_m	mass transfer coefficient of vapor, ms^{-1}
$\mathbf{H}$	magnetic field intensity, A m^{-1}
i	imaginary unit, $\sqrt{-1}$
$\dot{I}$	volumetric evaporation rate, $kgm^{-3}s^{-1}$
j	total mass flux, kg $m^{-2}s^{-1}$
k^{th}	thermal conductivity, $Wm^{-2}K^{-1}$
k	intrinsic permeability, m^2
k_r	relative permeability
K	non-equilibrium evaporation constant
m	overall mass fraction
M	moisture content, db
M_a, M_v	molecular weight of air and vapor
n	normal direction
P, p	total pressure and partial pressure, respectively, Pa
q	heat flux, W m^{-2}
Q	microwave source term, $Jm^{-3}s^{-1}$
R	universal gas constant, J $kmol^{-1}$ K^{-1}
S	saturation
t	time, s
T	Temperature, °C
TE	echo time, s
$\mathbf{v}$	velocity, m s^{-1}
V	volume, m^3
$x,\ y,\ z$	directions, m
Greek Symbols	
α	proportionality constant, ppm/°C
γ	magnetogyric ratio of hydrogen nucleus, rad/s T
ρ	density, kg m^{-3}
λ	latent heat of vaporization, J kg^{-1}
ω_a, ω_v	mass fraction of vapor and air with respect to total gas
ϕ	porosity
μ	dynamic viscosity, Pa s
ϵ_0	permittivity of free space, 8.854 x 10^{-12} Fm^{-1}
μ_0	permeability of free space, 4π x 10^{-7} Hm^{-1}
ϵ	complex relative permittivity
ϵ'	dielectric constant
ϵ''	dielectric loss
ω	angular frequency, rad s^{-1}
φ	phase shift, rad

BIBLIOGRAPHY

[1] Datta AK, Geedipalli SSR, Almeida MF. Microwave combination heating. *Food Technology*. 2005;59(1):36-40.

[2] Makoviny I, Zemiar J. Heating of wood surface layers by infrared and microwave radiation. *Wood Research*. 2004;49(4):33-40.

[3] Huang ZJ, Gotoh M, Hirose Y. Improving sinterability of ceramics using hybrid microwave heating. *Journal of Materials Processing Technology*. 2009;209(5):2446-2452.

[4] McMinn WAM, McLoughlin CM, Magee TRA. Thin-layer modeling of microwave, microwave-convective, and microwave-vacuum drying of pharmaceutical powders. *Drying Technology*. 2005;23(3):513-532.

[5] Vongpradubchai S, Rattanadecho P. The microwave processing of wood using a continuous microwave belt drier. *Chemical Engineering and Processing*. 2009;48(5):997-1003.

[6] Rakesh V, Datta AK, Amin MHG, Hall LD. Heating Uniformity and Rates in a Domestic Microwave Combination Oven. *Journal of Food Process Engineering*. 2009;32(3):398-424.

[7] Wappling-Raaholt B, Scheerlinck N, Galt S, Banga JR, Alonso A, Balsa-Canto E, Van Impe J, Ohlsson T, Nicolai BM. A combined electromagnetic and heat transfer model for heating of foods in microwave combination ovens. *Journal of Microwave Power and Electromagnetic Energy*. 2002;37(2):97-111.

[8] Durairaj S, Basak T. Analysis of pulsed microwave processing of polymer slabs supported with ceramic plates. *Chemical Engineering Science*. 2009;64(7):1488-1502.

[9] Basak T. Role of various elliptical shapes for efficient microwave processing of materials. *AIChE Journal*. 2007;53(6):1399-1412.

[10] Curet S, Rouaud O, Boillereaux L. Effect of sample size on microwave power absorption within dielectric materials: 2D Numerical Results vs. Closed-Form Expressions. *AIChE Journal*. 2009;55(6):1569-1583.

[11] Hansson L, Antti L. Modeling microwave heating and moisture redistribution in wood. *Drying Technology*. 2008;26(5):552-559.

[12] Brodie G. Simultaneous heat and moisture diffusion during microwave heating of moist wood. *Applied Engineering in Agriculture*. 2007;23(2):179-187.

[13] Sharma GP, Prasad S, Chahar VK. Moisture transport in garlic cloves undergoing microwave-convective drying. *Food and Bioproducts Processing*. 2009;87(C1):11-16.

[14] Halder A, Dhall A, Datta AK. An improved, easily implementable, porous media based model for deep-fat frying - Part I: Model development and input parameters. *Food and Bioproducts Processing*. 2007;85(C3):209-219.

[15] Ni H, Datta AK. Moisture, oil and energy transport during deep-fat frying of food materials. *Food and Bioproducts Processing*. 1999;77(C3):194-204.

[16] Yamsaengsung R, Moreira RG. Modeling the transport phenomena and structural changes during deep fat frying - Part 1: model development. *Journal of Food Engineering*. 2002;53(1):1-10.

[17] Turner IW, Perre P. Vacuum drying of wood with radiative heating: II. Comparison between theory and experiment. *AIChE Journal*. 2004;50(1):108-118.

[18] Ni H, Datta AK, Torrance KE. Moisture transport in intensive microwave heating of biomaterials: a multiphase porous media model. *International Journal of Heat and Mass Transfer*. 1999;42(8):1501-1512.

[19] Salagnac P, Glouannec P, Lecharpentier D. Numerical modeling of heat and mass

transfer in porous medium during combined hot air, infrared and microwaves drying. *International Journal of Heat and Mass Transfer*. 2004;47(19-20):4479-4489.

[20] Groombridge P, Oloyede A, Siores E. A control system for microwave processing of materials. *Journal of Manufacturing Science and Engineering-Transactions of the ASME*. 2000;122(1):253-261.

[21] Roussy G, Bennani A, Thiebaut JM. Temperature runaway of microwave irradiated materials. *Journal of Applied Physics*. 1987;62(4):1167-1170.

[22] Liu CM, Wang QZ, Sakai N. Power and temperature distribution during microwave thawing, simulated by using Maxwell's equations and Lambert's law. *International Journal of Food Science and Technology*. 2005;40(1):9-21.

[23] Akkari E, Chevallier S, Boillereaux L. Observer-based monitoring of thermal runaway in microwaves food defrosting. *J. Process Control*. 2006;16(9):993-1001.

[24] McCarthy MJ. Magnetic Resonance Imaging in Foods. Chapman and Hall, Inc., New York, NY. 1994.

[25] Nott KP, Hall LD. Validation and cross-comparison of MRI temperature mapping against fibre optic thermometry for microwave heating of foods. *International Journal of Food Science and Technology*. 2005;40(7):723-730.

[26] Haala J, Wiesbeck W. Modeling microwave and hybrid heating processes including heat radiation effects. *Ieee Transactions on Microwave Theory and Techniques*. 2002;50(5):1346-1354.

[27] Geedipalli SSR, Rakesh V, Datta AK. Modeling the heating uniformity contributed by a rotating turntable in microwave ovens. *Journal of Food Engineering*. 2007;82(3):359-368.

[28] Ghosh PK, Jayas DS, Smith EA, Gruwel MLH, White NDG, Zhilkin PA. Mathematical modelling of wheat kernel drying with input from moisture movement studies

using magnetic resonance imaging (MRI), Part I: Model development and comparison with MRI observations. *Biosyst. Eng.*. 2008;100(3):389-400.

[29] Hwang SS, Cheng YC, Chang C, Lur HS, Lin TT. Magnetic resonance imaging and analyses of tempering processes in rice kernels. *J. Cereal Sci.*. 2009;50(1):36-42.

[30] MacMillan B, Hickey H, Newling B, Ramesh M, Balcom B. Magnetic resonance measurements of French fries to determine spatially resolved oil and water content. *Food Res. Int.*. 2008;41(6):676-681.

[31] Bear J. Dynamics of Fluids in Porous Media, Dover Publications Inc, New York, NY. 1972.

[32] Datta AK. Porous media approaches to studying simultaneous heat and mass transfer in food processes. I: Problem formulations. *Journal of Food Engineering*. 2007;80(1):80-95.

[33] Halder A, Dhall A, Datta AK. Modeling Transport in Porous Media with Phase Change: Applications to Food Processing. Submitted to *Journal of Heat Transfer*. 2009.

[34] Choi Y, Okos MR. Thermal properties of liquid foods review, in Physical and Chemical Properties of Food, Okos MR (editor). American Society of Agricultural Engineers, St Joseph, MI. 1986: 35-77.

[35] Ratti C, Crapiste GH, Rotstein E. A New Water Sorption Equilibrium Expression for Solid Foods Based on Thermodynamic Considerations. *Journal of Food Science*. 1989;54(3):738-747.

CHAPTER 5

FULLY COUPLED SOLID MECHANICS- MULTIPHASE POROUS MEDIA MODEL

5.1 Abstract

Microwave puffing refers to significant structural changes in the material due to high pressure development caused by phase change during rapid heating. The process can be used to obtain low-fat healthy foods and ready-to-eat products to substitute deep fried foods. Microwaves provide an excellent means to perform puffing due to the high heating rates involved. The two-way coupling of the complex transport process and large deformations in the material, which is critical to accurately simulate the microwave puffing process, was implemented. A multiphase porous media model that includes different phases: solid, liquid water and gas and incorporates pressure driven flow and evaporation was used to describe the transport processes in the material. Large deformations were included to model volume change and the material was treated as hyperelastic. A moving Arbitrary Lagrangian-Eulerian (ALE) grid setting was used. The model was validated using surface temperature distribution, point temperature history, volume change and overall moisture loss experiments. The effect of various processing and operating conditions such as addition of other modes of heating, initial moisture content, sample size and relative humidity of the surroundings was studied to develop and optimize the process.

5.2 Introduction and objectives

In food processing, puffing is the rapid heating of food products to form vapor (and thus generate pressure) inside the material that in turn changes the food structure. Increased interest in the process is due to its ability to obtain low-fat healthy foods and ready-to-eat products that emulate deep fried foods[1–3]. Microwaves provide an excellent means to perform puffing due to the high heating rates involved. During the puffing process, the material is subjected to rapid heating using microwaves that leads to evaporation and pressure generation. This pressure build-up in turn causes the material to puff. The volume change in materials during processes such as potato puffing can be approximately[4] 15 to 25%. To develop and optimize this complex process, a comprehensive understanding of the process through physics-based modeling and experimentation is needed.

Microwave puffing is definitely a process with rapid heat and mass transfer combined with large deformations[1,5]. Although studies have been reported that aim to determine optimum processing conditions[4,7–10] by measuring properties[11–14] of fruits and vegetables for different puffing methods, attempts to understand the process comprehensively with the help of physics-based models are lacking with one exception in the case of vapor-induced puffing[15]. However, this particular work involves modeling bubble expansion in the pores in molten starch and does not consider the overall solid structure of the material which is critical and is intended in this work. Also, the model[15] is defined at a microscopic level and therefore does not include transfer of heat and water vapor in the continuum. Similarly, others have used bubble growth models for different applications [16,17]. Some others[18,19] have also used bubble growth models for studying extrusion and included transport of water vapor; however, these models used the effective diffusivity formulation, which does not describe the transport phenomena, especially pressure

driven flow and evaporation/condenstaion, comprehensively.

To model the microwave puffing process accurately, two way coupling effects of transport and large deformation need to be considered. The transport problem itself is very complex due to the presence of multiple phases- solid, liquid (water) and gas (air and water vapor); and multiple modes of transport- capillary flow, binary diffusion and pressure driven flow; along with rapid phase change (evaporation/ condensation). Researchers have implemented the transport problem with all the different components for varied applications[20–23] neglecting any deformation. Some have only considered heat transfer with small[24] or finite deformations[25]. Others have implemented relatively simple transport problems coupled with small deformation models that do not account for all the different phenomena mentioned earlier[26–28].

In case of microwave puffing, the solid mechanics problem becomes complex as well due to both geometric and material non-linearity. The structural changes in the material are large and hence large deformations have to be considered. Most of the modeling work that have included detailed transport formulation have only implemented small deformation version of the problem[29–32] that not only makes the problem simpler but cannot be applied to a process such as puffing where deformations are large. Moreover some of this work[29,30] use Luikov type models where the transport cannot be easily related to measurable physical processes. Some others have included empirical models for deformations[33]. Other researchers[34–37] have considered large deformations but their transport problem was not as complex with no phase change or hygroscopicity of the material. Yet others have included detailed transport but used linear constitutive relationships for large deformation problems[38,39]. In this work, we not only implement multiphase transport in a porous material but also consider large deformations for the solid mechanics problem. Although excellent texts exists that discuss similar problems

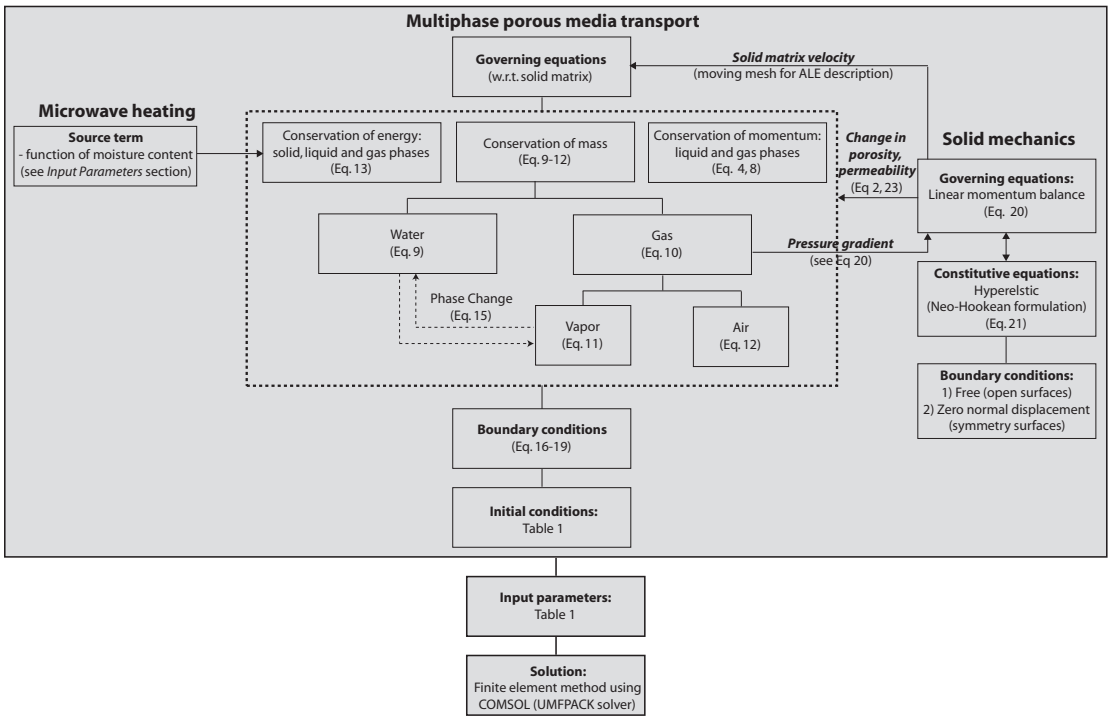

Figure 5.1: Flow chart showing the coupling between the different physics and the solution methodology.

especially in groundwater flow applications[40–42], in our knowledge this complete problem with all the transport and solid mechanics components has not been solved.

5.3 Mathematical model

As discussed earlier, the two-way coupling of multiphase porous media transport and solid mechanics (including large deformations) is critical to accurately simulate the microwave puffing process. The coupling is implemented by formulating the set of equations in a moving Arbitrary Lagrangian-Eulerian (ALE) grid setting[43,44]. The models for transport and solid mechanics, and their coupling are discussed in details in the following sections. The coupling is also shown schematically in Figure 5.1.

5.3.1 Transport– Multiphase porous media model

A 3D multiphase porous media model was formulated to describe the heat, mass and momentum transport during microwave puffing. The sample was considered porous[45] with three phases: solid, liquid water and gas. The gas phase had two components: water vapor and air. The schematic of a representative elementary volume (REV) of the material is shown in Figure 5.2a. The volume fraction of pores in a representative elementary volume of the material, ΔV, at any time t is denoted by porosity, ϕ:

$$\phi = \frac{\Delta V_p}{\Delta V} = \frac{\Delta V_w + \Delta V_g}{\Delta V} \tag{5.1}$$

where ΔV_w and ΔV_g are the volume occupied by liquid water and gas phases in the REV respectively. Note that this definition of porosity is generally what is considered in the porous media literature[45] and it includes the volume fraction of the gas as well as the liquid phase (water). This definition is different from the conventional meaning of porosity that only refers to gas phase volume fraction.

As the structure of the sample matrix changes due to deformation, the porosity changes. The volume of the solid matrix, however, does not change. Therefore the porosity, ϕ, at any time t in a deforming medium can be determined using the following relation:

$$(1 - \phi)\,\Delta V = (1 - \phi_0)\,\Delta V_0 \tag{5.2}$$

where ΔV_0 and ϕ_0 are the initial volume and porosity of a REV respectively.

Momentum balance

Darcy's law is considered for the flow of the movable phases (liquid water and gas) in the porous medium. For the deforming medium, the superficial velocity for each moving

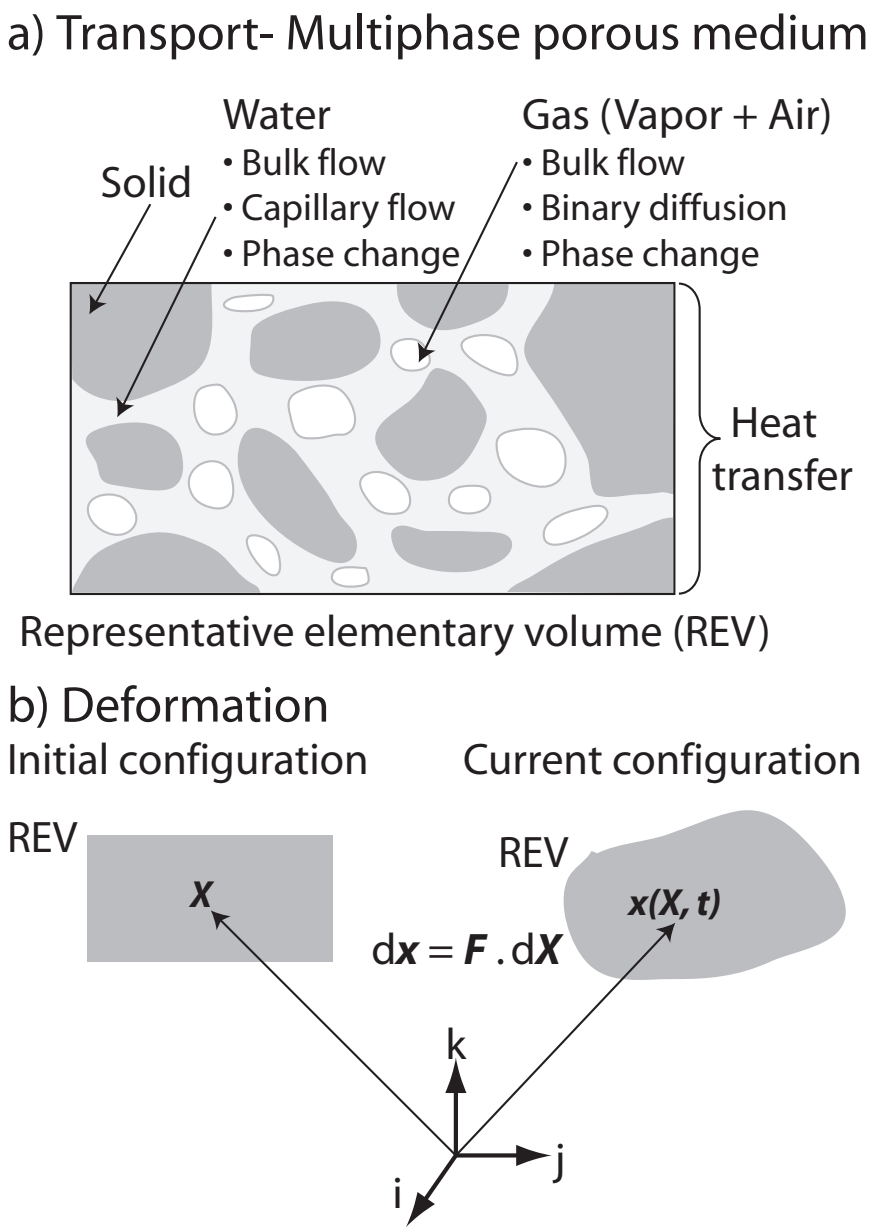

Figure 5.2: a) Representative elementary volume (REV) of the porous medium with the different phases and modes of transport considered. b) The initial and current configuration of a REV during deformation. Here **F** is the deformation gradient tensor.

phase due to the gas pressure gradient in the medium, with respect to the solid matrix velocity, $\mathbf{v_s}$, is therefore given by:

$$\mathbf{v_{sup,i\ s}} = -\frac{k_i k_{r,i}}{\mu_i}\nabla P \tag{5.3}$$

where $i = w$ denotes the liquid water phase and $i = g$ the gas phase. Here, the relative velocity, $\mathbf{v_{sup,i\ s}}$, is defined as $\mathbf{v_{sup,i\ s}} = \mathbf{v_{sup,i}} - \mathbf{v_s}$, and the total gas pressure is the sum of the partial pressures of vapor and air based on the ideal gas law, $P = p_a + p_v$. The relative velocity (with respect to the solid matrix) due to the gas pressure for each phase based on the volume occupied by that particular phase is therefore given by:

$$\mathbf{v_{i\ s}} = -\frac{1}{S_i\phi}\frac{k_i k_{r,i}}{\mu_i}\nabla P \tag{5.4}$$

where S_w and S_g are the liquid water saturation and gas saturation, respectively. The saturations, S_i, denote the volume fraction of the liquid or gas phase with respect to pore volume:

$$S_i = \frac{\Delta V_i}{\Delta V_p} = \frac{\Delta V_i}{\phi \Delta V} \tag{5.5}$$

Liquid water in the pores experiences capillary pressure, p_c, in addition to the gas pressure. Therefore,

$$p_w = P - p_c \tag{5.6}$$

The effective velocity of the liquid phase (with respect to the solid matrix) is therefore given by

$$\begin{aligned}
\mathbf{v_{eff,w\ s}} &= -\frac{1}{S_w\phi}\frac{k_w k_{r,w}}{\mu_w}\nabla p_w \\
&= -\frac{1}{S_w\phi}\frac{k_w k_{r,w}}{\mu_w}\nabla P + \frac{1}{S_w\phi}\frac{k_w k_{r,w}}{\mu_w}\nabla p_c \\
&= \mathbf{v_{w\ s}} + \frac{1}{S_w\phi}\frac{k_w k_{r,w}}{\mu_w}\frac{\partial p_c}{\partial S_w}\nabla S_w
\end{aligned} \tag{5.7}$$

Equation 5.7 can be rewritten in terms of capillary diffusivity[46], $D_c = -\frac{k_w k_{r,w}}{\phi \mu_w} \frac{\partial p_c}{\partial S_w}$, and water concentration, $c_w = \rho_w \phi S_w$:

$$\mathbf{v_{eff,w\ s}} = \mathbf{v_{w\ s}} - \frac{D_c}{c_w} \nabla c_w \tag{5.8}$$

Mass balance

The mass balance equation for the transportable phases includes the effects of bulk flow (convection), binary diffusion (gas phase) and capillary flow (liquid phase). Mass conservation equation for the liquid water phase includes the bulk flow, capillary flow and phase change. The equation is written using the ALE description with the mesh moving with the solid matrix velocity $\mathbf{v_s}$[39]:

$$\frac{\partial c_w}{\partial t} + (\mathbf{v_w} - \mathbf{v_s}) \cdot \nabla c_w + c_w \nabla \cdot \mathbf{v_w} = \nabla \cdot (D_c \nabla c_w) - \dot{I} \tag{5.9}$$

Similarly, the continuity equation for the gas phase is given by:

$$\frac{\partial c_g}{\partial t} + \left(\mathbf{v_g} - \mathbf{v_s}\right) \cdot \nabla c_g + c_g \nabla \cdot \mathbf{v_g} = \dot{I} \tag{5.10}$$

Mass balance equation for the vapor component of the gas phase includes bulk flow, binary diffusion and phase change:

$$\frac{\partial c_v}{\partial t} + \left(\mathbf{v_g} - \mathbf{v_s}\right) \cdot \nabla c_g + c_g \nabla \cdot \mathbf{v_g} = \nabla \cdot \left(S_g \phi \frac{C^2}{\rho_g} M_a M_v D_{eff,g} \nabla x_v \right) + \dot{I} \tag{5.11}$$

Here vapor concentration is related to the gas concentration by its mass fraction, $c_v = \omega_v c_g$. Similarly, concentration of air, c_a, is $\omega_a c_g$. The mass fraction of air can be calculated using the mass fraction of vapor from Equation 5.11:

$$\omega_a = 1 - \omega_v \tag{5.12}$$

Energy balance

The energy balance equation is solved for the mixture and the effect of microwave heating is included as a source term. Detailed discussion regarding microwave source term calculation is included in the Input Parameter section. Energy conservation includes convection due to moving phases, conduction, phase change and microwave power absorption term:

$$\begin{aligned} \frac{\partial}{\partial t}\left[\sum_{i=s,w,v,a}\left(c_i c_{p,i} T\right)\right] &+ \sum_{i=w,v,a}\left(\mathbf{v_i}-\mathbf{v_s}\right)\cdot\nabla\left(c_i c_{p,i} T\right) + \sum_{i=w,v,a}\left(c_i c_{p,i} T\ \nabla\cdot\mathbf{v_i}\right) \\ -c_{p,w} T\ \nabla\cdot\left(D_c \nabla c_w\right) &= \nabla\cdot\left(k_{eff}\nabla T\right) - \lambda\dot{I} + Q_{mic} \end{aligned} \tag{5.13}$$

Here the effective thermal conductivity is given by the volume weighted average of the different phases and components:

$$k_{eff} = \left(1-\phi\right)k_s^{th} + \phi\left\{S_w k_w^{th} + S_g\left(\omega_v k_v^{th} + \omega_a k_a^{th}\right)\right\} \tag{5.14}$$

Evaporation/ Condensation

The porous media model incorporates the change of phase between liquid water and vapor (evaporation/ condensation) throughout the domain using the following expression [20]:

$$\dot{I} = K_{evap}\frac{M_v}{RT}\left(p_{v,eq} - p_v\right) \tag{5.15}$$

where $p_{v,eq}$ is the equilibrium vapor pressure which is a function of both temperature and moisture content of the material.

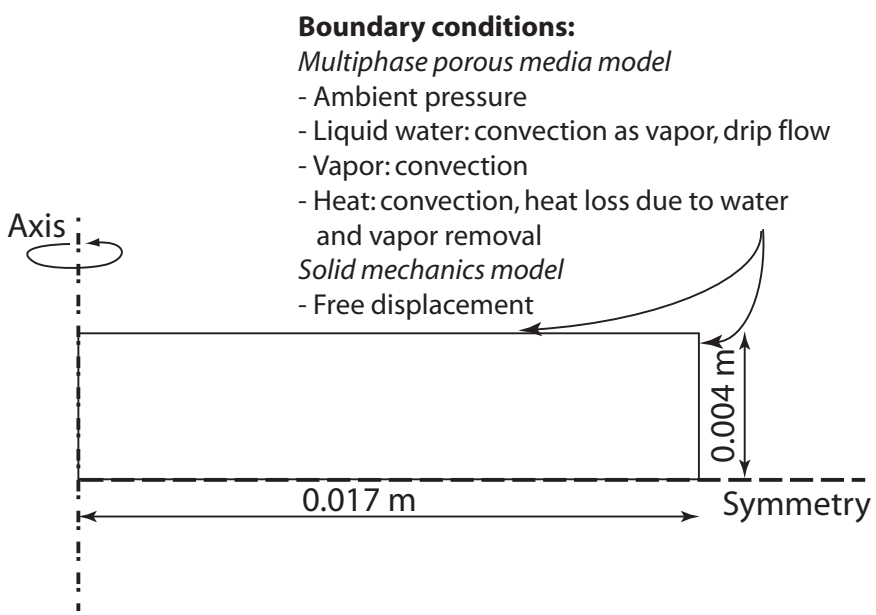

Figure 5.3: Schematic and boundary conditions for the problem.

Boundary conditions

The boundary conditions for the transport problem are now listed and are also shown in Figure 5.3. Pressure was set to ambient at the open surfaces (top and right boundaries in Figure 5.3):

$$P|_s = P_{amb} \tag{5.16}$$

Water from the interior can move out of the boundary as vapor after evaporation. When the liquid water saturation becomes high ($S_w = 1$), water can also move out of the open surfaces directly by drip flow. Therefore,

$$j_{n,w}|_s = h_m \phi S_w \left(\rho_v - \rho_{v,\,oven}\right) + \underbrace{c_w v_{n,w}}_{\text{when } S_w = 1} \tag{5.17}$$

where $j_{n,w}$ is the total normal flux of water at a particular surface. Vapor can be convected away from the open surfaces. Therefore,

$$j_{n,v}|_s = h_m \phi S_g \left(\rho_v - \rho_{v,\,oven}\right) \tag{5.18}$$

The air inside the microwave is at room temperature; the surface of the sample therefore is subjected to cooling by convection. The loss of heat due to evaporation of water, removal of liquid water (during drip flow) and vapor is also included in the boundary condition for heat transfer:

$$\begin{aligned} q_n|_s &= h(T - T_{amb}) - h_m \phi S_w \left(\rho_v - \rho_{v,\,oven}\right) \lambda \\ &- h_m \phi \left(S_w + S_g\right) \left(\rho_v - \rho_{v,\,oven}\right) c_{p,v} T - \underbrace{c_w v_{n,w} c_{p,w} T}_{\text{when } S_w = 1} \end{aligned} \tag{5.19}$$

where q_n is normal heat flux.

Initial Conditions

The initial conditions for the different variables are listed in the input parameters table (Table 5.1).

5.3.2 Solid Mechanics

To determine the deformation in the material during the puffing process, a solid mechanics model needs to be formulated and solved. The model includes geometric as well as material non-linearity. Large deformations in the REV and the deformation gradient tensor for the mapping are illustrated in Figure 5.2b.

Linear momentum balance

The linear momentum balance is solved to obtain the stresses. Since large deformations are involved, Lagrangian measures of stress and strain are used. The gas pressure

gradient causes the deformation. Therefore,

$$\nabla_X \cdot \left(\mathbf{S} \cdot \mathbf{F}^{\mathbf{T}}\right) - \nabla P = 0 \tag{5.20}$$

where **S** is the second Piola-Kirchhoff (PK2) stress tensor, **F** is the deformation gradient tensor and P is the gas pressure. Notation X refers to the Lagrangian reference frame. The PK2 stress is related to the Cauchy stress, which is normally used for small deformation problems, by

$$\mathbf{S} = J\mathbf{F}^{-1} \cdot \sigma \cdot \mathbf{F}^{-T} \tag{5.21}$$

where J is the Jacobian determinant of the deformation gradient tensor, **F**. The strain measure is the Green-Lagrange (or Green) strain tensor, **E**, given by

$$\mathbf{E} = \frac{1}{2}\left(\mathbf{F}^T \cdot \mathbf{F} - \mathbf{I}\right) \tag{5.22}$$

The stored energy function relates the stress and strain tensors

$$\mathbf{S} = \frac{\partial W}{\partial \mathbf{E}} \tag{5.23}$$

To solve Equation 5.20, we need to consider an appropriate material model (constitutive equations) and thereby determine the form of this stored energy function. This is now discussed.

Constitutive equations

As discussed earlier, during puffing large deformation of the material is involved. A non-linear material model (stress-strain relationship), therefore, needs to be used to obtain a consistent formulation for the problem. The linear Hooke's law of elasticity is applicable only for the special case of small deformations and is not valid in this case. The hyperelastic Neo-Hookean material model is an extension of the Hooke's Law of

elasticity to large deformations. Therefore, the Neo-Hookean formulation is considered for the problem. The stored energy function for a Neo-Hookean material is given by[43]:

$$W = \frac{K}{2}(J-1)^2 - \frac{G}{2}\left(\overline{I}_1 - 3\right) \tag{5.24}$$

where K and G are the initial bulk and shear modulus respectively. Here $\overline{I}_1$ is the first invariant (trace) of the right Cauchy-Green tensor, $\overline{\mathbf{C}}$ ($= \overline{\mathbf{F}}^T \cdot \overline{\mathbf{F}}$), for the volume preserving (deviatoric) part. The first and second terms on the right in Equation 5.24 are the volumetric and deviatoric contributions, respectively. The multiplicative split of the deformation gradient tensor into volumetric and deviatoric parts is defined by[47]

$$\mathbf{F} = J^{\frac{1}{3}}\,\overline{\mathbf{F}} \tag{5.25}$$

where $J^{\frac{1}{3}}$ is the volumetric part and $\overline{\mathbf{F}}$ is the volume preserving part. By definition, the Jacobian determinant of the deformation gradient tensor for the volume preserving part should be unity, which can be confirmed from Equation 5.25. It can be observed that the multiplicative split for the large deformation case is analogous to the case of small deformation where an additive split of the volumetric and deviatoric parts is used ($\varepsilon = \mathbf{e} + 1/3\ \mathrm{tr}[\varepsilon]\ \mathbf{I}$). Finally, the deformation causes change in porosity which is given by Equation 5.2.

Boundary conditions

The normal displacements on the symmetry boundaries to set to zero (see Figure 5.3). The other boundaries have no constraints and are free to move.

Table 5.1: Input parameters for the simulations

Parameter	Value	Source
Sample size (m)	0.034 (dia) × 0.008 (h)	
Viscosity		
Water, μ_w (Pa s)	0.988×10^{-3}	
Vapor and air, μ_g (Pa s)	1.8×10^{-5}	
Intrinsic permeability		
Water, k_w (m^2)	5×10^{-16}	58
Vapor and air, k_g (m^2)	2×10^{-15}	58
Relative permeability		
Water, $k_{r,w}$	$[(S_w - 0.09)/0.91]^3 \ f(\phi), \quad S_w > 0.09$ $0, \quad S_w < 0.09$	45
Vapor and air, $k_{r,g}$	$[1 - 1.1S_w]f(\phi), \quad S_w < 1/1.1$ $0, \quad S_w > 1/1.1$	45
Capillary diffusivity (water), D_c (m^2/s)	$4.5 \times 10^{-7} \exp(-2.8 + 2\mathrm{M})$	
Binary diffusivity, $D_{eff,g}$ (m^2/s)	2.6×10^{-5}	58
Specific heat capacity		
Solid, c_{ps} (J/kg K)	1650	65
Water, c_{pw} (J/kg K)	4178	65
Vapor, c_{pv} (J/kg K)	2062	65
Air, c_{pa} (J/kg K)	1006	65
Thermal conductivity		
Solid, k_s^{th} (W/m K)	0.21	65
Water, k_w^{th} (W/m K)	0.57	65
Vapor, k_v^{th} (W/m K)	0.026	65
Air, k_a^{th} (W/m K)	0.026	65
Density		
Solid, ρ_s (kg/m^3)	1530	
Water, ρ_w (kg/m^3)	998	
Vapor, ρ_v (kg/m^3)	Ideal gas law	
Air, ρ_a (kg/m^3)	Ideal gas law	
Latent heat of vaporization, λ (J/kg)	2.26×10^6	
Evaporation rate constant, K (/s)	1×10^{-3}	20
Equilibrium vapor pressure, $p_{v,eq}$ (Pa)	$p_{sat}(T) \exp(-0.0267M^{-1.656}$ $+0.0107e^{-1.287M} M^{1.513} \ln[p_{sat}(T)])$	66
Ambient pressure, P_{amb} (Pa)	101325	
Mass transfer coefficient, h_m (m/s)	0.011	21
Heat transfer coefficient, h (W/m^2 K)	20	21
Ambient temperature, T_{amb} (°C)	22	
Microwave source term, Q_{mic} (W/m^3)	$1.5 \times 10^7 [M_0/M]^{-1.17}$	
Bulk modulus, K (Pa)	4.594×10^5	48,52
Shear modulus, K (Pa)	7.94×10^4	51
Initial Conditions		
Porosity, ϕ_0	0.80	67
Pressure, P_0 (Pa)	101325	
Water concentration, $c_{w,0}$ (kg/m^3)	459	
Vapor mass fraction, $\omega_{v,0}$	0.01	
Temperature, T_0 (°C)	22	

5.3.3 Input parameters

All input parameters used for the simulations are listed in Table 5.1. Some of the input parameters are discussed here.

Porosity factor for water and gas permeability The porosity of material (as defined by Equation 5.1) changes with deformation as given by Equation 5.2. With change in porosity of the material, liquid and gas permeabilities also change. The porosity factor, $f(\phi)$, in the Kozeny-Carman equation relates the liquid and gas permeability to the porosity[45]. It is given by:

$$f(\phi) = \left(\frac{\phi}{\phi_0}\right)^3 \left(\frac{1-\phi_0}{1-\phi}\right)^2 \tag{5.26}$$

The liquid and gas permeability values were multiplied by this factor to include the effect of porosity change on permeability in the model.

Bulk Modulus From literature[48], the bulk modulus of raw uncooked potato was found to be 5 MPa. However, the same work[48] acknowledged that the modulus would decrease as the cell walls degrade during cooking or heating causing softening of potato samples. Others[49–52] have also shown that different processing conditions such as drying and microwave heating change the mechanical properties (e.g. Young's modulus) of raw potatoes substantially. They, however, did not measure the bulk modulus or the Poisson's ratio. In comparing boiling and microwave heating of potatoes[52], microwave heating was shown to result in more significant changes in mechanical properties of raw potato due to advanced changes in the microstructure of potato tubers, and breakdown of hemicellulose and cellulose components with changes in cell appearance that can include cell separation. Their data showed a 91% decrease in mechanical properties

during microwave heating as compared to the raw state. Based on the bulk modulus value of raw potatoes undergoing microwave heating, a bulk modulus of 459.4 kPa was used for this study.

Shear modulus A shear modulus value of 79.4 kPa was obtained from literature[51] for microwave heated potatoes.

Microwave source term Since the sample size is very thin (Table 5.1), a uniform microwave power absorption was assumed in the sample initially. The initial power was measured using the IMPI 2l test[53]. The power was scaled to account for the lower volume of the sample using data for power absorbed as function of sample volume from literature[54]. At later times, the microwave power was a function of moisture content and the relation (listed in Table 5.1) was also obtained from published literature[21].

5.3.4 Solution details

Since the sample was cylindrical, a 2D axisymmetric geometry was considered, as shown in Figure 5.3, to reduce computational requirements. The governing equations were solved in COMSOL Multiphysics 3.5a (COMSOL Inc., Burlington, MA) using the UMFPACK direct solver with a maximum time step of 0.01 s. The procedure followed for solving the coupled problem is schematically illustrated in Figure 5.1. A tetrahedral mesh with 13128 elements was used based on mesh convergence analysis (not shown here). The simulations were run on a 3 GHz Windows workstation with 16 Gb memory.

5.4 Experimental methodology

Potato samples were used to study the microwave puffing process experimentally. Cylindrical samples were obtained by cutting fresh Russet potatoes using a punch. The experimental methodology used in literature for hot-air puffing of potatoes[4] was followed. The cylindrical samples were initially blanched for 2 min by placing them in boiling water. Blanching was performed to stop enzyme action and soften the samples. Drying was then carried out at 90°C for 80 min in a hot air oven (Thermador JetDirect oven, Model CJ302UB, Enersyst Development Center, Dallas, Texas). The samples were dried slowly to a low moisture content ($\sim$1.6-1.8 db) so that a partially impermeable layer was formed at the surface that would restrict escape of gases during puffing. Puffing was then performed by subjecting the samples to rapid heating using microwaves for 60 s. Point temperatures were measured as functions of heating time in the sample during the puffing process using a fiber optic system (Fiso Technologies, Quebec, Canada). Spatial distribution of temperature at the surface of the samples was obtained using an infrared thermal imaging camera (FLIR A320, FLIR Systems, Boston, MA). Moisture loss was determined as a function of time by puffing samples to different times and measuring the weight loss. The change in volume of the samples during puffing was measured using the rapeseed displacement method[55] with an accuracy of 0.5 cm^3.

5.5 Results and Discussion

Validation of the model was done by comparing the computed results with the experimental measurement of temperature and moisture loss histories and volume change. Transient and spatial temperature, moisture, pressure, evaporation rate and porosity during the puffing process are discussed in this section, followed by sensitivity analysis of

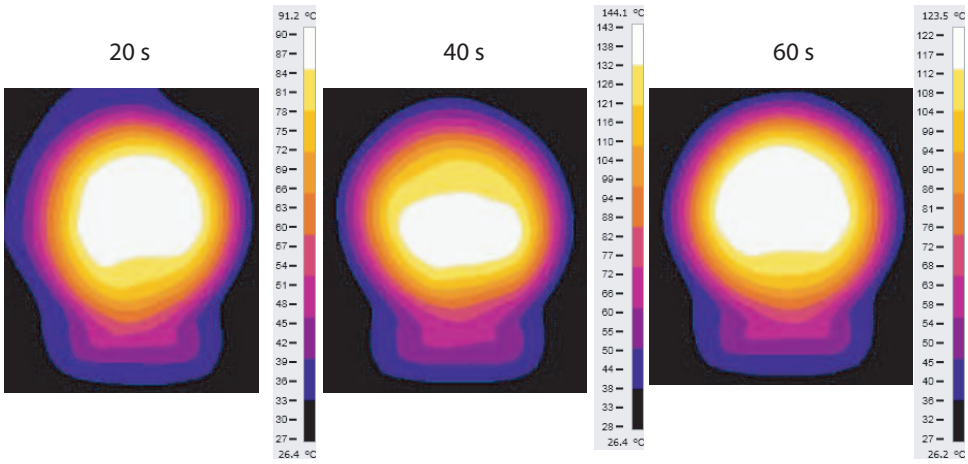

Figure 5.4: Spatial temperature distribution on the surface of the samples as obtained from the thermal imaging camera after different times during puffing.

the model to input parameters.

5.5.1 Experimental validation

Spatial temperature distribution at the sample surface The spatial temperature profiles at the sample surface at different times during puffing obtained from infrared thermal imaging is shown in Figure 5.4. Very high temperatures are observed after 60 s of puffing. In 60 s, most of the moisture is released in the form of liquid water due to drip flow and as water vapor. The residual mass comprises mostly of the solid matrix whose temperatures become very high. The highest temperature is obtained after 40 s and then it starts to fall as the microwave power absorption reduces due to moisture loss while cooling takes place at the surface. It can also be observed that the temperature contours are fairly symmetric in the axial direction; thereby justifying the use of an axi-symmetric model to reduce computational requirements. These temperatures maps obtained from thermal imaging were then used to determine temperatures in the axial direction and were compared with the simulated results, as shown in Figure 5.5. The

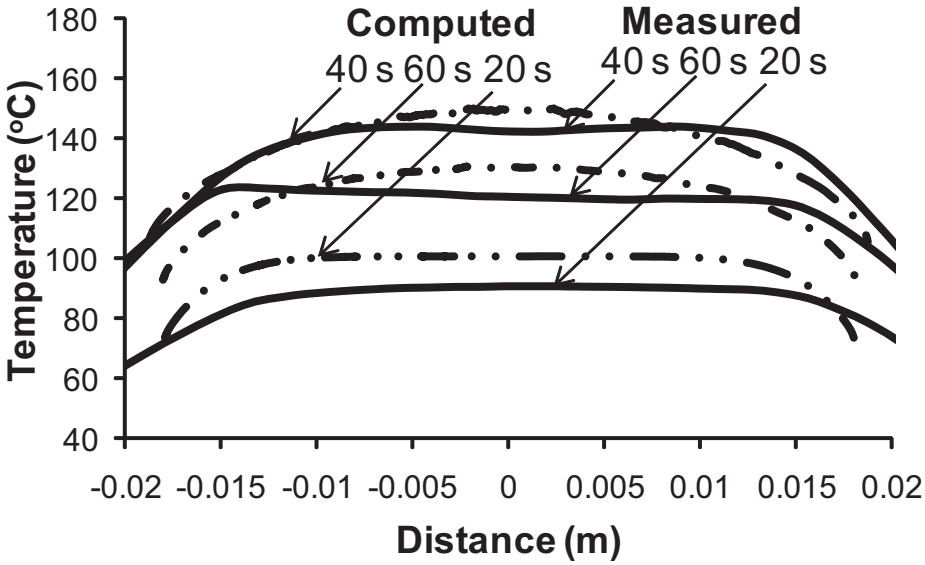

Figure 5.5: Computed and measured (using thermal imaging camera) temperature distribution at the top surface of the samples at different times.

comparisons are seen to be quite good. The experimental temperatures are expected to be lower since temperature measurement using the infrared camera was done after the puffing process and the time lag ($\sim$10 s) may have lead to cooling.

Temperature history To perform a more detailed validation, temperature histories were obtained from experiments at a region about 2 mm below the surface of the sample and halfway from the axis. The location of this region is approximate since it was nearly impossible to position the fiber optic probe exactly due to the small dimension of the sample and the finite thickness of the probe. In addition, the size of the sample changes considerably during the puffing process. The point temperature measurements therefore only provide a qualitative assessment of the temperature ranges that are observed during the puffing process. Three different measurements are shown in Figure 5.6 along with the predicted temperature history at the point. The temperatures predicted by the model are found to be consistent with the measured values.

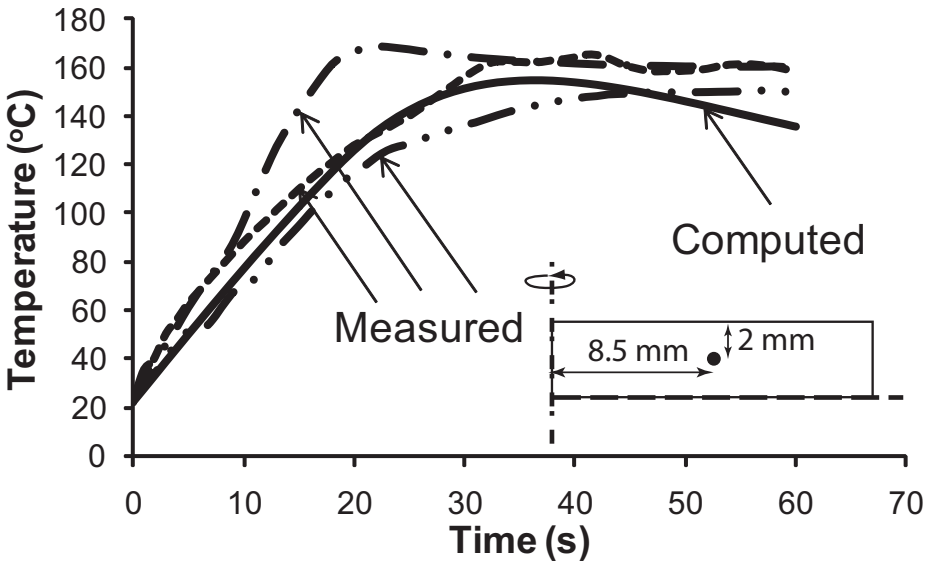

Figure 5.6: Computed and measured (using fiber optic probes) temperature history at a point 2 mm from the top surface and halfway from the axis of the sample (as shown).

Moisture loss Moisture loss obtained from the computational model as function of time was found to closely match those determined gravimetrically as shown in Figure 5.7.

Volume change The volume change predicted by the model was compared to the experimentally measured values as shown in Figure 5.8. The general trend of volume change predicted by the model was found to match the experimental result. A more accurate determination of the solid mechanics parameters (bulk modulus and shear modulus) and increasing the accuracy of the volume measurement may lead to a better match. A detailed uncertainty analysis is presented later. The increase in volume with time initially, followed by a decrease, is attributed to the decrease in microwave heating due to moisture loss. As a result, evaporation decreases and there is less vapor formation leading to lower pressures in the domain. However, there is a constant loss of vapor at the surface which further decreases pressures in the domain and thereby the volume of

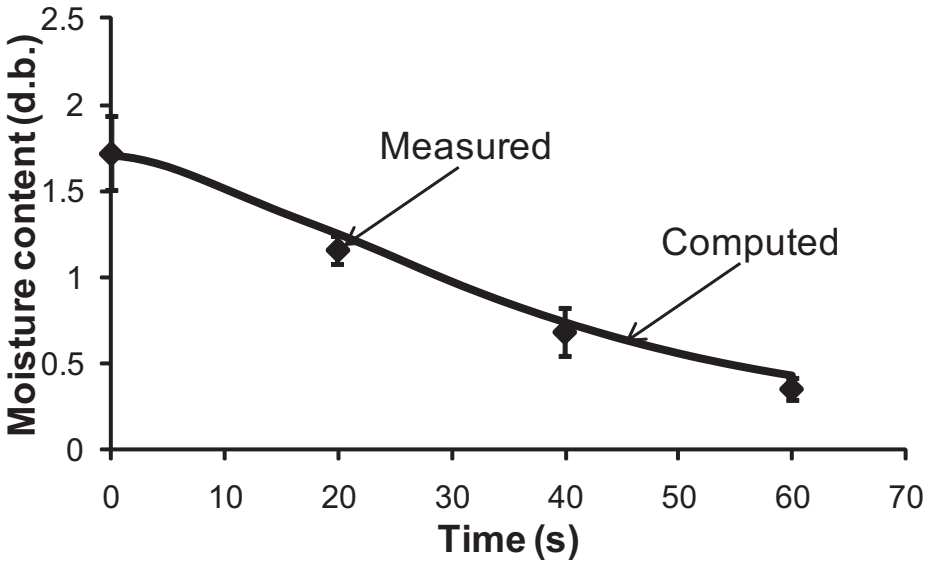

Figure 5.7: Computed and measured (determined from weight loss) moisture content in the samples as a function of puffing time. Error bars represent the standard deviation for three measurements.

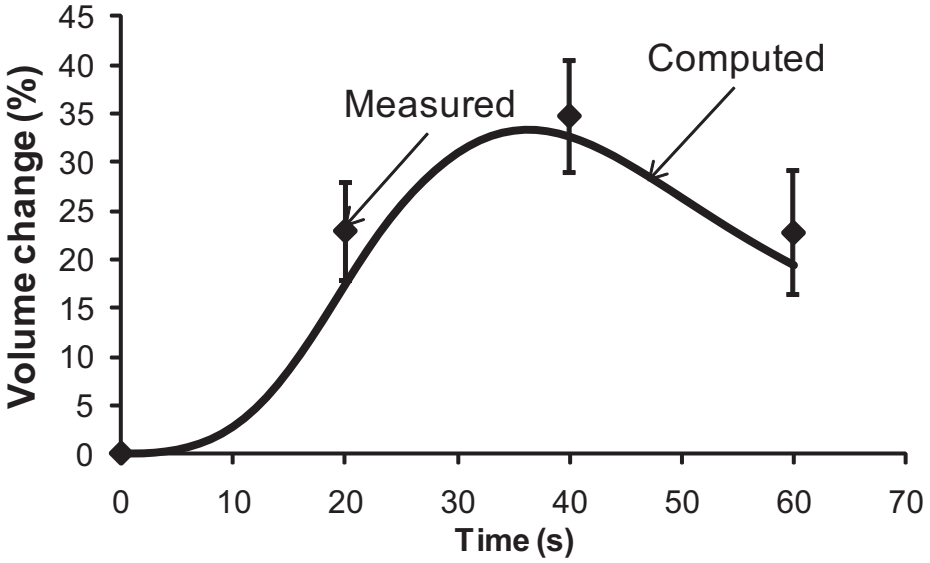

Figure 5.8: Computed and measured (determined using rapeseed displacement method) volume change in the samples as a function of puffing time.

the sample decreases. Maximum volume around the same time ($\sim$40 s) has also been reported earlier[56]. The change in structure of the sample at different times during the puffing process along with the deformed mesh are shown in Figure 5.9. There is considerable change in volume during the puffing process. From Figure 5.8, it can be observed that the overall change is about 20%. It is consistent with a previous study[4] which also reported about 25% volume change for hot air puffing (at 200°C) of potatoes determined using experiments.

As could be expected, large variability in the property values between potatoes samples exists due to the natural textural non-uniformity. These could also lead to inconsistency in comparison of the computed and measured variables. However, based on the experimental comparisons of the three model parameters (temperature, moisture, volume change), the model is considered to be validated. The analysis of the results are now presented along with the sensitivity analysis to determine variables that affect the puffing process.

5.5.2 Change in temperature, moisture, evaporation rate, pressure, and porosity during puffing

Temperature, moisture, evaporation rate, pressure and porosity distribution in the domain at different times during puffing obtained from the simulation are shown in Figures 5.10-5.14. Temperatures in the interior of the sample increase with puffing time due to microwave heating. The sample surface is exposed to the air at room temperature which cools the surface. The temperatures are, therefore, generally higher in the interior.

Liquid water moves due to the action of the capillary forces. It is lost from the

Figure 5.9: The deformed domain of the sample with the respective meshes at different times during the puffing process.

surface by evaporation to water vapor and by drip flow, when surface water saturation becomes close to unity. As temperature increases due to rapid heating, liquid water also evaporates over the whole domain (Figure 5.12) forming water vapor that moves more readily to the surface from where it is convected away. The moisture content at the surface (Figure 5.11) is, therefore found to be very low as a result of these loses. With time, considerable moisture is lost throughout the domain (from 1.7 d.b to 0.4 d.b.).

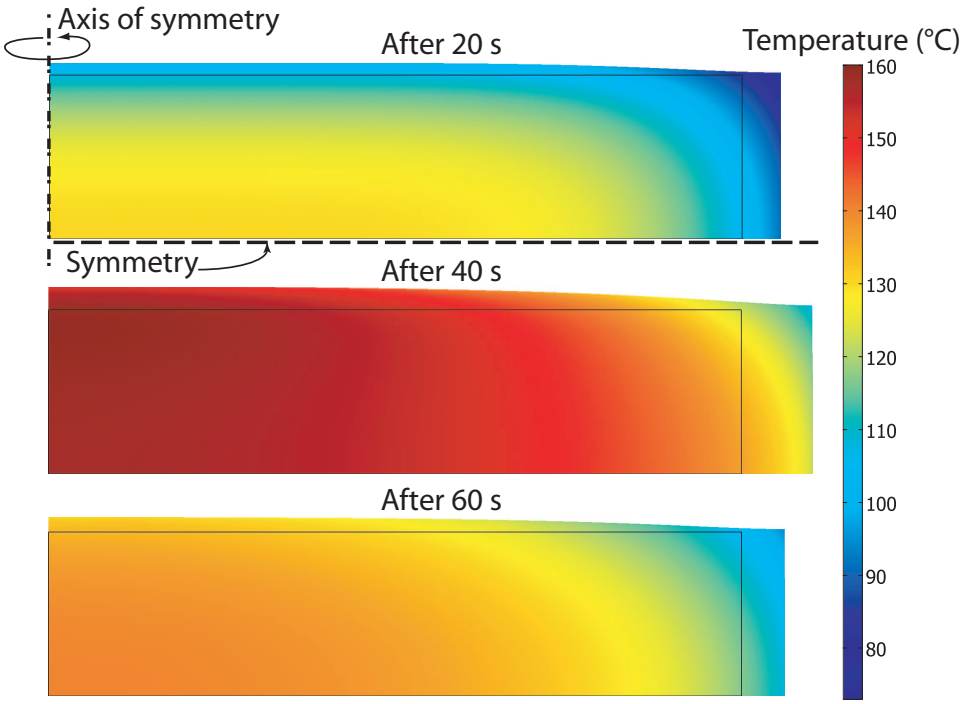

Figure 5.10: Computed temperatures inside the sample at different times during puffing. The initial moisture content of the sample was 22°C. The inner rectangle represents the initial dimensions before puffing.

In a comprehensive review of puffing process for biological materials[1], it was reported that the optimum moisture content of puffed products are in the range of 0.16-0.54 d.b, which is consistent with this study.

The porosity of the material changes due to the change in structure. As more liquid water evaporates into vapor, the pressure inside the medium increases. It can be seen from Figure 5.13 that significantly high pressures are developed. These high pressures in turn causes the material to deform (shown in Figure 5.9). The very large deformations cause significant change in porosity (defined by Equation 5.1) of the material (Figures 5.14) as given by Equation 5.2. However, a feedback mechanism comes into play that prevents further increase in pressure. As porosity increases, there is a drastic increase in the permeability, as given by the Kozeny-Carman porosity factor (Equa-

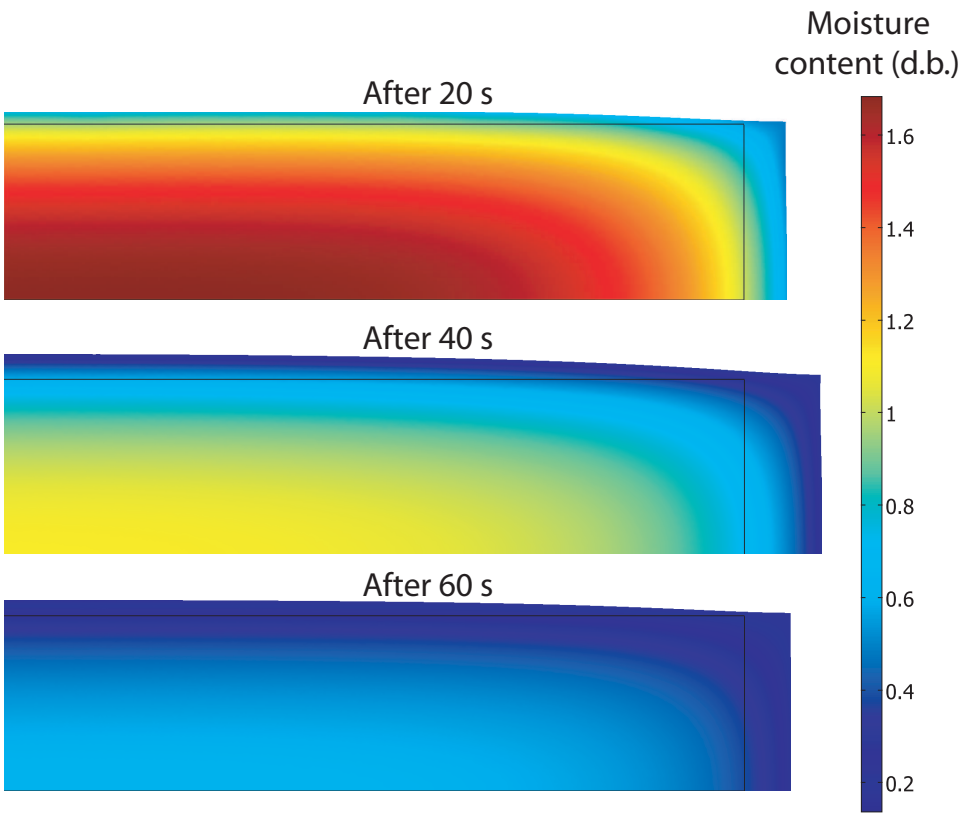

Figure 5.11: Computed moisture content inside the sample at different times during puffing. The initial moisture content of the sample was 1.7 db.

tion 5.26). Due to increase in the gas permeability the pressure decreases at a particular location. The pressure therefore remains bounded which may be one of the reasons that the material does not rupture during the process.

5.5.3 Sensitivity of the model to input parameters

With a large number of parameters needed in the complex model along with unavailability of accurate values for some of these parameters, it is necessary to quantify the model sensitivity to different parameters to have greater confidence in the predicted results. For example, the value of bulk modulus has not been measured for the material for the

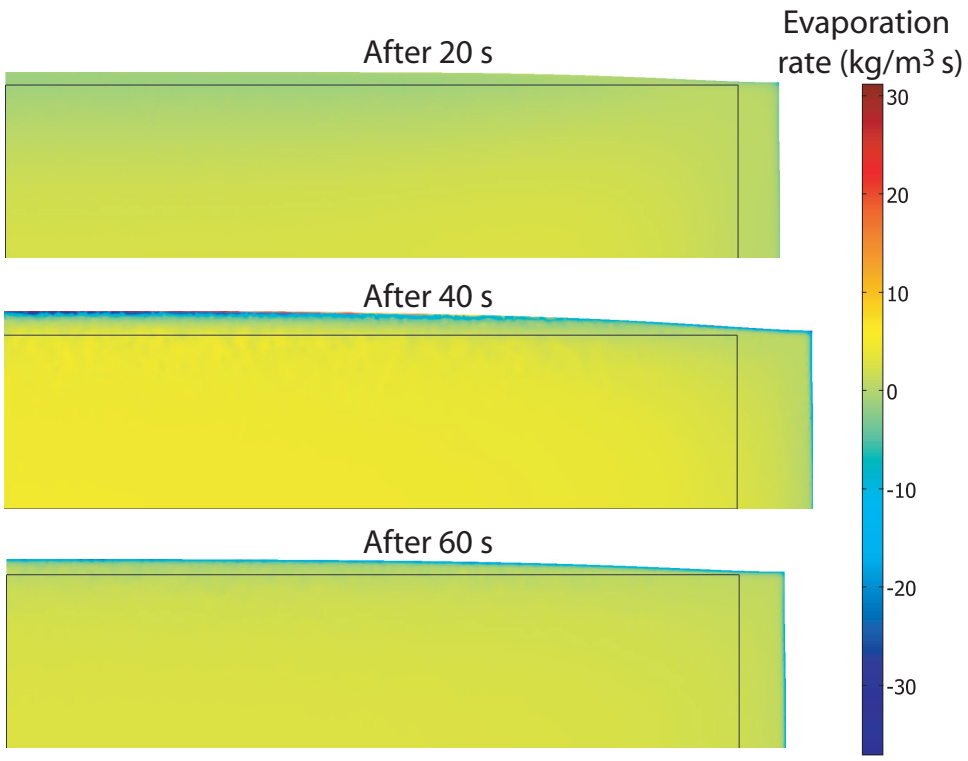

Figure 5.12: Computed evaporation rates inside the sample at different times during puffing. Positive values represent evaporation and negative values correspond to condensation. Evaporation occurs over the whole domain. At the surface, due to lower surrounding temperatures, some condensation is observed.

series of processes considered here, i.e., blanching followed by slow drying followed by intensive microwave heating. In order to look into the effect of change in these parameters values on the results, sensitivity analysis was done for two parameters whose accurate values were difficult to find in existing literature, bulk modulus and permeability of water and gas. For bulk modulus, a series of values were considered in the range of $\pm 20\%$ of the value used for the simulations in this paper. Permeability values were considered in the range of $\pm 50\%$ of the value used for the simulations. Moisture content and volume change histories, as affected by bulk modulus and permeability, were computed.

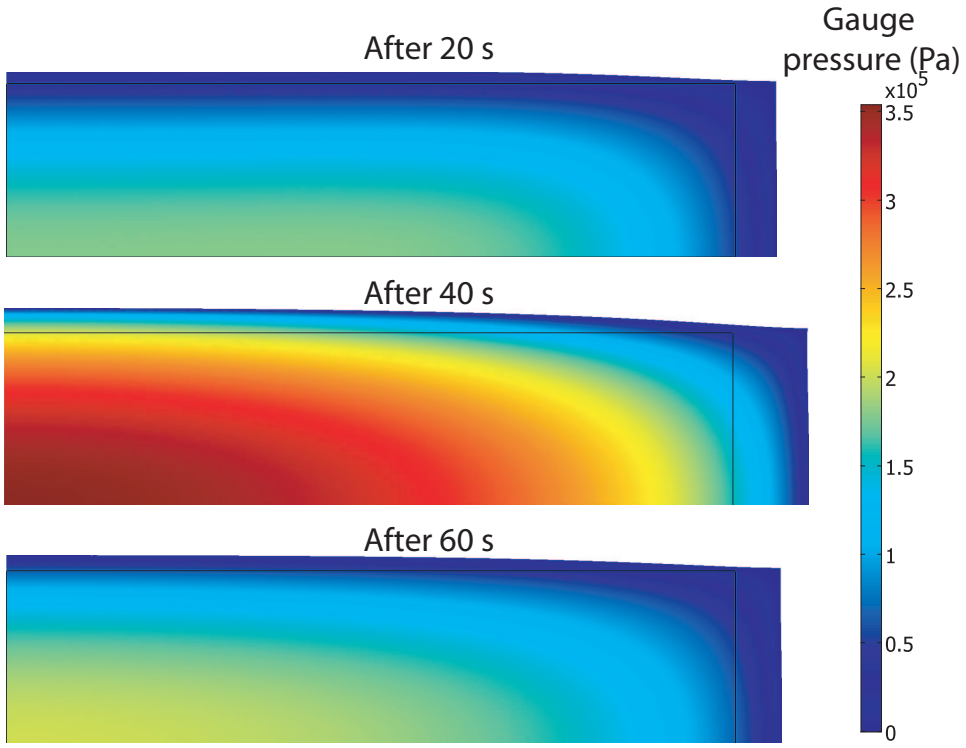

Figure 5.13: Computed gauge pressures inside the sample at different times during puffing. Highest pressures occur near the center of the material.

Bulk modulus

Four additional values of bulk modulus ($\pm 10\%$, $\pm 20\%$) were used to determine the sensitivity of the model to this parameter. The range of bulk modulus values used was estimated based on the literature data for potatoes undergoing intensive heating processes[49–52]. Moisture loss and volume change histories are plotted in Figure 5.15. The change in bulk modulus values do not affect the moisture loss predicted from the model at all as can be seen in Figure 5.15a. However, the volume change depends considerably on the value of bulk modulus. Lower values of bulk modulus represent softened tissues that are easier to deform and therefore the volume increase is maximum for the minimum bulk modulus value (at -20% of the original value). Deformation in the material causes change in porosity that can potentially affect the transport processes inside the

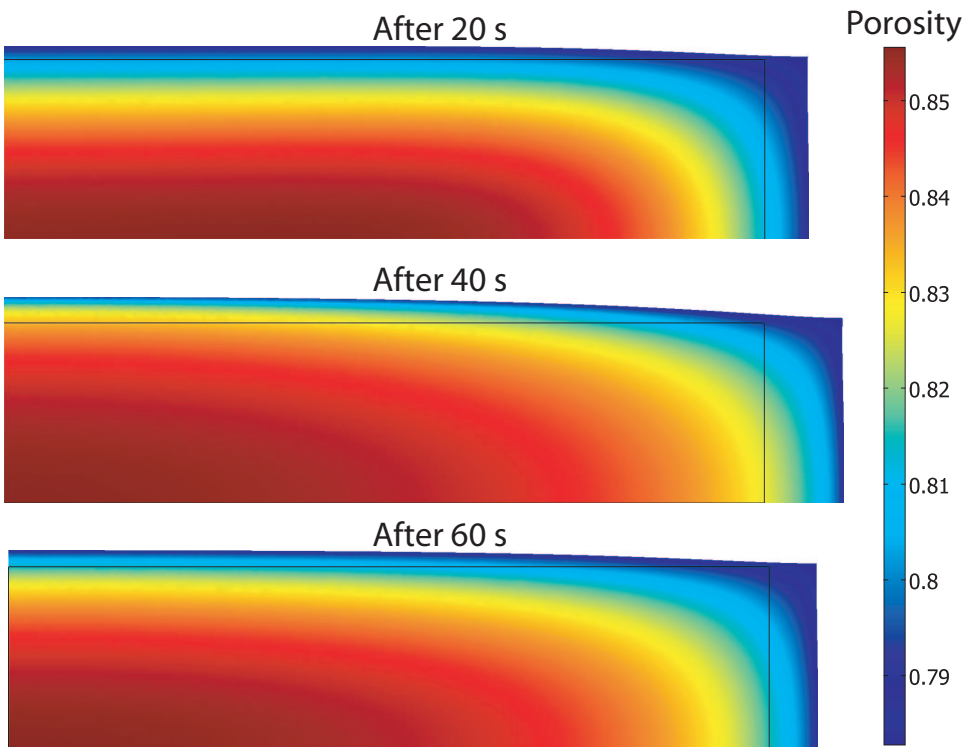

Figure 5.14: Computed change in porosity of the samples at different times during puffing. The initial porosity of the sample was 0.8. Note that this porosity only represents the change in volume of the material and it does not represent the loss of water.

medium. However, the changes in porosity are insignificant, with change of 0.44 and -0.33% for -20% and 20% increase in bulk modulus values, respectively. As a result, the transport inside the medium remains independent of the change in the bulk modulus value and the moisture loss is not affected.

Water and gas permeability

Measurement of permeabilities of biological materials is still not a standard technique and different literature sources have estimated a wide range of liquid and gas permeability values in potatoes[21,57,58]. The reported values vary by more than two orders of magnitude and these variations are so large that it is not feasible to incorporate them

(a)

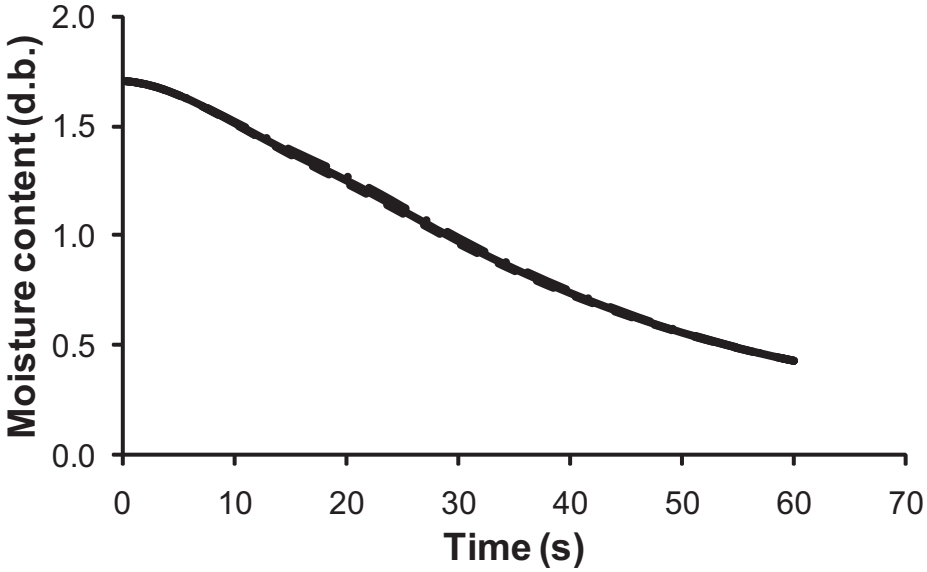

(b)

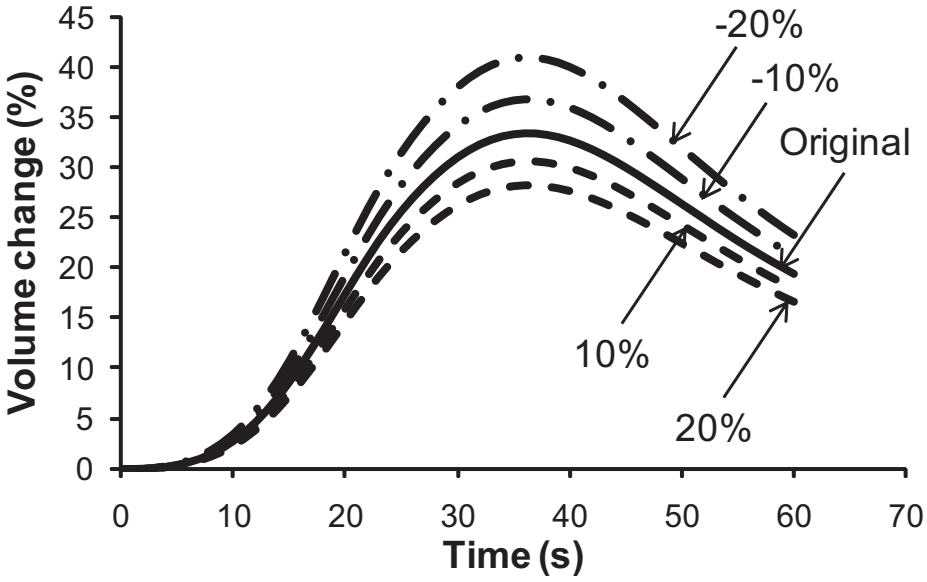

Figure 5.15: (a) Sensitivity of the process to change in bulk modulus using the total moisture loss as the variable of interest. The moisture loss history is plotted for 5 different values of bulk modulus: the original value (given in Table 5.1) and 10, 20, -10 and -20% of the original value. (b) Sensitivity to the bulk modulus value with total volume change as the variable.

in the sensitivity analysis study as they render the problem non-physical (without corresponding change in other parameter value, e.g., moisture content, porosity, etc.) and hence unsolvable. In order to account for the large variation, water and gas permeability values were considered in range of $\pm 50\%$ of the original value. The resulting change in moisture content and volume change of the material are plotted in Figure 5.16. Again it is found that the change in permeability values did not affect the total moisture loss as much but the volume change was influenced considerably. This is due to the drastic change in pressures inside the domain with change in permeability values. When gas permeability decreases, there is additional resistance to flow through the porous media (as given by Equation 5.3) and as a result, the pressures increase.

Uncertainty analysis

For estimating the uncertainty in volume prediction from the model due to the input parameters discussed above, an uncertainty analysis is carried out[59]. Keeping all other parameters fixed, the volume at a specific time can be a function of bulk modulus (K) and permeability (k):

$$V = f(K, k) \tag{5.27}$$

Here, the effect of both liquid and gas permeability is lumped into the variable k. The uncertainty in volume is therefore:

$$V \pm \Delta V = f(K \pm \Delta K, k \pm \Delta k) \tag{5.28}$$

where Δ is the uncertainty interval for the two parameters. Using a first order approximation we get,

$$V \pm \Delta V = f \pm \frac{\partial f}{\partial K}\Delta K \pm \frac{\partial f}{\partial k}\Delta k \tag{5.29}$$

To include the combined effect of all the uncertainties and to avoid inconsistencies due to plus or minus sign in the different uncertainties, a statistical approach is taken[60]. The

(a)

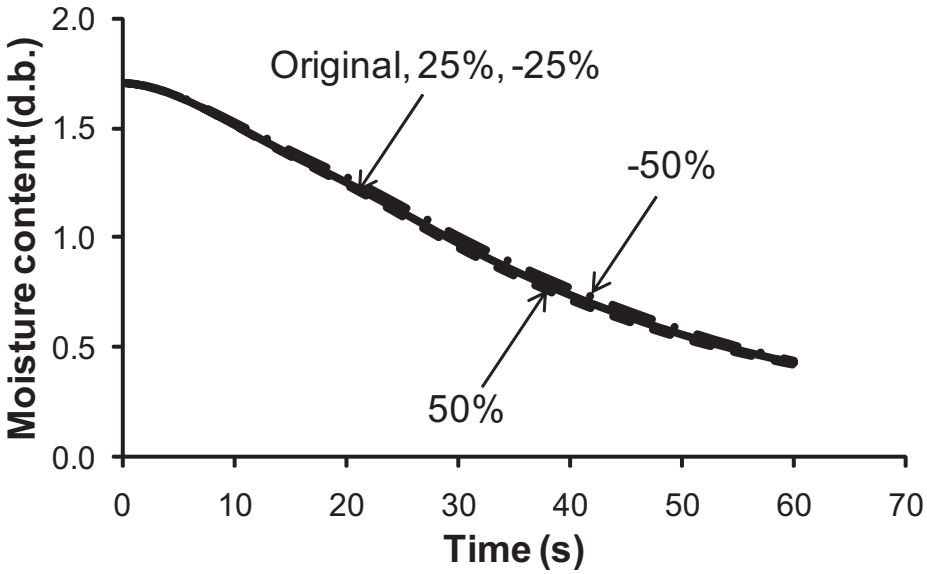

(b)

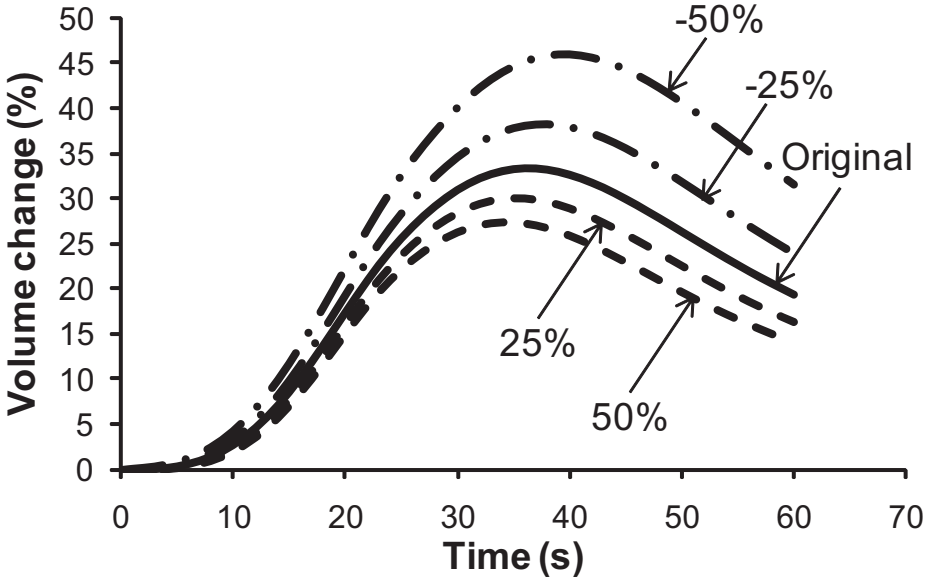

Figure 5.16: (a) Sensitivity of the process to change in liquid and gas permeabilities using the total moisture loss as the variable of interest. The moisture loss history is plotted for 5 different sets of permeabilities: the original set (given in Table 5.1) and 25, 50, -25 and -50% of the original set of values. (b) Sensitivity to liquid and gas permeabilities with the total volume change as the variable.

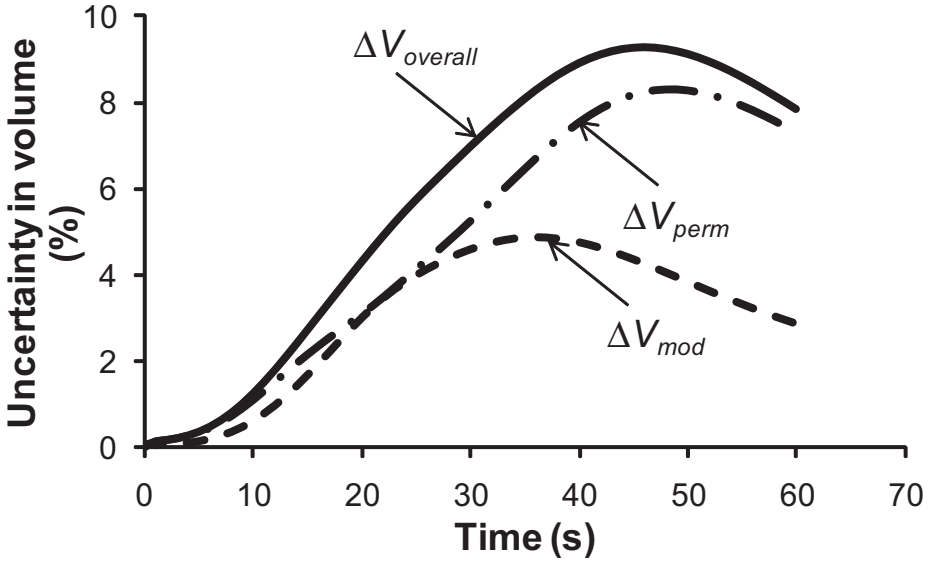

Figure 5.17: Uncertainty in volume change prediction from the model with time due to the variation in bulk modulus and permeability values. ΔV_{mod}, ΔV_{perm} and $\Delta V_{overall}$ represent percentage uncertainty due bulk modulus and permeability, and the overall uncertainty respectively.

total uncertainty is therefore defined as the square root of the sum of the errors squared:

$$\Delta V = \sqrt{\left(\frac{\partial f}{\partial K}\Delta K\right)^2 + \left(\frac{\partial f}{\partial k}\Delta k\right)^2} \tag{5.30}$$

The partial derivatives are calculated using a central differencing scheme, i.e., the derivatives are calculated using function values corresponding to the maximum and minimum values of the particular parameter. For example, for bulk modulus values:

$$\Delta V_K = \frac{\partial f}{\partial K}\Delta K \approx \frac{V_{K,\max} - V_{K,\min}}{2} \tag{5.31}$$

The percentage uncertainties plotted in Figure 5.17 are therefore defined as:

$$\Delta V_{\text{mod}} = \frac{\Delta V_K}{V_{org}} \times 100, \quad \Delta V_{perm} = \frac{\Delta V_k}{V_{org}} \times 100, \quad \Delta V_{overall} = \frac{\Delta V}{V_{org}} \times 100 \tag{5.32}$$

The overall uncertainty, in general, keeps increasing with the process time (Figure 5.17) reaching a maximum value of about 9% after 46 s. Uncertainty in the choice of permeability values affect the volume change more than the uncertainty in the bulk modulus

value chosen. The results from this uncertainty analysis basically shows that there may be large uncertainties in the volume change predicted by the model depending on the chosen input parameters values. Accordingly, in general uncertainty in the predictions must be considered while comparison with experimental data, e.g., in the volume change validation presented in Figure 5.8, it must be kept in mind that the predicted values can also be uncertain by as much as 9%.

5.6 Optimum conditions for puffing

The development of the comprehensive model provides us with a unique and exciting opportunity to look at the different factors that can affect the puffing process and thereby determine the optimum conditions for the process. In absence of sensory evaluation data, the quality parameters that are deemed to be important for the final product are the final moisture content and final volume. The effect of different processing conditions on these quality parameters is now studied. The different parameters that are considered are:

- Combination microwave heating
- Initial moisture content
- Sample size
- Relative humidity

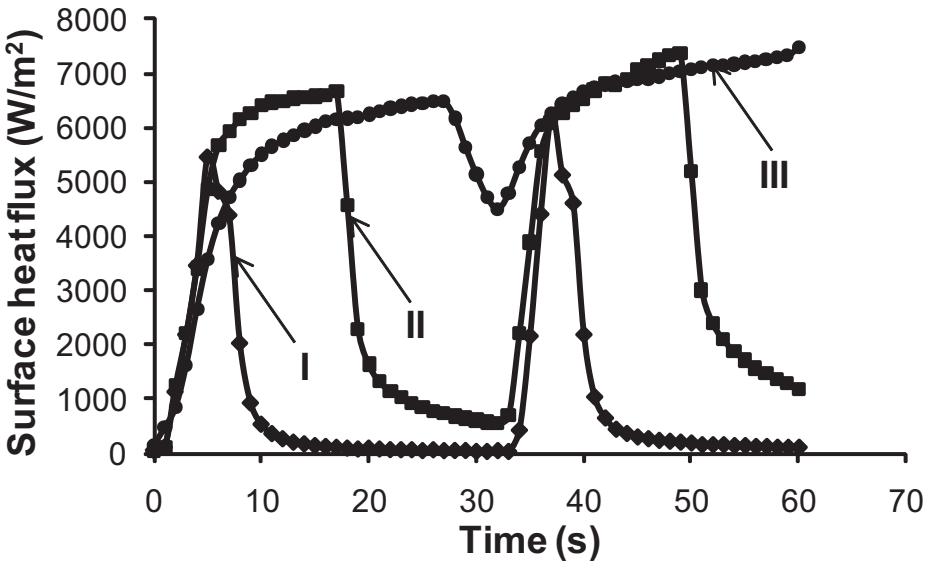

Figure 5.18: Surface heat fluxes corresponding to different power levels for infrared heating. The data that was measured using heat flux sensors is taken from literature[61].

5.6.1 Combination microwave heating

The effect of combining additional modes of heating such as infrared, hot air and forced hot air on puffing characteristics were determined using the model.

Infrared heating

Infrared heating was combined with microwaves for puffing the samples. Surface heat flux as a function of time due to infrared heating at different power levels measured using heat flux sensors were obtained from literature[61] for a particular oven (GE Advantium Oven, General Electric Company, Louisville, KY). The fluxes (plotted in Figure 5.18) were included as boundary conditions on the open surface of the sample. The total moisture loss and volume change were determined for the different cases (plotted in Figure 5.19). With increase in infrared power, the final volume was found to increase

(a)

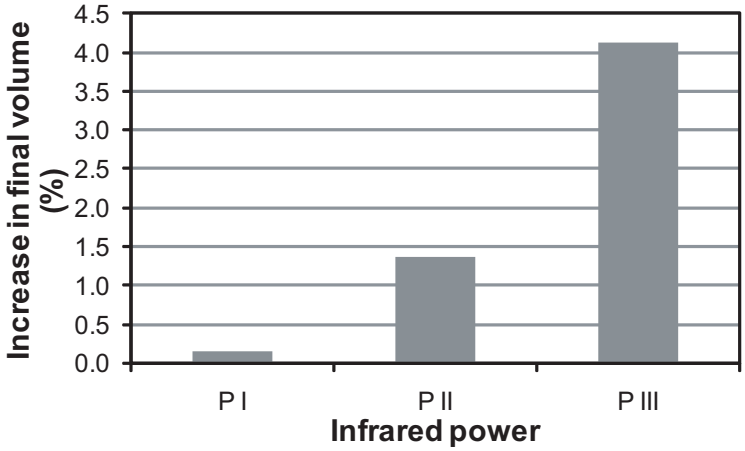

(b)

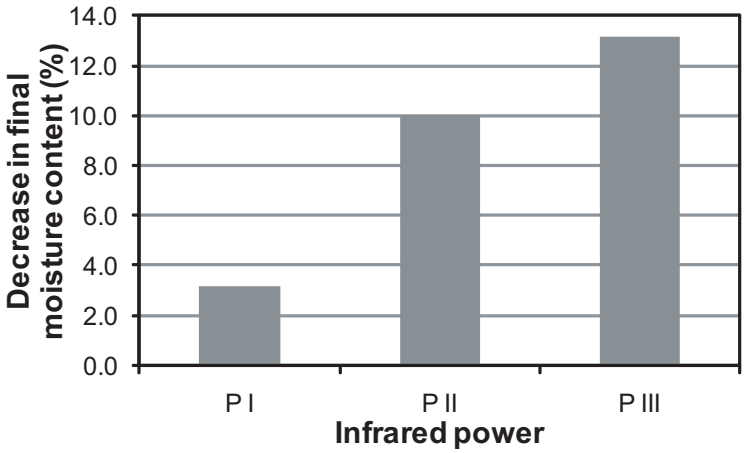

Figure 5.19: Change in puffing characteristics on addition of infrared heating. The different power levels are plotted in Figure 5.18. Addition of infrared heating increases the final product volume and decreases its moisture content and may therefore lead to a better quality puffed product. The percentages are calculated based on the value of final moisture content and volume for the sample puffed without infrared heating (original case).

and the final moisture content decreased (Figure 5.19). There is a decrease in moisture content by 3.1 to 13.2% depending on the infrared power level compared to the sample puffed using microwaves only. Infrared provides a constant source of additional surface heating that causes increased evaporation and loss of moisture. Most of the additional moisture loss is in the form of liquid water at the surface that is first evaporated and then escapes as vapor. The increased vapor formation when infrared heating is added also increases pressures[62] which in turn leads to increase in the volume of the product. The volume increase compared to microwave only heating is 4.1% for the highest infrared power level. Increased volume and decreased moisture content of the final product are both desired during puffing. The final volume relates directly to the texture and crispiness of the product and almost all past studies on puffing of different materials[1] including potatoes[6,56] and cereals[12] have used volume change as an index of puffing. Lower moisture can potentially reduce the microbial activity for a shelf stable product. Therefore, infrared addition to microwave puffing may lead to a better quality product.

Hot air heating

The effect of addition of hot air to microwave for puffing was studied. Almost all previous work on puffing used only hot air heating for the puffing process and as expected the hot air temperature was deemed to be an important factor affecting puffing[10,11]. Four different air temperatures were considered: 22, 100, 120 and 140°C. It was assumed that the change in airflow was insignificant and therefore the same heat transfer coefficient of 20 W/m^2K was used for the simulations. There was no appreciable change in the volume of the puffed product on addition of the hot air heating mode (Figure 5.20a). Hot air heating at the surface does not change the pressure distribution in the interior as much; as a result the structural changes are insignificant. However, moisture loss was

found to be 4.7% to 6.7% more compared to the sample puffed at room temperature (Figure 5.20b). This is due to ease of removal for moisture from the surface of the sample by evaporation as a result of the high temperatures. Hot air can therefore be used in addition to microwaves to reduce the final moisture content of the puffed product. However these changes are not as significant compared to addition of infrared since the surface heat flux due to hot air heating decreases as the surface temperature increases with time.

Hot air and forced convection

Puffing was carried out by combining microwaves with hot air flowing at different velocities. The hot air velocity inside the oven can be controlled by using fans in the oven whose direction of rotation can be controlled[63] (e.g. GE Profile oven, Model no. JT930BHBB, GE, Inc., Louisville, KY) or by using impingement of air jet[64] on the sample surface (e.g. Thermador JetDirect oven, Model CJ302UB, Enersyst Development Center, Dallas, TX). A moderate air temperature of 60°C was considered. Three different heat transfer coefficients that were used for the simulations were 25, 30 and 35 W/m^{2}K. The corresponding mass transfer coefficient obtained using Lewis number analogy were 0.017, 0.021 and 0.024 m/s respectively. For the original case, air temperature was 22°C, heat transfer coefficient was 20 W/m^{2}K and mass transfer coefficient was 0.011 m/s. In this case, although there was appreciable decrease in moisture, in the range of 5.4 to 8.7%, with increase in heat transfer coefficient (Figure 5.21b), the volume of the puffed product decreased by 3.3 to 5.2% compared to the volume obtained using microwave only puffing. Moisture loss as expected is more as there is increased surface evaporation due to the higher heat transfer coefficient as well as increased removal of liquid water as well as vapor due to the higher mass transfer coefficient. However, as

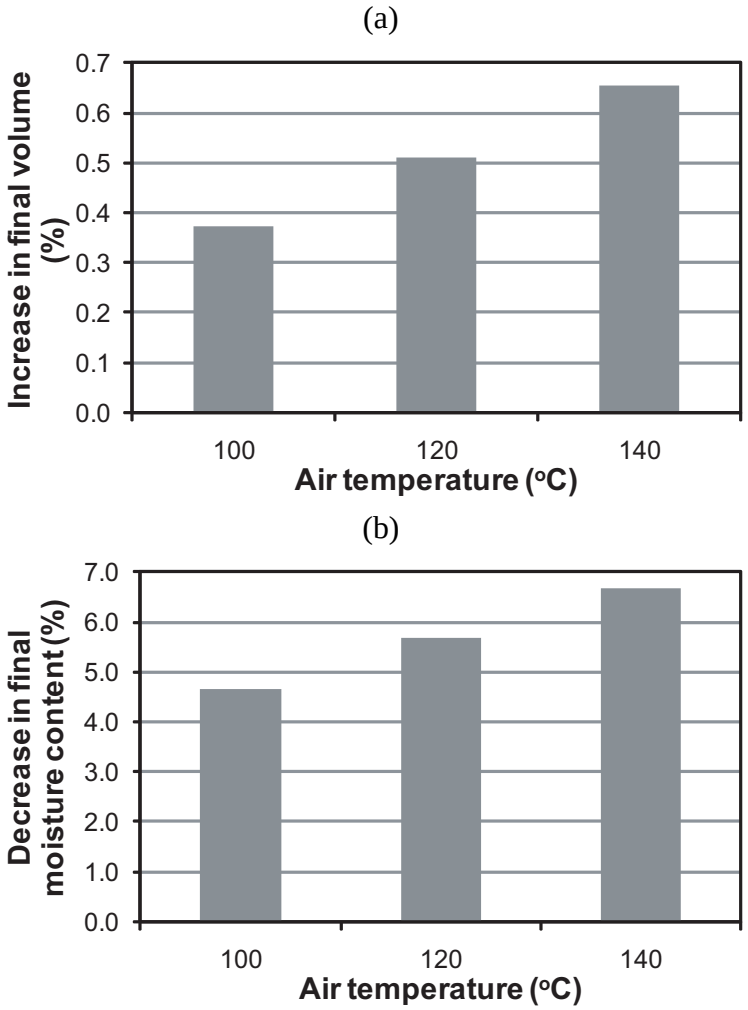

Figure 5.20: Change in puffing characteristics when the sample is heated with application of hot air on the surface along with the microwaves. Hot air used in addition to microwave heating can help reduce the final moisture content of the puffed product; although the change is not as significant compared to addition of infrared. The percentages are calculated based on the value of final moisture content and volume for the sample puffed at room temperature (original case).

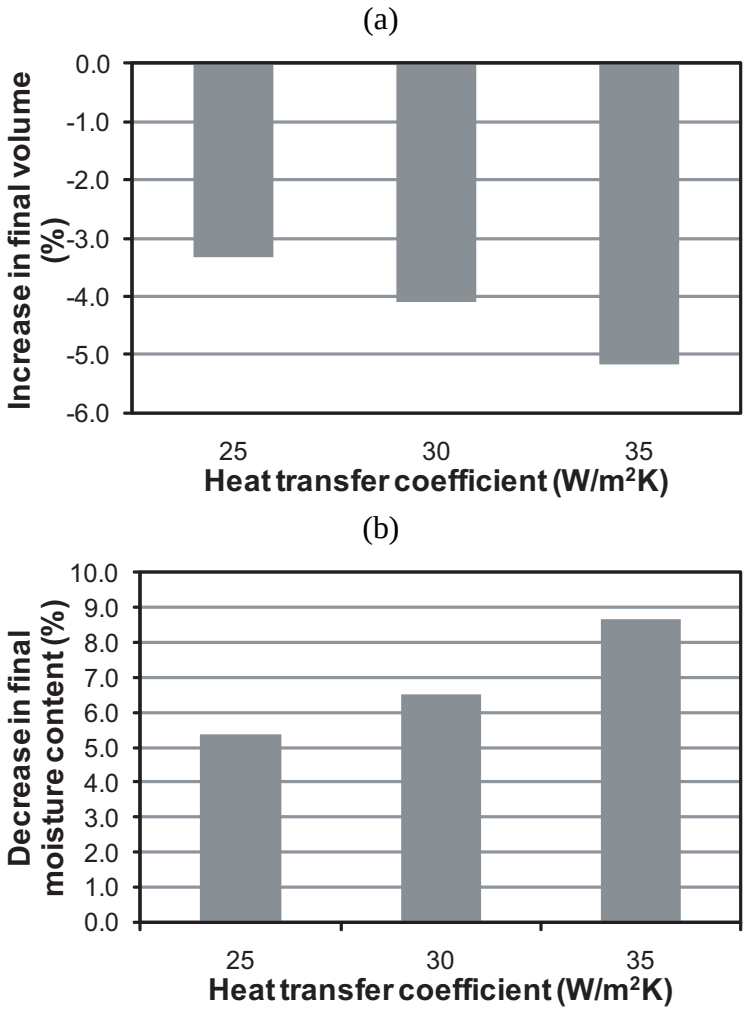

Figure 5.21: Change in puffing characteristics with addition of hot air at 60°C at different velocities on the surface. Puffing carried out under forced air convection may lead to decreased volume products. The percentages are calculated based on the value of final moisture content and volume for the original case where the heat transfer coefficient was 20 W/m^{2}K.

moisture is lost as vapor, the pressure inside the domain decreases which results in decrease of the volume as the pressures are unable to puff the sample as much. Decrease in volume of puffed product with the use of higher air velocity of puffing was also reported in an experimental study[6] for puffing of rehydrated potato flour.

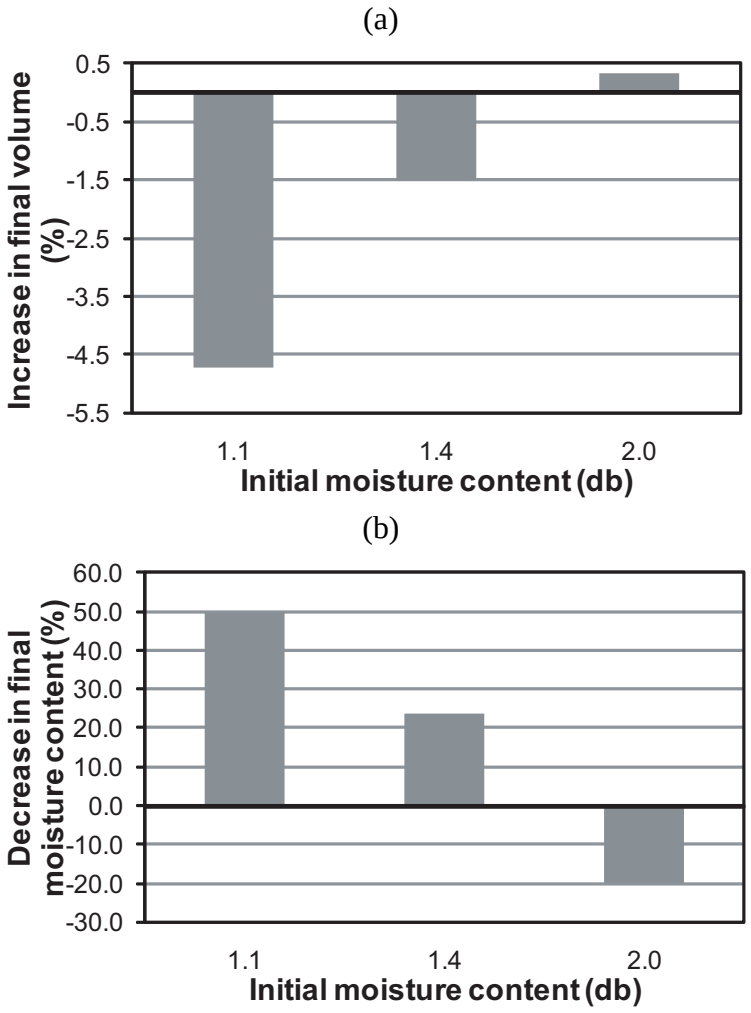

Figure 5.22: Change in puffing characteristics with the initial moisture content of the samples. An initial moisture content near 1.4 db may be optimum for puffing. The percentages are calculated based on the value of final moisture content and volume for the sample with initial moisture content of 1.7 db (original case).

5.6.2 Initial moisture content

One of the most important variables that must be studied for the success of the puffing process is the initial moisture content of the sample[8,56]. The moisture content should be optimum, since if it is too high, the formation of vapor becomes difficult as greater energy is required for evaporation. This effect was also discussed previously[6]. On the other hand if there is too little liquid water to begin with the sample may become

almost completely dry much before the end of the puffing process[56]. The initial moisture content of the sample can be controlled by controlling the oven temperature and time during drying step. Four different initial moisture content values were considered for the simulations: 1.1, 1.4, 1.7 and 2.0 db. The volume change in the samples was not appreciable in the initial moisture content range considered (Figure 5.22a). The final volume of the driest sample was 4.7% less and for the sample at 1.4 db about 1.5% less compared to the original sample at 1.7 db. However there was a drastic increase in moisture loss for the drier samples ($\sim$24-50%) compared to the sample at 1.7 db which is desirable during puffing as discussed earlier. Therefore an initial moisture content near 1.4 db may be optimum for puffing.

5.6.3 Sample size

The effect of the sample size on the puffing characteristics was studied. Samples of different thicknesses were considered: 2, 4 and 6 mm. The thickness of the original sample was 8 mm. Since the initial volumes of the samples were different, in order to compare the final product obtained from the different samples, the volume change with respect to initial volume of each sample in percentage was calculated and plotted as shown in Figure 5.23a. It was found that volume change was the maximum for the 8 mm sample. The thinnest sample showed almost no volume change ($\sim$ 0.1%) for the given set of puffing conditions. Since thinner slices may be more desirable for consumption by the consumer, puffing conditions would have to be drastically changed. This may involve starting with a higher moisture content, or using a much higher power for microwaves, or possible addition of infrared heating. As thickness decreased, it was also found that moisture content decreased drastically which is desirable (Figure 5.23b). The transport domain becomes much smaller which the thickness and moisture from the

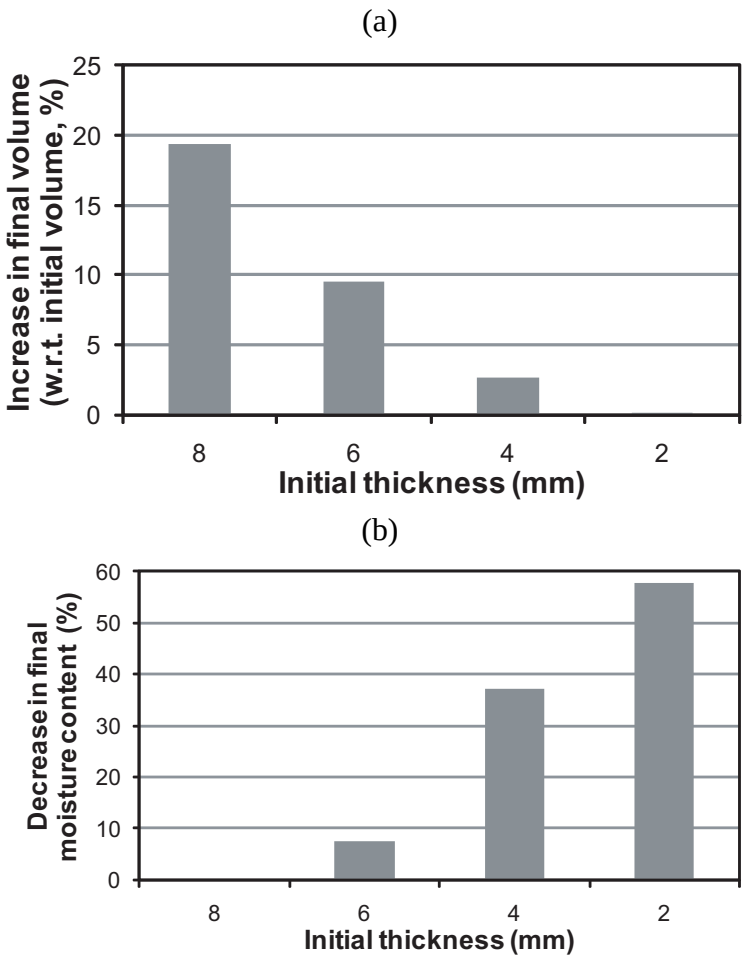

Figure 5.23: Change in puffing characteristics with the initial thickness of the samples. The thinnest sample (2 mm thick) showed almost no volume change after puffing. Volume change percentage is calculated with respect to initial volume of each sample. Final moisture change percentage is calculated based on the value of final moisture content for the 8 mm thick sample (original case).

interior is able to move faster to the surface from where it is removed.

5.6.4 Relative humidity

Finally the effect of relative humidity of the surrounding air on the puffing characteristics of the sample was studied. Relative humidity (RH) is defined as

$$RH = \frac{p_{v,\,amb}}{p_{sat}} \times 100\% \tag{5.33}$$

where $p_{v,\,amb}$ is the vapor pressure of water in air and p_{sat} is the vapor pressure of pure water at the same temperature. To incorporate the effect of RH in the model, the $\rho_{v,\,oven}$ terms in boundary condition equations (Equations 5.17-5.19) were written as functions of RH, saturation pressure and temperature,

$$\rho_{v,\,oven} = \frac{p_{v,\,amb} M_v}{R T_{amb}} = \left[\frac{p_{sat} RH}{100}\right] \frac{M_v}{R T_{amb}} \tag{5.34}$$

Four different RH values were considered: 40, 60, 80 and 100%. The original case was run for a RH of 0. The final moisture content and volume for the different RH values are shown in Figure 5.24. The maximum volume increase was an insignificant 0.5% for a RH of 100% compared to the sample puffed at 0 RH. The corresponding moisture loss change was only 0.7%. It can therefore be concluded that RH does not an any appreciable effect on the puffing characteristics.

5.7 Summary and Conclusions

A fully coupled model for multiphase transport and large deformation during microwave puffing of a hygroscopic porous material was formulated, solved using a finite element based software and validated using experimental measurements. A comprehensive understanding of the different phenomena such as evaporation/condensation, pressure development, deformation and their relationships with heating rates and transport parameters was developed. Such a detailed model is essential in order to understand a complex

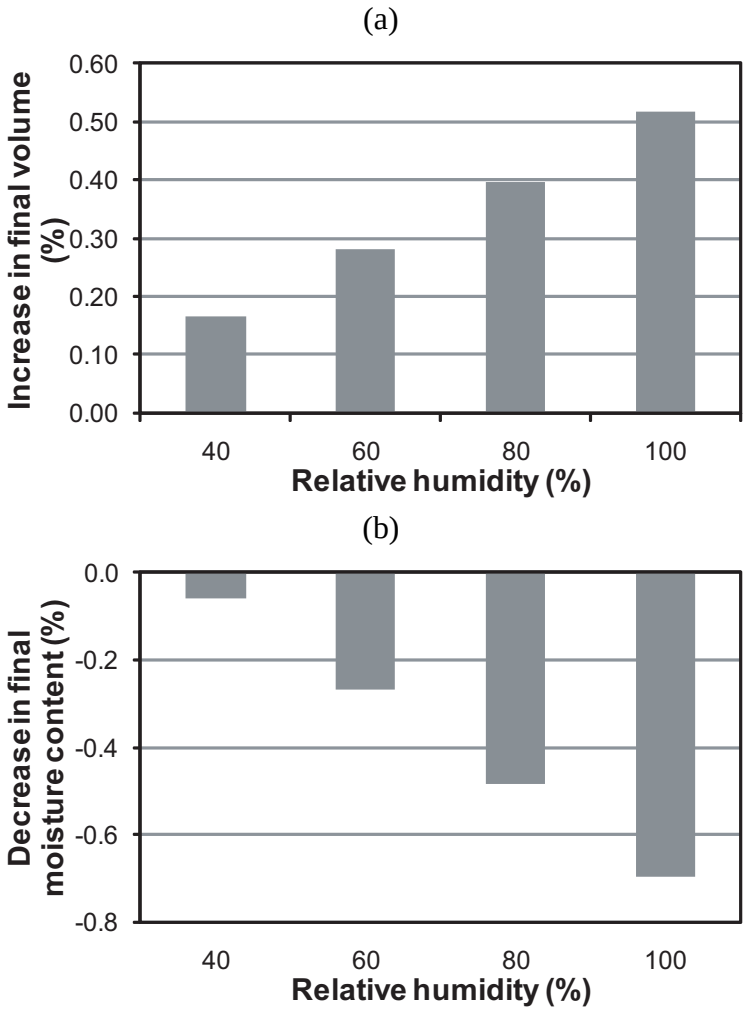

Figure 5.24: Change in puffing characteristics with the relative humidity of the surrounding air. The RH of the air does not affect the puffing process significantly. The percentages are calculated based on the value of final moisture content and volume for the sample puffed at 0 RH (original case).

process such as puffing and has not been implemented earlier. Often drawbacks of such complex models are the availability of accurate input parameters. To address this issue, detailed uncertainty analysis was carried out. Once the model was developed and validated, it provided us with a unique and exciting opportunity to take a detailed look at factors affecting the puffing process and thus determine the optimum conditions for the process.

The major conclusions from the work are summarized as follows. (1) The model accurately predicts the different variables during the puffing process as measured in this work and also reported earlier by others. (2) Very high temperatures are required to generate pressures needed to puff the material. The process may not be successful unless carried out using an intensive heating source such as microwaves. (3) Although pressures increase due to intensive microwave heating, they remain bounded due to a complex feedback mechanism that includes change in porosity and permeability of the material with puffing time. (4) Moisture loss was found to be largely independent of the change in input parameters such as bulk modulus and liquid and gas permeabilities. (5) Uncertainty in the choice of permeability values affect the volume change more than the uncertainty in the bulk modulus value chosen.(6) Infrared addition to microwave puffing increases the final product volume and decreases its moisture content and may therefore lead to a better quality product. (7) Hot air can be used in addition to microwaves to reduce the final moisture content of the puffed product; although the change is not as significant compared to addition of infrared. (8) Heating of sample using forced air convection may lead to decreased volume products. (9) An initial moisture content near 1.4 db may be optimum for puffing. (10) Thinner samples showed almost no volume change after puffing. Puffing conditions may need to be drastically changed from the method proposed in this study for successful puffing of thin samples. (11) Relative humidity of the surroundings had no effect on the puffing characteristics.

5.8 Acknowledgements

This project was supported by National Research Initiative Grant from the USDA Cooperative State Research, Education, and Extension Service Competitive Grants program.

Nomenclature

Symbol	Description and unit
c	concentration, kg m^{-3}
c_p	specific heat capacity, J $kg^{-1}K^{-1}$
C	molar density, kmol m^{-3}
$D_{eff,g}$	effective gas diffusivity, m^2s^{-1}
D	capillary diffusivity, m^2s^{-1}
E	Green-Lagrange strain tensor
F	deformation gradient tensor
G	shear modulus, Pa
h	heat transfer coefficient, W $m^{-2}K^{-1}$
h_m	mass transfer coefficient of vapor, ms^{-1}
$\dot{I}$	volumetric evaporation rate, $kgm^{-3}s^{-1}$
j	total mass flux, kg $m^{-2}s^{-1}$
J	Jacobian of deformation gradient tensor, Pa
k^{th}	thermal conductivity, $Wm^{-2}K^{-1}$
k	intrinsic permeability, m^2
k_r	relative permeability
K	bulk modulus, Pa
K_{evap}	non-equilibrium evaporation constant
m	overall mass fraction
M	moisture content, db
M_a, M_v	molecular weight of air and vapor
n	normal direction
P, p	total pressure and partial pressure, respectively, Pa
q	heat flux, W m^{-2}
Q_{mic}	microwave source term, $Jm^{-3}s^{-1}$
R	universal gas constant, J $kmol^{-1}$ K^{-1}
S	saturation
S	second Piola Kirchhoff stress tensor, Pa
t	time, s
T	Temperature, °C
v	velocity, m s^{-1}
V	volume, m^3
W	stored energy function, Pa
$x,\ y,\ z$	coordinates (Eulerian frame), m
$X,\ Y,\ Z$	coordinates (Lagrangian frame), m
Greek Symbols	
ρ	density, kg m^{-3}
λ	latent heat of vaporization, J kg^{-1}
ω_a, ω_v	mass fraction of vapor and air with respect to total gas
ϕ	porosity
μ	dynamic viscosity, Pa s
σ	Cauchy stress tensor, Pa

BIBLIOGRAPHY

[1] Payne FA, Taraba JL, Saputra D. Review of puffing processes for expansion of biological products. *Journal of Food Engineering*. 1989;10(3):183-197.

[2] McAlister RE. Microwave puffing of cereal grain and products made therefrom. 1972; U.S. Patent 3682651.

[3] Krysiak DLM, Allen PE, Kirihara TT. Laminated multi-layered cereal products and methods of preparation. 2004;U.S. Patent 6746707.

[4] Varnalis AI, Brennan JG, MacDougall DB. Proposed mechanism of high-temperature puffing of potato. Part I. The influence of blanching and drying conditions on the volume of puffed cubes. *Journal of Food Engineering*. 2001;48(4):361-367.

[5] Wu PJ, Schwartzberg HG. Popping Behavior and Zein Coating of Popcorn. *Cereal Chemistry*. 1992;69(5):567-573.

[6] Nath A, Chattopadhyay PK, Majumdar GC. High temperature short time air puffed ready-to-eat (RTE) potato snacks: Process parameter optimization.*Journal of Food Engineering*. 2007;80:770-780.

[7] Chandrasekhar PR, Chattopadhyay PK. Rice puffing in relation to its varietal characteristics and processing conditions. *Journal of Food Process Engineering*. 1991;14(4):261-277.

[8] Hoke K, Housova J, Houska M. Optimum conditions of rice puffing. *Czech Journal of Food Sciences*. 2005;23(1):1-11.

[9] Saputra D, Payne FA, Cornelius PL. Puffing dehydrated green bell peppers with carbon dioxide. *Transactions of the ASAE*. 1991;34(2):475-480.

[10] Nath A, Chattopadhyay PK. Effect of process parameters and soy flour concentration on quality attributes and microstructural changes in ready-to-eat potato-so snack

using high-temperature short time air puffing. *LWT-Food Science and Technology*. 2008;41(4):707-715.

[11] Antonio GC, Alves DG, Azoubel PM, Murr FEX, Park KJ. Influence of osmotic dehydration and high temperature short time processes on dried sweet potato (Ipomoea batatas Lam.). *Journal of Food Engineering*. 2008;84(3):375-382.

[12] Mariotti M, Alamprese C, Pagani MA, Lucisano M. Effect of puffing on ultrastructure and physical characteristics of cereal grains and flours. *Journal of Cereal Science*. 2006;43(1):47-56.

[13] Tabeidie Z, Payne FA, Cornelius PL. Puffing potato pieces with CO2. *Transactions of the ASAE*. 1992;35(6):1935-1940.

[14] Zapotoczny P, Markowski M, Majewska K, Ratajski A, Konopko H. Effect of temperature on the physical, functional, and mechanical characteristics of hot-air-puffed amaranth seeds. *Journal of Food Engineering*. 2006;76(4):469-476.

[15] Schwartzberg HG, Wu JPC, Nussinovitch A, Mugerwa J. Modelling deformation and flow during vapor-induced puffing. *Journal of Food Engineering*. 1995;25(3):329.

[16] Chiotellis E, Campbell GM. Proving of bread dough I - Modelling the evolution of the bubble size distribution. *Food and Bioproducts Processing*. 2003;81(C3):194-206.

[17] Fan JT, Mitchell JR, Blanshard JMV. A model for the oven rise of dough during baking. *Journal of Food Engineering*. 1999;41(2):69-77.

[18] Alavi SH, Rizvi SSH, Harriott P. Process dynamics of starch-based microcellular foams produced by supercritical fluid extrusion. I: model development. *Food Research International*. 2003;36(4):309-319.

[19] Wang LJ, Ganjyal GM, Jones DD, Weller CL, Hanna MA. Modeling of bubble growth dynamics and nonisothermal expansion in starch-based foams during extrusion. *Advances in Polymer Technology*. 2005;24(1):29-45.

[20] Halder A, Dhall A, Datta AK. An improved, easily implementable, porous media based model for deep-fat frying - Part I: Model development and input parameters. *Food and Bioproducts Processing*. 2007;85(C3):209-219.

[21] Ni H, Datta AK, Torrance KE. Moisture transport in intensive microwave heating of biomaterials: a multiphase porous media model. *International Journal of Heat and Mass Transfer*. 1999;42(8):1501-1512.

[22] Yamsaengsung R, Moreira RG. Modeling the transport phenomena and structural changes during deep fat frying - Part 1: model development. *Journal of Food Engineering*. 2002;53(1):1-10.

[23] Turner IW, Perre P. Vacuum drying of wood with radiative heating: II. Comparison between theory and experiment. *AIChE Journal*. 2004;50(1):108-118.

[24] Shi X, Datta AK, Mukherjee Y. Thermal stresses from large volumetric expansion during freezing of biomaterials. *Journal of Biomechanical Engineering-Transactions of the ASME*. 1998;120(6):720-726.

[25] Baek S, Wells PB, Rajagopal KR, Humphrey JD. Heat-induced changes in the finite strain viscoelastic behavior of a collaagenous tissue. *Journal of Biomechanical Engineering-Transactions of the ASME*. 2005;127(4):580-586.

[26] Niamnuy C, Devahastin S, Soponronnarit S, Raghavan GSV. Modeling coupled transport phenomena and mechanical deformation of shrimp during drying in a jet spouted bed dryer. *Chemical Engineering Science*. 2008;63(22):5503-5512.

[27] Ressing H, Ressing M, Durance T. Modeling the mechanisms of dough puffing

during vacuum microwave drying using the finite element method. *Journal of Food Engineering*. 2007;82(4):498-508.

[28] Minkoff SE, Kridler NM. A comparison of adaptive time stepping methods for coupled flow and deformation modeling. *Applied Mathematical Modelling*. 2006;30(9):993-1009.

[29] Itaya Y, Kobayashi T, Hayakawa KI. 3-Dimensional Heat and Moisture Transfer with Viscoelastic Strain-Stress Formation in Composite Food during Drying. *International Journal of Heat and Mass Transfer*. 1995;38(7):1173-1185.

[30] Irudayaraj J, Haghighi K. Stress-Analysis of Viscoelastic Materials during Drying .1. Theory and Finite-Element Formulation. *Drying Technology*. 1993;11(5):901-927.

[31] Perre P, Turner IW, Passard J. 2-D solution for drying with internal vaporization of anisotropic media. *AIChE Journal*. 1999;45(1):13-26.

[32] Yang DQ, Rahardjo H, Leong EC, Choa V. Coupled model for heat, moisture, air flow, and deformation problems in unsaturated soils. *Journal of Engineering Mechanics-Asce*. 1998;124(12):1331-1338.

[33] Mayor L, Sereno AM. Modelling shrinkage during convective drying of food materials: a review. *Journal of Food Engineering*. 2004;61(3):373-386.

[34] Di Y, Yang J, Sato T. An operator-split ALE model for large deformation analysis of geomaterials. *International Journal for Numerical and Analytical Methods in Geomechanics*. 2007;31(12):1375-1399.

[35] Bollada PC. Expansion of elastic bodies with application in the bread industry. *Mathematical and Computer Modelling*. 2008;48(7-8):1055-1067.

[36] Khalili N. Two-phase fluid flow through fractured porous media with deformable matrix. *Water Resources Research*. 2008;44:-.

[37] Chao L, Borja RI, Regueiro RA. Dynamics of porous media at finite strain. *Computer Methods in Applied Mechanics and Engineering*. 2004;193(36-38):3837-3870.

[38] Zhang J, Datta AK, Mukherjee S. Transport processes and large deformation during baking of bread. *AIChE Journal*. 2005;51(9):2569-2580.

[39] Liang S, Yin JY, Xue SF. The ALE Method for Oil/Water Two-Phase Flow in Deforming Porous Media. *Journal of Canadian Petroleum Technology*. 2009;48(4):72-77.

[40] Biot MA. Mechanics of incremental deformations, John Wiley & Sons Inc, New York, New York. 1965.

[41] Lewis RW, Schrefler BA, The Finite Element Method in the Deformation and Consolidation of Porous Media, John Wiley & Sons Ltd, West Sussex, England. 1987.

[42] Coussy O. Poromechanics, John Wiley & Sons Ltd, West Sussex, England. 2004.

[43] Belytschko T, Liu WK, Moran B. Nonlinear Finite Elements for Continua and Structures, John Wiley & Sons Ltd, West Sussex, England. 2001.

[44] Donea J, Huerta A, Ponthot JP, Rodríguez-Ferran. Arbitrary Lagrangian-Eulerian Methods. In Encyclopedia of Computational Mechanics Volume 1, Eds. Stein E, Borst RD, Hughes TJR, John Wiley & Sons Ltd, West Sussex, England. 2004.

[45] Bear J. Dynamics of Fluids in Porous Media, Dover Publications Inc, New York, NY. 1972.

[46] Datta AK. Porous media approaches to studying simultaneous heat and mass transfer in food processes. I: Problem formulations. *Journal of Food Engineering*. 2007;80(1):80-95.

[47] Simo JC, Hughes TJR. Computational Inelasticity, Springer-Verlag Inc, New York, NY. 1998.

[48] Jarvis MC, Mackenzie E, Duncan HJ. The Textural Analysis of Cooked Potato .2. Swelling Pressure of Starch during Gelatinization. *Potato Research*. 1992;35(2):93-102.

[49] Solomon WK, Jindal VK. Relationship between texture of raw and cooked potatoes. *Journal of Texture Studies*. 2005;36(5-6):589-604.

[50] Krokida MK, Maroulis ZB. The effect of drying methods on viscoelastic behaviour of dehydrated fruits and vegetables. *International Journal of Food Science and Technology*. 2000;35(4):391-400.

[51] Alvarez MD, Canet W. Kinetics of thermal softening of potato tissue heated by different methods. *European Food Research and Technology*. 2001;212(4):454-464.

[52] Blaszczak W, Sadowska J, Fornal J, Vacek J, Flis B, Zagorski-Ostoja W. Influence of cooking and microwave heating on microstructure and mechanical properties of transgenic potatoes. *Nahrung-Food*. 2004;48(3):169-176.

[53] Buffler CR. Microwave Cooking and Processing: Engineering Fundamentals for the Food Scientist. Van Nostrand Reinhold, New York. 1993:4-31, 157-159

[54] Zhang H, Datta AK. Microwave power absorption in single- and multiple-item foods. *Food and Bioproducts Processing*. 2003;81(C3):257-265.

[55] AACC. *Approved methods of the AACC. Method 74-09.* American Association of Cereal Chemists, St. Paul, MN. 1988.

[56] Varnalis AI, Brennan JG, MacDougall DB, Gilmour SG. Optimisation of high temperature puffing of potato cubes using response surface methodology. *Journal of Food Engineering*. 2004;61(2):153-163.

[57] Datta AK. Hydraulic permeability of food tissues. *International Journal Of Food Properties*. 2006;9(4):767-780.

[58] Ni H, Datta AK. Heat and moisture transfer in baking of potato slabs. *Drying Technology*. 1999;17(10):2069-2092.

[59] Rabin Y. A general model for the propagation of uncertainty in measurements into heat transfer simulations and its application to cryosurgery. *Cryobiology*. 2003;46(2):109-120.

[60] Holman JP. Experimental Methods for Engineers, Seventh Edition, McGraw-Hill, New York. 2001.

[61] Dhall A, Datta AK, Torrance KE, Almeida MF. Radiative heat exchange modeling inside an oven. *AIChE Journal*. 2009;55(9):2448-2460.

[62] Datta AK, Ni H. Infrared and hot-air assisted microwave heating of foods for control of surface moisture. *Journal of Food Engineering*. 2002;51:355-364.

[63] Rakesh V, Datta AK, Amin MHG, Hall LD. Heating Uniformity and Rates in a Domestic Microwave Combination Oven. *Journal of Food Process Engineering*. 2009;32(3):398-424.

[64] Geedipalli S, Datta AK, Rakesh V. Heat transfer in a combination microwave-jet impingement oven. *Food and Bioproducts Processing*. 2008;86(C1):53-63.

[65] Choi Y, Okos MR. Thermal properties of liquid foods review, in Physical and Chemical Properties of Food, Okos MR (editor). American Society of Agricultural Engineers, St Joseph, MI. 1986: 35-77.

[66] Ratti C, Crapiste GH, Rotstein E. A New Water Sorption Equilibrium Expression for Solid Foods Based on Thermodynamic Considerations. *Journal of Food Science*. 1989;54(3):738-747.

[67] Ni H. Multiphase moisture transport in porous media under intensive microwave heating. PhD Thesis. Cornell University. 1997.

APPENDIX A

FUTURE WORK

In this work, fundamental physics based modeling was used in synergy with related experimentation to study, understand and optimize microwave and combination heating processes. Future work can be accomplished in the following areas by utilizing and extending the framework developed in this work:

A.1 Combination heating extended to complex food systems

In the present work, study of combination heating processes (Chapters 2-4) included materials that did not deform during the heating process and hence, were considered as rigid porous media. However, complex food systems such as meats undergo significant deformation during the heating process. A fully coupled electromagnetics-porous media transport-solid mechanics model needs to be used for modeling such processes. Additionally the problem would have to be solved in a 3D setting since axi-symmetry assumption would not be valid for relatively large samples (as compared to thin samples considered in Chapter 5) heated by microwaves. The model for coupled porous media transport and solid mechanics developed in Chapter 5 can be further integrated with the full electromagnetic model (solving the Maxwell's equations) for studying such systems. The comprehensive computational framework for solving such a problem is shown in Figure A.1.

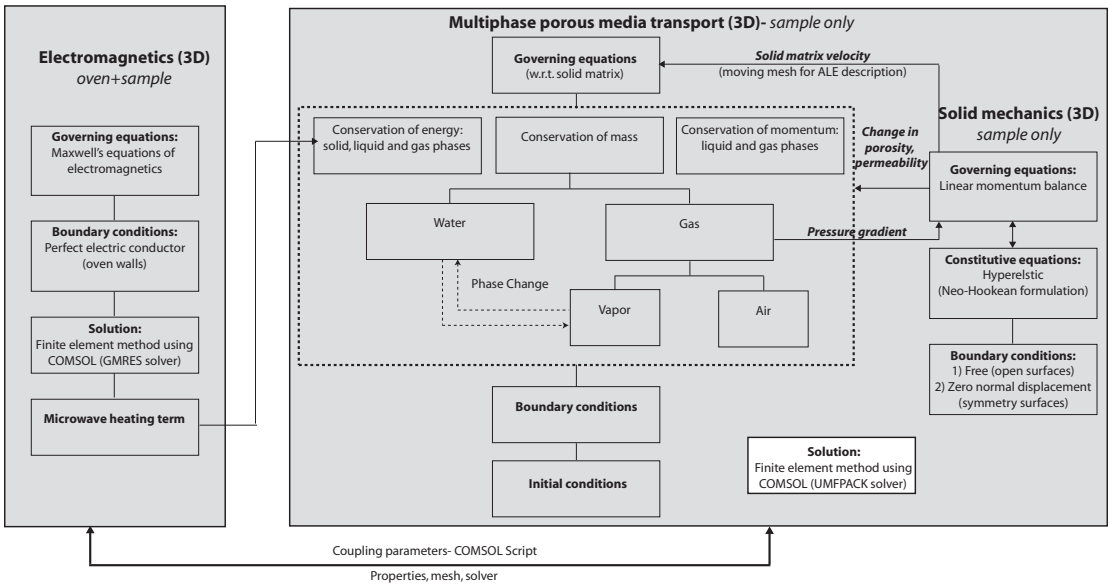

Figure A.1: Coupling between electromagnetics, multiphase porous media transport and solid mechanics (including large deformations) and the solution methodology.

A.2 Combination microwave heating including infrared heating using radiation modeling

Radiant heating was included as a boundary condition (using a heat transfer coefficient measured experimentally) for studying combination heating process involving radiant heating in this work. A sophisticated model for full radiation modeling has been developed in our research group[1]. To study the effect of infrared and combination microwave+infrared oven parameters in greater detail, the formulation for microwave combination heating developed in Chapters 2-4 can be coupled with the full radiation model. For shorter heating times, properties (dielectric, radiation and thermal) can be considered to be constant and the formulation in Chapter 2 can be used without significant increase in complexity.

For variable properties that need to be considering for longer heating times (still as-

suming negligible moisture loss), the formulation in Chapter 3 can be used along with the full radiation model. However, additional complexities will have to be incorporated. The present radiation model[1] has been developed in FLUENT and the coupled electromagnetics-heat transfer model has been developed in COMSOL Script. Compatibility issues and coupling between the two codes have to be considered. If temperature changes would change radiation properties significantly, the FLUENT module would have to be called from inside the COMSOL Script code to update the radiation solution after every few time steps.

Coupling the most comprehensive combination heating model (Chapter 4) with radiant heating module would be the most challenging. The problem size will be huge as well as coupling of FLUENT and COMSOL would have to be considered. Figure A.2 illustrates the proposed framework for the simulations.

A.3 Combination microwave heating with jet impingement using turbulence modeling inside the oven

Another combination heating technique involves using microwaves with jet impingement. A number of computational studies have been done in the past[2] but there has been no work on combination microwave+jet impingement heating with fundamental modeling of all the different physics involved. To study the process comprehensively, a conjugate problem needs to be solved that includes modeling of turbulent airflow inside the oven cavity and multiphase porous media transport inside the sample along with full electromagnetic modeling of microwave heating. For this problem, again the framework developed in this work (Chapters 2-4) can be used for modeling combination heating and can be coupled with a turbulence model such as the standard $k-\epsilon$ model,

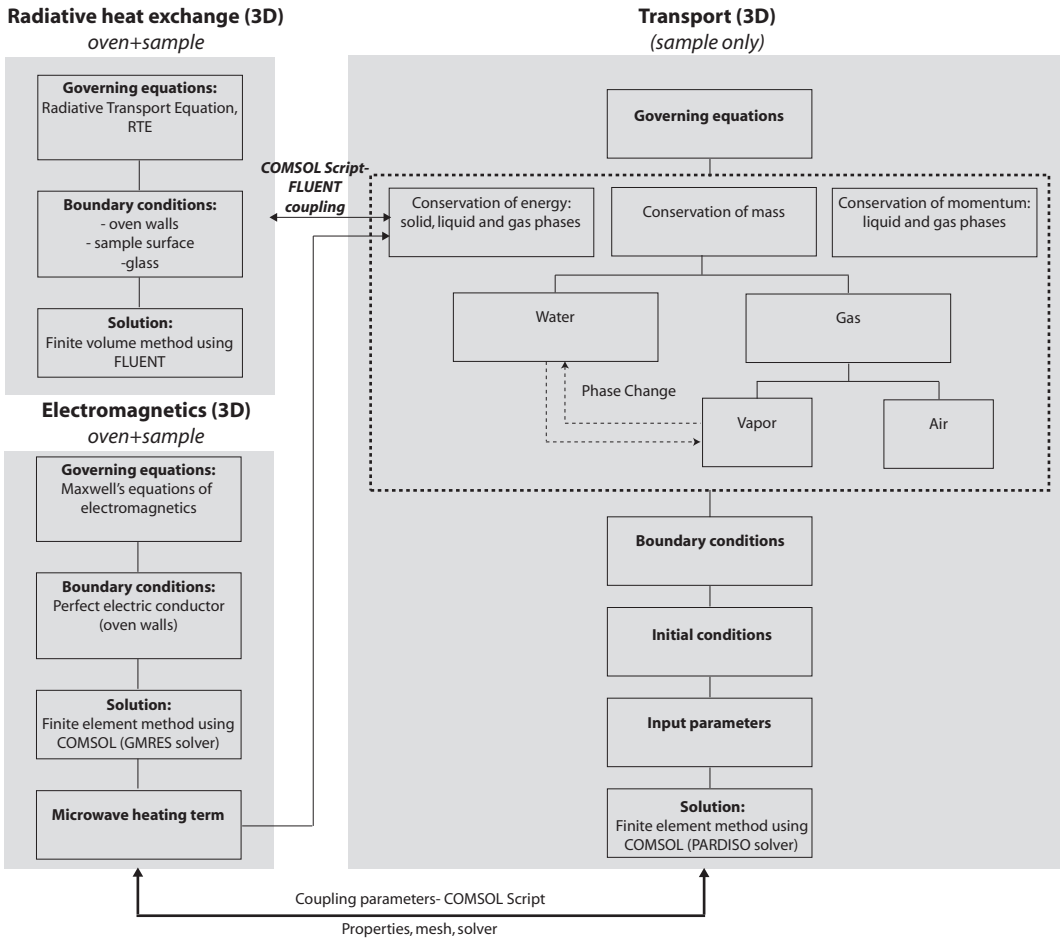

Figure A.2: Flow chart showing the coupling between the different physics and the solution methodology.

which is available in COMSOL, to account for airflow due to jet impingement inside the oven cavity. The model developed for turbulent airflow in the upper airway can be used as a reference[3].

A.4 Study of microwave thawing

Microwave thawing is a process in which rapid change of thermal and dielectric properties of the sample takes place when the sample is heated using microwaves. Mathe-

matically it is identical to the problem solved in Chapter 3. The only difference being that the dielectric properties change at a much faster rate during thawing as the sample changes phase from solid to liquid. Therefore, the update the EM solution needs to be carried out at a much faster rate. In the preliminary work on microwave thawing that we started, we had to use an update interval as small as 1 s to accurately model the process.

A.5 Computational framework for other applications

With the availability of a comprehensive modeling framework that includes a number of different fundamental physical phenomena (electromagnetics, complex transport, solid mechanics) from this work, possibilities for using the models are broad and exciting and they can be used for detailed study of a wide range of problems. The modeling framework is fundamental physics based and can be applied directly to generic porous media based applications such as modeling of fuel cells, digesters, biosensors, ground-water flow, reservoir flow (oil/gas/water flow, CO_2 sequestration, etc.) and biomedical applications (drug delivery, thermal therapy, etc.).

BIBLIOGRAPHY

[1] Dhall A, Datta AK, Torrance KE, Almeida MF. Radiative heat exchange modeling inside an oven. *AIChE Journal*. 2009;55(9):2448-2460.

[2] Geedipalli S, Datta AK, Rakesh V. Heat transfer in a combination microwave-jet impingement oven. *Food and Bioproducts Processing*. 2008;86(C1):53-63.

[3] Rakesh V, Datta AK, Ducharme NG, Pease AP. Simulation of Turbulent Airflow using a CT Based Upper Airway Model of a Racehorse. *Journal of Biomechanical Engineering- Transactions of the ASME*. 2008;130(3):031011.